MONTAN
UNIVERSITÄT
LEOBEN

Chair of Physics

Doctoral Thesis

Growth morphologies for the deposition of Para-hexaphenyl molecules on amorphous substrates

Dipl.-Ing. Stefan Lorbek

January 2021

MONTANUNIVERSITÄT LEOBEN
www.unileoben.ac.at

EIDESSTATTLICHE ERKLÄRUNG

Ich erkläre an Eides statt, dass ich diese Arbeit selbständig verfasst, andere als die angegebenen Quellen und Hilfsmittel nicht benutzt, und mich auch sonst keiner unerlaubten Hilfsmittel bedient habe.

Ich erkläre, dass ich die Richtlinien des Senats der Montanuniversität Leoben zu "Gute wissenschaftliche Praxis" gelesen, verstanden und befolgt habe.

Weiters erkläre ich, dass die elektronische und gedruckte Version der eingereichten wissenschaftlichen Abschlussarbeit formal und inhaltlich identisch sind.

Datum 14.01.2021

Stefan Lorbek

Unterschrift Verfasser/in
Stefan Lorbek

Growth morphologies for the deposition of Para-hexaphenyl molecules on amorphous substrates

by
Dipl.-Ing. Stefan Lorbek
submitted in fulfillment of the requirements for the degree of
Doktor der montanistischen Wissenschaften
at the Institute of Physics
University of Leoben, Austria

under supervision of
Ao. Univ. Prof. Dr. Christian Teichert

refereed by
Ao. Univ. Prof. Dr. Christian Teichert
and
Ao. Univ. Prof. Dr. Roland Resel

Leoben, January 2021

To my wife and our children

Abstract

There is already a large variety of applications on the consumer market made of thin films of organic semiconducting materials. Therefore, it is crucial to understand the formation mechanisms of such organic films. Here, thin films of the aromatic rod-like molecule Para-hexaphenyl (6P) were grown by organic molecular beam epitaxy under ultra-high vacuum conditions. For these experiments, Ar^+-bombarded mica and silicon dioxide (SiO_2) were used as amorphous substrates. 6P tends to build mounds of nearly upright standing molecules on this kind of substrates. The growth morphology of these thin films was investigated by various ex- and in-situ atomic force microscopy techniques (AFM). One important parameter in nucleation of thin-film growth is the critical nucleus size i^*. The analysis of the experiments reveals that the calculated values for i^* from rate theory, island-size scaling, and capture-zone scaling (using the generalized Wigner surmise) are in good agreement with each other. 6P on ion-bombarded mica and on SiO_2 can exhibit a post-nucleation with a dewetting by virtue of the exposure to air, most probably because of water co-adsorption. After growth, short annealing of 5 to 10 minutes up to a substrate temperature of 423 K was applied to the 6P thin films. AFM phase mode investigations yield that islands shrink, but something remains or changes the surface at the position of the former islands. Kelvin probe force microscopy reveals a change in the contact potential difference at these positions in comparison with positions at remaining 6P islands or pure SiO_2. Further, 6P was deposited under a grazing incidence at angles between 70° and 85° with respect to the substrate's surface normal. Steering effects, which are present in inorganic growth under grazing incidence, were not observed for organic thin films of 6P on SiO_2. However, there is an evidence of a slight change in the fractal dimension of the resulting 6P islands. Finally, the nucleation of elongated hexagonal islands in subsequent layers was investigated by AFM and simulations using empirical force-fields (EFF) together with molecular dynamics (MD) simulations were performed. The preferable inner angles of the hexagonal islands are $(104 \pm 2)^\circ$ and $(126 \pm 2)^\circ$. EFF simulations result in an octagonal structure as an equilibrium shape of the 6P single crystal and MD simulations explain the formation of a hexagonal structure because the 6P molecules have a higher sticking probability at the [10] facet.

Kurzfassung

Es gibt bereits eine Vielzahl von Anwendungen am Markt, welche aus sehr dünnen Schichten organischer Halbleitermaterialien bestehen. Daher ist es wichtig, die Mechanismen hinter der Bildung solcher organischer Schichten zu verstehen. Deshalb wurden im Rahmen dieser Arbeit dünne Schichten aus Para-hexaphenyl (6P) – einem stäbchenförmigen aromatischen Molekül – durch Molekularstrahlepitaxie unter Ultrahochvakuumbedingungen gewachsen. Für diese Experimente wurden mit Ar^+-Ionen beschossene Glimmerplättchen und Siliziumoxid (SiO_2) als amorphe Substrate verwendet. 6P neigt dazu, auf dieser Art von Substraten Hügel aus nahezu aufrecht stehenden Molekülen zu bilden. Die Wachstumsmorphologie dieser dünnen Schichten wurde mithilfe von verschiedenen ex- und in-situ Technicken der Rasterkraftmikroskopie (AFM) untersucht. Ein wichtiger Parameter bei der Keimbildung des Dünnschichtwachstums ist die kritische Keimgröße i^*. Die Analyse der Experimente zeigt, dass die berechneten Werte für i^* aus den drei Theorien – Wachstumraten, Skalieren von Inselgrößen und Skalieren der Einfangzonen (unter Verwendung der verallgemeinerten Wigner-Vermutung) – gut übereinstimmen. Auf ionenbeschossenem Glimmer und auf SiO_2 kann es aufgrund von Kontakt mit Luft – höchstwahrscheinlich wegen einer Wasserkoadsorption – zu einer späteren Bildung von Keimen durch eine Entnetzung des 6P kommen. Nach dem Wachstum wurden die gewachsenen 6P Schichten für 5 bis 10 Minuten bis zu einer Substrattemperatur von 423 K getempert. AFM-Untersuchungen im Phasenmodus ergaben, dass die Inseln schrumpfen, aber an der Position der ehemaligen Inseln etwas zurückbleibt oder die Oberfläche verändert. Die Raster-Kelvin-Sondenmikroskopie zeigt eine Änderung der Oberflächenpotentialdifferenz an diesen Positionen im Vergleich zu Positionen an noch bestehenden 6P-Inseln oder unbedeckten SiO_2. Ferner wurde 6P unter steilen Winkeln zwischen 70° und 85° in Bezug auf die Normale der Probenoberflächen aufgedampft. Bei diesen organischen Dünnschichten aus 6P auf SiO_2 wurden jedoch keine Lenkungseffekte beobachtet, die jedoch beim anorganischen Wachstum bei streifenden Einfall auftreten können. Es gibt allerdings Hinweise auf eine geringfügige Veränderung der fraktalen Dimension der so gewachsenen 6P-Inseln. Schließlich wurde die Keimbildung länglicher hexagonaler 6P-Inseln in höheren Schichten mittels AFM untersucht und Simulationen mit empirischen Kraftfeldfunktionen (EKF) zusammen mit Molekulardynamik (MD) durchgeführt. EKF Simulationen resultieren in einer achteckigen Struktur als Gleichgewichtsform eines 6P-Einkristalls, und MD Simulationen erklären die Bildung der darausfolgenden hexagonalen Struktur, da 6P eine höhere Wahrscheinlichkeit hat, an der [10]-Facette haften zu bleiben.

Acknowledgments

First of all I have to thank my supervisor **Prof. Dr. Christian Teichert** for advice, motivation, and his constant fatherly nudges in the right direction.
Prof. Dr. Oskar Paris for giving me the possibility to perform the work for this thesis in the Institute of Physics at the Unviversity of Leoben.

Furthermore, I want to thank all the members of the Institute of Physics for their support and friendship. Especially, **Ing. Heinz Pirker** for his great effort to put his expertise into solving all kind of electronics and computer problems, **Peter Mocharitsch** for crafting all things needed for the UHV system, and **Heide Kirchberger** and **Magdalena Ottrin** for their help with bureaucracy.

A big thank to **Dr. Gregor Hlawacek** for his patience in teaching me all things about growing 6P thin-films in UHV and AFM.
Special thanks to **Dr. Kratzer** for his longtime friendship, many fruitful discussions, and his great help in all scientific matters.
I am grateful to **Dipl.-Ing. Quan Shen**, not only for his friendship and fun in laboratory, but also for his expertise in FFM and TSM.
Thanks to **Dr. Igor Beinik**, **Dr. Christian Ganser**, **Dr. Patrice Kreiml**, **Dr. Andreas Nevosad**, **Dr. Franz Schmied**, **Dipl.-Ing. Astrid Wachauer**, and **Lin Wang** for their friendship and the nice time together in laboratory.
Dipl.-Ing. Tomas Kamencek for his patience in performing many measurements which were a big help for the investigation of hexagonal second-layer structures.
Prof. Dr. Peter Puschnig, **Dr. Dimitrii Nabok**, and **Dr. Giulio Biddau** from the Chair for Atomistic Modelling and Design of Materials for the theoretical input and simulations for this thesis.
Prof. Dr. Thomas Griesser and **Dr. Matthias Edler** from the Chair of Polymeric Chemistry for providing the Oxford Plasmalab System 100 and supporting me in the chemical cleaning of the Knudsen-cell.

And a big “thank you” is for all collaboration partners from different institutions. Especially **Prof. Dr. Adolf Winkler** and his students from Graz University of Technology, Austria for inspiration and many discussions, and to **Dr. Thomas Potocar** for supplying us samples of 6P grown on ion-bombarded mica.

Dr. Yuri Kozyrev and **Dr. Maria Rhubezhanska**, who unfortunately both passed away, at O.O. Chuiko Institute of Surface Chemistry, National Academy of Sciences of Ukraine, Kiev, Ukraine for their hospitality and teaching me the growth of Er/Si(001) in UHV with the help of RHEED.

Dr. Paloma Tejedor and **Dr. Marcos Benedicto** at Instituto de Ciencia de Materiales de Madrid, CSIC, Madrid, Spain for their hospitality.

However, the biggest thank to my wife **Lisa** and our children **Valentina** and **Maximilian** for their patience and support all these years.

Contents

Abstract i

Kurzfassung iii

1 Introduction 1

2 Fundamentals 3
- 2.1 Growth . . . 3
  - 2.1.1 Surface Processes . . . 5
  - 2.1.2 Nucleation . . . 10
  - 2.1.3 Consideration of diffusion-limited aggregation . . . 16
  - 2.1.4 Steering effects during deposition . . . 20
- 2.2 6P – a semiconducting molecule . . . 24
- 2.3 Substrates . . . 28
  - 2.3.1 SiO_2 . . . 28
  - 2.3.2 Mica . . . 30
  - 2.3.3 BaF_2 . . . 32
- 2.4 Deposition technique . . . 32
- 2.5 Characterization techniques . . . 34
  - 2.5.1 Atomic force microscopy (AFM) . . . 34
  - 2.5.2 Helium Ion Microscopy (HIM) . . . 41

3 Experimental 43
- 3.1 Preparation of substrates . . . 43
  - 3.1.1 SiO_2 . . . 43
  - 3.1.2 Mica . . . 46
  - 3.1.3 BaF_2 . . . 47
- 3.2 The ultra-high vacuum setup . . . 47

3.3 Characterization of samples 52
3.3.1 AFM equipment 52
3.3.2 Software and its usage for characterization 55

4 Results 57
4.1 Nucleation 57
4.1.1 Determination of the critical island size 57
4.1.2 Growth on plasma etched SiO_2 surfaces 65
4.1.3 Growth on SiO_2 after different thermal cleaning procedures 68
4.1.4 Growth at different substrate temperatures 74
4.1.5 Growth with different deposition rates 78
4.1.6 Bimodal island-size distribution in thin-film growth 80
4.2 Investigations of 6P on SiO_2 when performing a short annealing after film growth 85
4.3 Investigations of 6P deposition at grazing incidence on amorphous SiO_2 . 91
4.4 Hexagonal shaped islands in second and higher layers 103
4.5 6P thin-film growth on BaF_2 114

5 Summary & Outlook 117

List of Figures 123

List of Tables 139

List of Publications 141

Bibliography 156

Acronyms 157

1 Introduction

> „There is an enormous world-wide effort both in basic scientific research as well as in industrial development in the area of organic electronics. It is becoming increasingly clear that, if devices based on organic materials are ever going to have a significant relevance beyond being a cheap replacement for inorganic semiconductors, there will be a need to understand interface formation, film growth and functionality. ...“ (From NFN-final report [1])

These are the first lines within the final report of the National Research Network (Nationales Forschungsnetzwerk – NFN) for "Interface Controlled And Functionalised Organic Films" which was a national cooperation of scientific groups from different institutes at four Austrian universities in Linz, Graz, and Leoben. The scientific and technical range covered the branches from chemistry to applied physics by simulating, fabricating, and characterizing homogeneous films, organic heterostructures and prototype devices as organic solar cells and organic thin film transistors (OTFT). The network was divided into 10 single projects (situated at the above-mentioned four universities) and financed by the FWF, the Austrian Science Fund.

The experimental work for this thesis was performed within this NFN which was running from 2006 until 2012.

The quoted text at the beginning demonstrates very clearly the motivation for this work. If we look back 15 years ago, we were living already for decades in the so-called computerized age. The aim of those days (and still now) was to fabricate faster, smaller and less energy-consuming devices. It was realized that all of these goals were not so easy to reach by using inorganic semiconducting materials. But they were well understood, and we mostly able to control their chemical and physical behavior. Well, but we also became aware about their limits. A new promising family of materials was found in organic molecules, or better to say in thin films consisting of one kind or a mixture of different kinds of molecules. These films can have a crystalline structure of molecules which either areises from alignment with ordered structure of the substrate (e.g., Cu(001) [2], highly oriented pyrolytic graphite (HOPG) [3],...) or from self-assembling into monolayers of lying or standing molecules. The advantages of using organic materials are the big variety of molecules, their cheap production, the low costs of fabricating devices (e.g., ink-jet printing of circuits), and the low energies needed for device operation. Further, screens and displays made from organic light emitting diodes (OLED) show superior color quality compared to conventional display technology. The most interesting advantage nowadays is the possibility of fabricating very thin films on bendable substrates which made mobile phones with flexible screen possible as demontrated by the Royol Corporation at the Consumer Electronic Show in Las Vegas 2019. Other companies are already producing large scale organic solar cells on bendable synthetic foils which can be used, e.g., as roofs for tents (AMOR solar power films, Nantes, France). Known disadvantages can be for example a shorter lifetime of such devices and their sensitivity against UV-light or air compared to their inorganic counterparts.

Anyway, many leaders in economics and politics became aware of the potential in using organic molecules. Therefore, the theoretical and experimental understanding of such devices and more important of the thin films which are the heart of many of these devices becomes more and more essential. This was the main driving force for this thesis. The SPM group at the University of Leoben which was part of the NFN from 2006 on had already practical experience in growing and characterizing thin films by different methods. This thesis should not only be the continuation of the work on growth of the rod-like molecule Para-hexaphenyl by G. Hlawacek who began growing organic thin films in the SPM group Leoben [4]. It aimed at deeper questions as for example about the processes in the early stage of growth (e.g., submonolayers of molecules). These investigations are summed up and will be discussed in detail in this work.

2 Fundamentals

2.1 Growth

In this work, the main attention is laid on the epitaxial growth of small organic molecules on substrates of different kind. Epitaxy (from the Greek words “epi” – on or above and “taxis” – in order / in ordered manner) means the oriented growth on a substrate which is in a strong sense a single crystal. It is a type of crystal growth or, in more technical meaning, material deposition where the deposit forms new layers with one or more well-defined orientations with respect to the crystalline order of the substrate. Mostly substrates with amorphous surfaces, which fulfill not really the typical definition of epitaxy, were used for this work here. Anyway, some of the concepts of epitaxy are still applicable when it comes to the growth on amorphous substrates which are in general weakly interacting. The low interaction between the deposit and the substrate imply that the same thermodynamics like in epitaxy on weakly interacting crystalline substrates takes place in the early stages of crystal growth. At later stage, when the nuclei have grown sufficiently large, the growth is predominantly governed by kinetics. So the formation of a critical nucleus and its growth on isotropic surfaces can be contemplated with ideas lent from epitaxy.

In general, two kinds of epitaxial growth are distinguished – homoepitaxy and heteroepitaxy. The first describes the growth of some material onto itself and the second is the growth of different materials onto each other. During thin-film growth, the heteroepitaxial growth mode changes to homoepitaxy if growth proceeds on a closed layer or on top of already grown islands. In literature, three main growth modes are considered in thermodynamic equilibrium [5–7]. These modes are schematically illustrated in Figure 2.1.

a) layer-by-layer growth (Frank - van der Merwe)
Only if the first monolayer completely covers the surface the next layer begins to grow and so on.

b) layer-plus-island growth (Stranski - Krastanov)
   After a monolayer or a few layers grown in layer-by-layer mode (wetting the surface completely) a change in growth towards three-dimensional crystallite formation happens.

c) island-by-island growth (Volmer - Weber)
   From begin on, only islands (in fact, three-dimensional crystallites) are formed on the surface without building a full layer. It takes a large coverage until these three-dimensional islands merge and cover the entire surface.

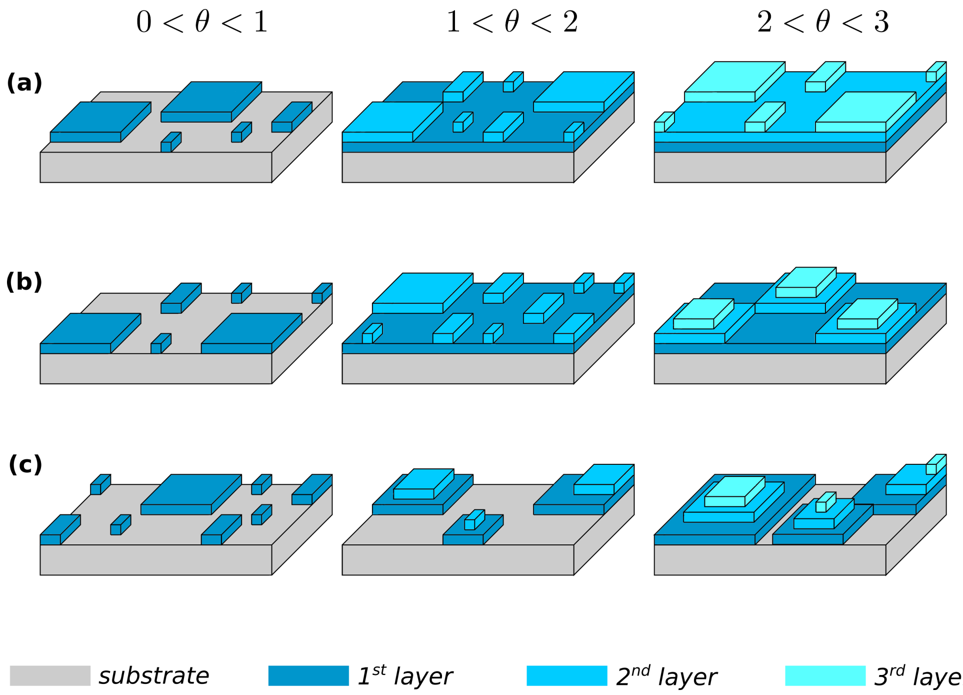

Figure 2.1: The different modes during thin-film growth in a schematic presentation: (a) Frank - van der Merwe, (b) Stranski - Krastanov, (c) Volmer - Weber for different coverage θ.

In inorganic growth, for most of the cases single atoms are the building blocks, whereas in organic thin-film growth organic, rather large, molecules are the building units. Inorganic and organic growth can behave similar. In principle in most cases organic molecules show the same growth behavior like single atoms. So they impinge onto the surface, can diffuse around, and eventually form nuclei. Nevertheless, there are some differences caused mainly by the anisotropy inherent of most molecules. They are building wetting layers or clusters and in a later stage tend to form islands of lying or standing molecules.

Which configuration – lying or standing – is adopted depends in part on the geometry of the molecules. There are flat, two dimensional molecules like Hexaazatriphenylene-hexacarbonitrile (HATCN) or Perylene-3,4,9,10-tetracarboxylic dianhydride (PTCDA) and rod-like molecules like Pentacene (5A) or Para-hexaphenyl (6P). These examples of molecules are only a small fraction of a plethora of organic molecules of which are used in organic semiconductor investigations. Another parameter with major impact on the growth behavior is the choice of the substrate on which the growth takes place. Because the relations between the surface free energy of the substrate σ_{Sub}, the film σ_{Film}, and the interfacial free energy $\sigma_{\mathrm{Sub/Film}}$ play an important role in the formation of thin films. There is already proof for the difference between growth on crystalline well oriented surfaces and amorphous substrates [8]. Further, one has to keep in mind growth parameters like the substrate temperature T, the growth rate R, the roughness of the surface, the kinetic energy of the impinging molecules, and so on. Every single parameter can cause a shift of growth mode, film morphology, or structure. Therefore, the investigation of the growth mechanisms of organic molecules will continue for the next decades because new synthesized molecules and even new substrates are constantly appearing always on the scene[9–11].

2.1.1 Surface Processes

If molecules are considered as single particles (like atoms) a number of processes during deposition have to be taken into account. The most important ones are presented in Figure 2.2. It illustrates some basic mechanisms of inorganic epitaxial growth. As mentioned before, some of the key parameters of thin-film growth are the deposition rate R, the surface temperature T, adsorption energy E_{a} when arriving at the surface, terrace diffusion barrier E_{d} (diffusion energy), step edge barrier E_{ES} (Ehrlich-Schwoebel barrier), nearest-neighbor bond strength between particles E_{bond}. These parameters are important to explain adsorption, diffusion, and desorption processes [6, 12].

To understand adsorption and desorption of particles onto or from a surface, the thermodynamics of this situation needs to be investigated further. The deposition rate R (sometimes called impinging rate or often used to be called the deposition flux F in literature) is related to the vapor pressure p, the atomic mass m and the temperature T

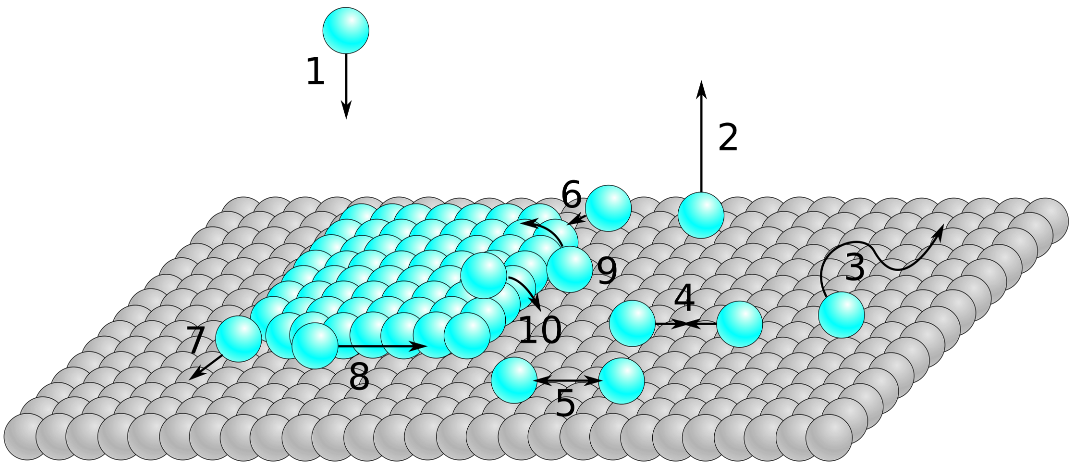

Figure 2.2: Schematic of the key processes during epitaxial growth (1 – adsorption, 2 – desorption from surface, 3 – adatom diffusion on surface, 4 – formation of dimers, trimers, or bigger clusters, 5 – decay of dimers or similarly small clusters, 6 – incorporation of particles into existing stable clusters or islands, 7 – detachment of particles from clusters or islands, 8 – edge diffusion, 9 – step-up jump, 10 – step-down hopping).

with the Boltzmann constant k_B

$$R = \frac{p}{\sqrt{2\pi \cdot m \cdot k_B \cdot T}} \ . \tag{2.1}$$

At equilibrium it is possible to assume a sublimation of a pure solid which is given by the equality of the chemical potential of vapor μ_{V} and of solid μ_{S} ($\mu_{\mathrm{V}} = \mu_{\mathrm{S}}$). At low pressure p the chemical potential of the vapor is

$$\mu_{\mathrm{V}} = -k_B \cdot T \cdot \ln \frac{k_B \cdot T}{p \cdot \lambda^3} \tag{2.2}$$

with λ as the thermal deBroglie wavelength (chap. 1.3.1, pp.11 in [6]). Then the equilibrium vapor pressure p_{e} can be derived in terms of the chemical potential of the solid μ_{S}

$$p_{\mathrm{e}} = \left(\frac{2\pi \cdot m}{h^2}\right)^{3/2} \cdot (k_B \cdot T)^{5/2} \cdot \exp \frac{\mu_{\mathrm{S}}}{k_B \cdot T} \ . \tag{2.3}$$

Now the problem of the need of a model for μ_{S} occurs. Klein & Venables [13] showed in 1976 that a typical μ_{S} at low pressure is a “quasi-harmonic” model and this is equal to the free energy per particle ($\mathcal{F}/N = \mu_\mathrm{S}$)

$$\mathcal{F}/N = -L_0 + V_0 \ . \tag{2.4}$$

The first term L_0 is the energy per particle in the solid relative to the vapor and the second term V_0 is the energy due to the harmonic zero-point vibrations of the solid.

To understand the full picture of the kinetics during growth, at first the idea of supersaturation needs to be considered. Mostly solidification from the vapor phase begins at supersaturation which means growth at non-equilibrium state. Figure 2.3 shows that a certain

$$\Delta\mu = \mu_\mathrm{V} - \mu_\mathrm{S} \tag{2.5}$$

is the thermodynamic driving force of supersaturation after the definition by Markov (chap.1.2 in [5]) which goes back to the paper of Burton, Cabrera & Frank [14] in 1951:

> “It is called a supersaturation and is defined as the difference of the chemical potentials $\Delta\mu$ of the infinitely large mother and new phases at the particular value of the temperature.”

If the vapor is considered as an ideal gas and after executing the integration (shown on p.6 in [5]) it is possible to obtain the following expression for the thermodynamic driving force during supersaturation, where the relation p/p_e is the value of supersaturation with p_e the equilibrium pressure from eq. (2.3):

$$\Delta\mu = k_B \cdot T \cdot \ln(p/p_\mathrm{e}) \tag{2.6}$$

As shown in Figure 2.3, it is clear that (a) in equilibrium $\Delta\mu$ must be zero, (b) it should be positive during condensation, and (c) negative in case of sublimation or evaporation.

Further, if the adsorption energy E_a of a particle is high enough, the particle can become a part of the surface with a certain mobility on the surface given by the diffusion energy E_d (usually $E_\mathrm{a} > E_\mathrm{d}$). In case of impinging atoms, these particles are called adatoms (as a simplification here used even for molecules hitting the surface). The energy for desorption is often given by the negative E_a in the literature. For example, the rate of desorption is approximately described as

$$R_\mathrm{des} = \nu_\mathrm{a} \cdot \exp(-E_\mathrm{a}/(k_B \cdot T)) \ , \tag{2.7}$$

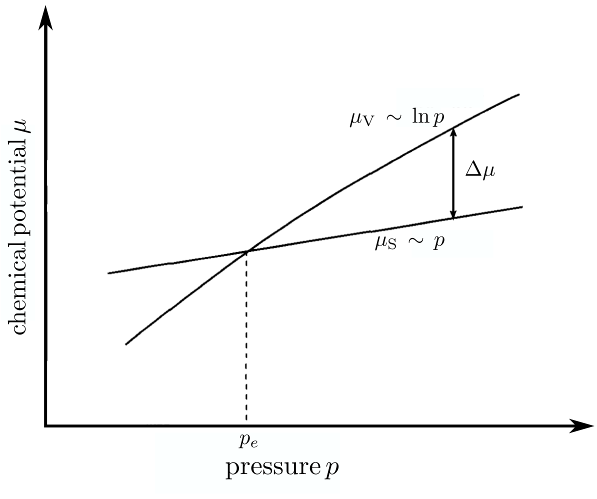

Figure 2.3: Dependency of the chemical potentials μ_V and μ_S on the pressure p. p_e indicates the equilibrium pressure. (Reproduced from Figure 1.2 on p.5 in [5])

with ν_a the (pre-exponential) attempt frequency of particles leaving the surface.
In addition, the particles can be mobile on the surface. They move around until they find each other building a stable nucleus for a new island or they aggregate into an existing island (or step edge) or they leave the surface again within the process of adsorption-desorption. Assuming the motion beeing a random walk in two dimensions, the particles will diffuse in 2D on the surface with the following diffusion coefficient in the Arrhenius form of

$$D = D_0 \cdot \exp(-E_d/(k_B \cdot T)) \;, \tag{2.8}$$

where E_d is the activation energy for diffusion of the particle on a terrace, where E_d depends on the surface orientation. D_0 is the frequency of the particles for lattice jumps over the surface. In literature its value is often given as $\nu_d \cdot a^2/4$ with ν_d the attempt frequency of the diffusing particles and a the lattice parameter. D_0 can be simplified to $\nu_d/4$ (chap.1.3.2 pp.16 in[6]). In addition to D, during diffusion the adatom lifetime on the surface before desorption

$$\tau_a = \nu_a^{-1} \cdot \exp(-E_a/(k_B \cdot T)) \tag{2.9}$$

is also relevant. These two parameters yield the characteristic diffusion length

$$x_s = \sqrt{D \cdot \tau_a} \;, \tag{2.10}$$

which tells about the fate of the adatom and defines even the role of steps in evaporation and condensation (which is more important for atoms and very small molecules) [14]. Together with the deposition rate, this leads to an adatom density (molecule density on the surface)

$$n_1 = R \cdot \tau_\mathrm{a} \; . \tag{2.11}$$

This will be important for the nucleation in the early stage of island growth as will be discussed in section 2.1.2 of this chapter.

Atoms and molecules are not only performing a so-called “intralayer” diffusion by diffusing on terraces or along step edges. They can incorporate into step edges in 2D or even in three dimensions perform a so-called “interlayer” diffusion by overcoming the additional step edge barrier (Ehrlich-Schoebel barrier E_ES illustrated in Figure 2.4 [15, 16]). So the particles are able to do step-up jumps and step-down hoppings (like shown in the sketch of Figure 2.2).

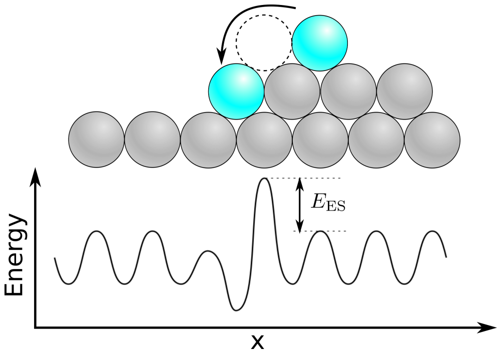

Figure 2.4: A particle descending from a step edge experiences an additional energy barrier E_ES – the Ehrlich-Schwoebel barrier.

For molecules diffusing across a descending step there are certain peculiarities to be considered. Hlawacek et al. [4] have shown for rod-like molecules that they begin to bend themselves to reduce the step edge barrier energy while traversing a step edge which looks like a crawling caterpillar (shown in Figure 2.5).

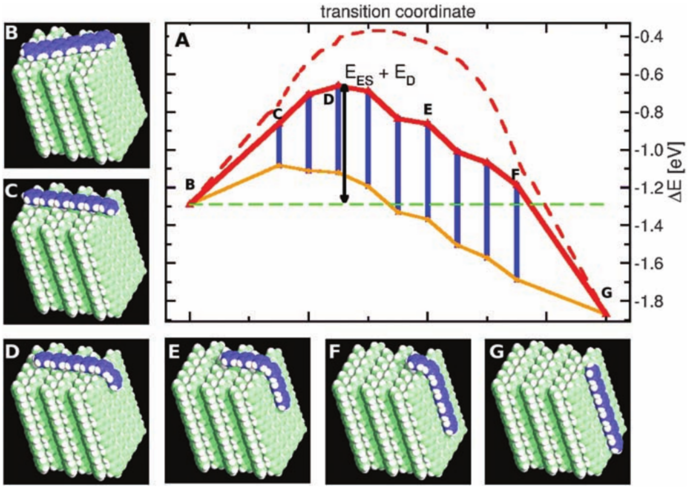

Figure 2.5: (A) Energies associated with the transition path for diffusion of a rod-like molecule (exemplarily for a 6P molecule) over a step edge. Labels B to G correspond to situations illustrated in images (B) to (G) which are snapshots of the transition path. (Reproduced from [4])

2.1.2 Nucleation

The formation of stable islands in early thin film growth is very essential. After forming a stable nucleus the film begins to grow in islands. Due to the interplay of surface energies, diffusion energy, and step edge energy the film tends either to grow layer by layer (Frank - van der Merwe), forms mounds after closing the first layer (Stranski - Krastanov), or forms only three-dimensional crystallites with a hardly closed first layer (Volmer - Weber).

How and when stable nuclei are formed is defined by thermodynamics: the change in Gibbs energy (chap. 2.1.1 pp.80 in [5], chap. 2.2 pp.24 in [17])

$$\Delta G = -\frac{4}{3} \cdot \frac{\pi \cdot r^3}{v_\mathrm{l}} \cdot \Delta\mu + 4 \cdot \pi \cdot r^2 \cdot \sigma \tag{2.12}$$

is the driving force for nucleation. ΔG is a function of supersaturation $\Delta\mu$, surface energy σ, specific volume v_l and the droplet (nucleus) radius r. The maximum of ΔG defines the critical radius r^* of the nucleus and is given by

$$r^* = \frac{2 \cdot \sigma \cdot v_\mathrm{l}}{\Delta\mu} \; . \tag{2.13}$$

By substitution of r^*, the maximum value of the Gibbs energy change – which is necessary for the formation of a stable nucleus – is obtained from eq. (2.12):

$$\Delta G^* = \frac{16\pi \cdot \sigma^3 \cdot v_l^2}{3 \cdot \Delta\mu^2} \tag{2.14}$$

For better understanding of the influence of ΔG during nucleation, Figure 2.6 illustrates that the nucleation is a simple stability problem between the surface energy term ($4 \cdot \pi \cdot r^2 \cdot \sigma$ – energy cost) and the volume free energy term ($4/3 \cdot (\pi \cdot r^3)/v_l \cdot \Delta\mu$ – energy gain) in ΔG and that it is a elementary self-assembly process.

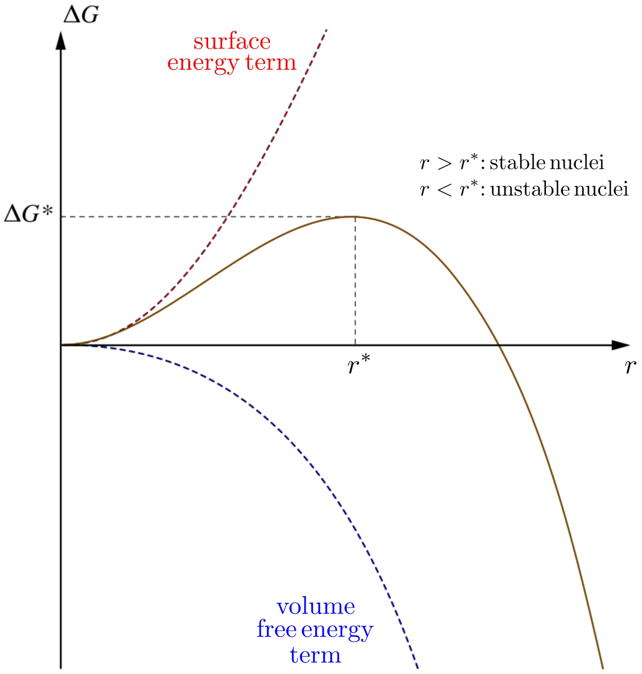

Figure 2.6: Dependency of the Gibbs free energy ΔG on the island radius r assuming the formation of a crystalline nucleus with a spherical shape from a supersaturated vapor phase. ΔG^* is the work of formation of the critical nucleus at radius r^*. (Reproduced from Figure 2.6 at p.25 in [17])

Furthermore, this radius of the critical nucleus size corresponds with the numbers of adatoms (or here molecules) which are within such a nucleus. This number is called critical nucleus size i^* (or even called critical island size). Only an amount of $i^* + 1$ adatoms can form a stable nucleus. So $i^* = 0$ means that an adatom does not move and is already a stable island, $i^* = 1$ means a dimer is stable, and so on (see Figure 2.7).

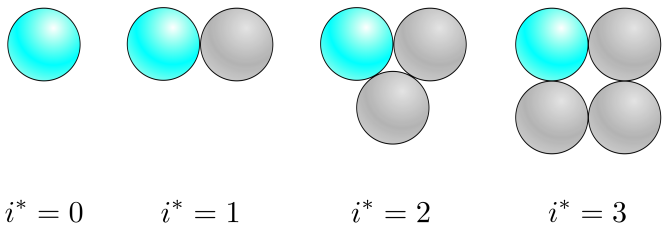

Figure 2.7: Diagram of different stable island configurations for $i^* = 0$ to 3 which means that the supercritical cluster is then a monomer, dimer, trimer, tetramer, and so on.

Estimating such an i^* by theory and simulations, three distinctive approaches were proposed by different authors:

a) Rate theory using rate equations (RE) by Venables, Spiller and Hanbücken [7].

b) Scaling theory using an island-size distribution (ISD) by Amar and Family [18].

c) Advanced scaling theory using a capture-zone distribution (CZD) by Pimpinelli and Einstein [19, 20].

Within the rate theory mean field rate equations (a set of coupled ordinary differential equations) have been developed to explain nucleation long ago [21]. At low coverage, the RE for an adatom density n_1 from eq. (2.11) is simply written like

$$\mathrm{d}n_1/\mathrm{d}t = R - \frac{n_1}{\tau} \tag{2.15}$$

with

$$\tau^{-1} = \tau_{\mathrm{a}}^{-1} + \tau_{\mathrm{n}}^{-1} + \tau_{\mathrm{c}}^{-1} + \ldots \tag{2.16}$$

and its steady state solution is again eq. (2.11). Here τ represents all loss terms for adatoms as desorption (τ_{a}), nucleation (τ_{n}), capturing by stable clusters (τ_{c}) and other processes. All this together is illustrated in Figure 2.8 (chap. 5.2.3 p.153 in [6] and [22, 23]).

The inverse ratio of deposition rate and diffusion

$$\mathfrak{R} = R/D \tag{2.17}$$

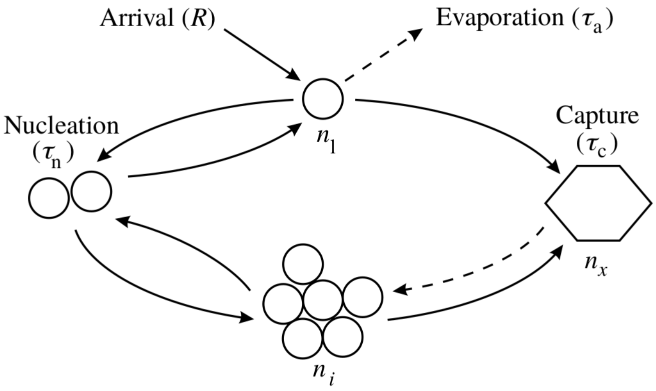

Figure 2.8: Schematic illustration which shows the interaction between nucleation and growth states. The density n_1 determines the critical cluster size n_i in conjunction with the different losses which have characteristic times. n_x is the density of already stable clusters (from chap 5.2.3, p.153, Figure 5.5 in [6]).

and the solution for the density of already stable clusters from RE [24]

$$n_x \approx \theta^{1/(i^*+2)} \cdot \mathfrak{R}^{i^*/(i^*+2)} \cdot \exp(E_{i^*}/(i^*+2) \cdot k_B \cdot T) \tag{2.18}$$

define the form of the important scaling relation in growth investigations

$$n_x \sim \mathfrak{R}^{\chi} \tag{2.19}$$

with the total coverage $\theta = R \cdot t$ (and the deposition time t) and the energy E_{i^*} which controls clustering (the sum of activation barrier for diffusion and binding energy of the critical cluster).
Where the scaling exponent χ can have two occurrences [7, 23]:

a) $\chi = i^*/(i^*+2)$ for 2D island formation,

b) $\chi = i^*/(i^*+2.5)$ for 3D island formation.

Extraction of i^* from simulation or experimental data can be done by plotting $\ln n_x$ vs $\ln R$ (after the proportionality of (2.19) together with (2.17)), because χ is nothing else than the slope of this graph.

Amar and Family suggested another ansatz which is based on the usage of a distribution of island sizes $\tilde{s}$ per unit area (ISD) [18, 25, 26]

$$N_{\tilde{s}}(\theta) = \theta \cdot \tilde{S}(\theta)^{-2} \cdot f_{i^*}(u) \ . \tag{2.20}$$

It scales with the average island size $\tilde{S}(\theta) = \left[\sum \tilde{s} \cdot N_{\tilde{s}}(\theta)\right] / \sum N_{\tilde{s}}(\theta)$, $u = \tilde{s} \cdot \tilde{S}(\theta)$ and $f_{i^*}(u)$ which is a dimensionless scaling function (independent of coverage, but different for each value of i^*). This scaling function is determined later for different critical island sizes i^*

$$f_{i^*}(u) = C_{i^*} \cdot u^{i^*} \cdot \exp(-i^* \cdot a_{i^*} \cdot u^{1/a_{i^*}}) \ , \tag{2.21}$$

where C_{i^*} and a_{i^*} are represented by the two following hypergeometrical equations which are important for the normalization and proper asymptotic behavior of the scaling function [18, 26]:

$$C_{i^*} = \frac{(i^* \cdot a_{i^*})^{(i^*+1) \cdot a_{i^*}}}{a_{i^*} \cdot \Gamma\left[(i^*+1) \cdot a_{i^*}\right]} \ , \qquad \frac{\Gamma\left[(i^*+2) \cdot a_{i^*}\right]}{\Gamma\left[(i^*+1) \cdot a_{i^*}\right]} = (i^* \cdot a_{i^*})^{a_{i^*}} \tag{2.22}$$

The used Γ-function was derived in the 18th century by Daniel Bernoulli for complex numbers with a positive real part and is defined via the convergent improper integral

$$\Gamma(z) = \int_0^\infty x^{z-1} e^{-x}\, dx, \qquad \mathrm{Re}(z) > 0 \ . \tag{2.23}$$

Practicable values for C_{i^*} and a_{i^*} are listed in Table 2.1 published in [27].

Table 2.1: The constants C_{i^*} and a_{i^*}, for i = 1–6.

i^*	C_{i^*}	a_{i^*}
1	1.1091	0.2715
2	1.9678	0.2976
3	3.2385	0.3086
4	5.1214	0.3145
5	7.9036	0.3182
6	11.9963	0.3207

A plot of $N_{\tilde{s}}(\theta) \cdot \tilde{S}(\theta)^2/\theta$ vs $\tilde{s}/\tilde{S}(\theta)$ leads to a histogram of $f_{i^*}(\tilde{s}/\tilde{S}(\theta))$. This is compared with the general scaling function in eq. (2.21) for different i^*. The scaling function which yields the highest coefficient of determination $\langle R^2 \rangle$ (best least square fit) with the sample data defines the critical nucleus size i^* of the investigated system.

Another approach using ISD was introduced by Mulheran, Blackman and later by Brinkmann et al. [28–30]. They suggested to perform a Voronoi tessellation according to the capture zones (so-called Voronoi cells) surrounding the islands within nearby diffusing adatoms are captured. The generation of such a Voronoi diagram is exemplified in Figure 2.9.

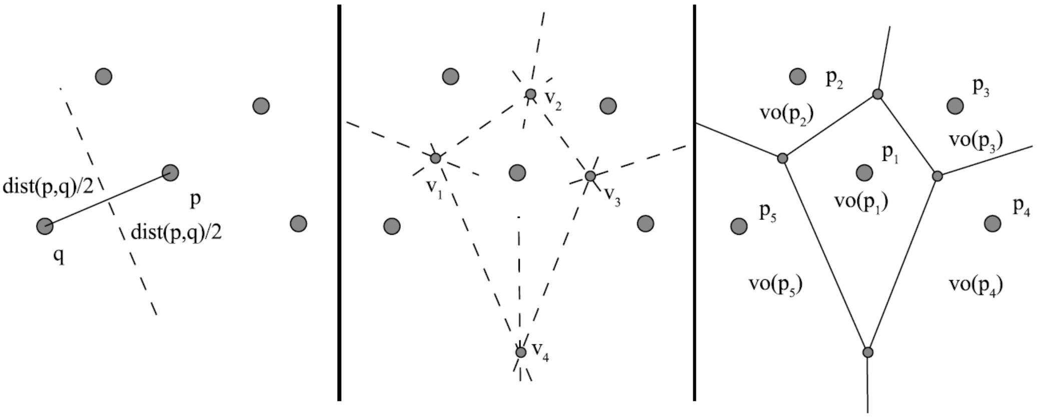

Figure 2.9: Step-by-step generation of a Voronoi diagram from 5 vertices in 2D; left: first a bisector between p and q is formed (divided by dashed line); middle: Voronoi vertices $\mathrm{v_i}$ are established at the bisector intersections; right: bisector remnants are now the Voronoi edges between the Voronoi cells $\mathrm{vo(p_i)}$. (From [31])

In 2007, Pimpinelli and Einstein proposed like Mulheran and others before the usage of capture zones for further investigations, but this time they recommended to describe the distribution of the capture-zone areas (therefore called capture-zone distribution – CZD) by a generalized Wigner surmise distribution

$$P_\beta(s) = a_\beta \cdot s^\beta \cdot \exp(-b_\beta \cdot s^2) \ , \tag{2.24}$$

a class of probability distribution functions based on random matrix theory [19] with the fluctuating variable of the capture-zone areas with size A normalized by their mean value $\langle A \rangle$

$$s \equiv A/\langle A \rangle \ . \tag{2.25}$$

a_β and b_β are constants, fixed by normalization and unit-mean conditions, like

$$a_\beta = 2 \cdot \Gamma\left(\frac{\beta+2}{2}\right)^{\beta+1} \Big/ \Gamma\left(\frac{\beta+1}{2}\right)^{\beta+2} \ , \qquad b_\beta = \left[\Gamma\left(\frac{\beta+2}{2}\right) \Big/ \Gamma\left(\frac{\beta+1}{2}\right)\right]^2 \ . \tag{2.26}$$

The values for a_β and b_β for different β are listed in Table 2.2 published in [27]. The key parameter for the critical nucleus size is here the variable β which has the form

$$\beta = i^* + 2 \tag{2.27}$$

in the two-dimensional case [20, 32, 33].

Table 2.2: The constants a_β and b_β, for β = 2–7.

i^*	a_β	b_β
2	3.24	1.27
3	6.25	1.77
4	11.60	2.26
5	21.05	2.76
6	37.62	3.26
7	66.50	3.76

In detail, this alternative method relies on the calculation of Wigner-Seitz cells surrounding each nucleation center, utilizing Voronoi tessellation as a way to characterize the capture zone of a growing island.

The determination of the proper i^* is done similar to the approach with ISD. The counts of s are plotted as a histogram (which shows the distribution $P(s)$). In a next step the obtained histogram needs to be compared with a few $P_\beta(s)$ at different values of β. And again, this $P_\beta(s)$, at a certain value of β, which fits best by the highest $\langle R^2 \rangle$, determines the critical nucleus size i^*. In comparison to ISD, the CZD is independent of the total coverage θ, of the island sizes and of the island shapes, because for the Voronoi diagram only the center of mass of every single island is needed. Nevertheless, CZD leads to a weaker statistics, because polygons – which possess vertices outside the investigated total area – need to be excluded. In contrast, the ISD is able to count all islands within the investigated total area.

2.1.3 Consideration of diffusion-limited aggregation

Three stages during thin-film growth can be estimated:

a) nucleation,

b) aggregation and

c) coalescence & percolation

During nucleation, stable nuclei are formed which begin to attract more adatoms to grow during the aggregation state. As discussed earlier, the growing island can first coalesce to a closed first layer (and then forming the next layer by coalescence or building mounds on this first layer) or begin forming mounds which coalesce later. Nevertheless, in every growth mode each new layer or island or step induces a new possibility for nucleation on its top which leads to aggregation and so on. The possible transition of a growing island is shown in Figure 2.10(a) to (c). The island may begin with a very ramified shape which is self-similar and thus called "fractal" with a fractal dimension between 1 and 2. If the island is more fractal its dimension is closer to 1. With continuous growth, the thin branches of the island coalesce to a few larger branches. The dimension of the island increases and it is then called "dendritic". Finally, the island becomes compact without any branches with a dimension close to 2. Figure 2.10(d) illustrates two possibilities how two compact islands can coalesce with each other.

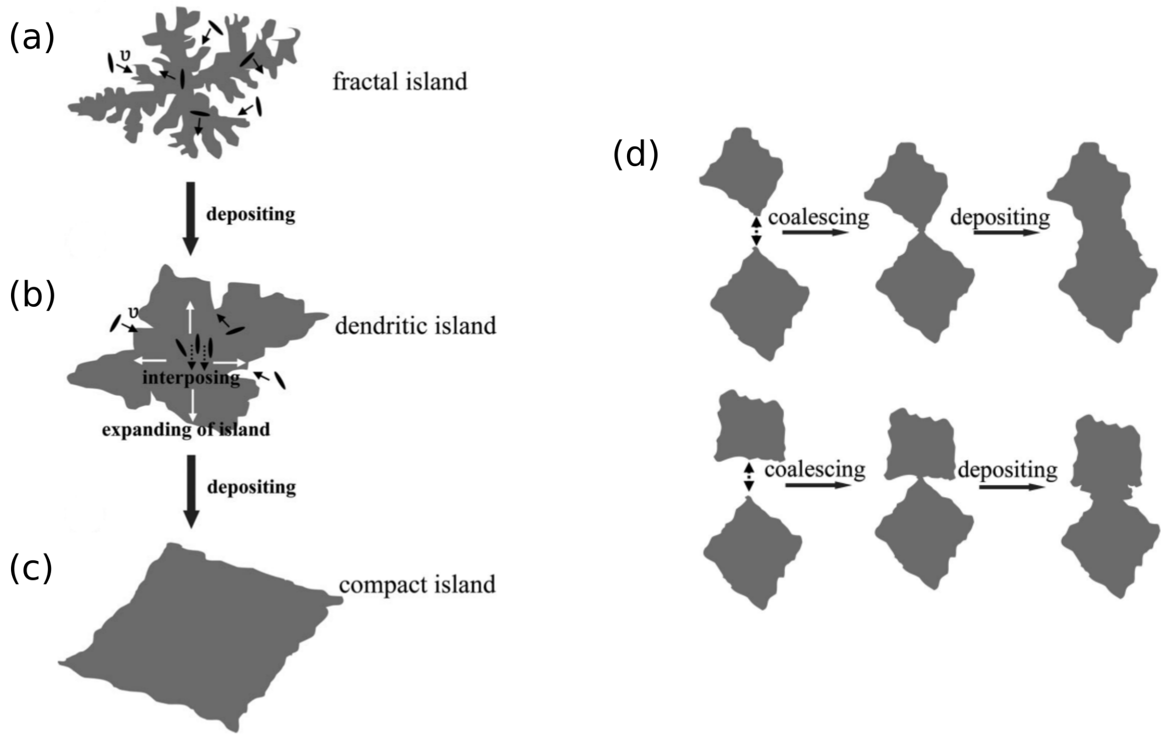
(a)
υ
fractal island
depositing
(b)
υ
dendritic island
interposing
expanding of island
depositing
(c)
compact island
(d)
coalescing
depositing
coalescing
depositing

Figure 2.10: (a), (b) and (c) show the transition during thin-film growth of an island from fractal to a dendritic shape which finally ends up in a large compact island. (d) The two rows are examples what happens to the islands during coalescence. (Reproduced from investigations of growth done by Yang et al. [34])

If the adatoms are highly mobile at the surface and at the edges of the nuclei more compact islands will be formed. The more the adatoms are prevented from diffusing along the edges the more ramified they become, until they are completely dendritic (reversible aggregation). In the extreme case, the adatoms which hit the nuclei do not perform any edge diffusion and will keep their initial position as part of the cluster. This is often called "hit-and-stick" process and leads to the formation of wide branches that spread out into random directions with lower fractal dimensions (irreversible aggregation). All these processes are combined into the general term of diffusion-limited aggregation (DLA). Kandel found two limits derived from RE which are important to understand DLA [35]. Classical DLA plays a main role within the first limit where attachment of particles to the cluster edges is infinitely fast. Whereas in the second limit, the adatoms react somehow more mobile. In this case, the kinetics of island growth is definitely limited by the slow attachment to island edges. If the second case is more probable than DLA, it is called attachment-limited aggregation (ALA) [36]. As a result, it has a big influence on the form of the scaling exponent χ in eq. (2.19). While for the nucleation in 2D within the first limit it holds in the form $\chi = i^*/(i^*+2)$, it changes to $\chi = 2 \cdot i^*/(i^*+3)$ which results in different values for i^* assuming ALA. In a similar manner, ALA provokes a modification in the CZD and eq. 2.27) changes to $\beta = (i^*+3)/2$ [36].

Witten and Sander were the first who suggested to investigate the regime of aggregation with computer simulations [37] and found that DLA fits best for growth far from equilibrium. They developed a suitable Monte Carlo algorithm (MC) to grow fractal structures which was first improved by Meakin et al. and Kolb et al. [38–42]. Until now, the work on DLA simulations which began with Witten and Sanders is still in progress.
In principle, a DLA simulation begins with a seed particle somewhere on a lattice. Then particle after particle is added once at a time to the growing aggregate, via random walk trajectories on the lattice. The starting point and the direction through every step on the lattice of each particle is newly generated in simplest case every time randomly by MC algorithms. The cases – a particle will attach, detach, or diffuse along the edge of the cluster – can be controlled with a simplified sticking coefficient k_s (with $0 < k_s \leq 1$; $k_s = 1$ means "hit-and-stick" compare with Figure 2.11) [43, 44]. More advanced simulations take temperature, coverage, deposition rate and energies (on the surface for diffusion, binding,...) into account, but their names vary in literature; mostly they are synonymous with kinetic Monte Carlo (kMC). In more advanced kMC, morphology dependent activation energies are included for both, intra- and interlayer diffusion [45].

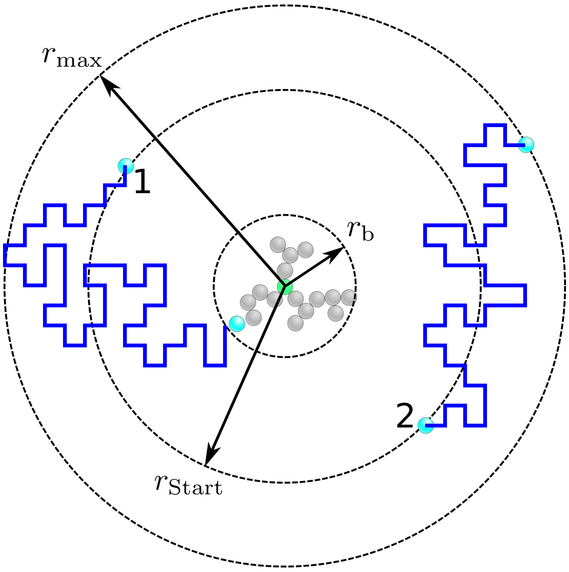

Figure 2.11: Schematic diagram of a simple DLA algorithm dated back to Figure 1 from [43]. It needs three zones (here shown as circles with radii r_b, r_{Start}, and $r_{\max}$). The diffusing particles are introduced at random points with the radius r_{Start} away from the center of the seed particle (green). The blue lines are probable random walks of the particles. In case 1, the particle reaches the aggregate (gray) which has a minimum bounding radius of r_b and sticks. In case 2, the particle reaches the external boundary (set at radius $r_{\max}$) and is rejected. Therefore a new particle will start at r_{Start}.

These DLA driven growths end up with a high ramification which leads to the self-similarity of the growth patterns. This can be investigated by the fractal Hausdorff dimension D_{f} which is a powerful tool in drawing comparisons between simulated and real grown films [46, 47]. The fractal dimension is numerically calculated from

$$D_{\mathrm{f}} = \frac{\log n_{\mathrm{dis}}}{\log \widehat{m}} \,, \tag{2.28}$$

where n_{dis} is the amount of disjoint parts of a geometrical object which represent smaller copies of the object, all scaled by the factor $\widehat{m}$ (like $1 : \widehat{m}$). If the object is ramified in such a way that it becomes difficult to find appropriate values for n_{dis} and $\widehat{m}$, the box-counting method leads numerically to the right fractal dimension – the so-called Minkowski–Bouligand dimension D_{fb} (see chap. 3.1 in [48] and [47, 49]). It works with a grid of boxes which is put over the fractal object. These boxes have the length ε and then only these boxes are counted which are located at the object's edges ($N(\varepsilon)$).

$$D_{\text{fb}} = \lim_{\varepsilon \to 0} \frac{\log N(\varepsilon)}{\log\left(\frac{1}{\varepsilon}\right)} \tag{2.29}$$

It should be obvious that a grid with smaller boxes leads to a higher $N(\varepsilon)$ which means that D_{fb} becomes more close to the actual fractal dimension of the investigated object.

During investigations with RE, ISD, and CZD of submonolayer thin films, the aggregation regime is suited best, because the islands of real grown thin films are big enough to be investigated.

2.1.4 Steering effects during deposition

Usually, the incident flux of particles towards the surface during a perpendicular deposition ($\alpha = 0°$) is presumed to be constant all over the surface. In this case R will be constant in the same way. But Shevchik pointed out in 1973 that the surface atoms have a significant influence on the particle trajectory in the gas phase [50]. The trajectory of the particles is bent slightly in the vicinity of the surface substrate atoms due to adatom-substrate interaction. This process is attractive that so that the trajectory of the incoming adatoms is not only bent. It is even preferable for them to land on top terraces driven by an increasing R (shown in Figure 2.12 for an Al/Ni(001) system by molecular dynamics simulation). In 2000, Raible et al. suggested a generalized nonlinear stochastic model to explain the growth of mound-like structures which can explain either the deflection of the trajectories towards the local surface normal and the acceleration of the particles in front of the surface [51, 52].

Dijken et al. performed 1999 growth experiments with a Cu/Cu(001) system at grazing angles of incidence (like for example in Figure 2.12(b) for the Al/Ni(001) system) and were able to show that the steering effect plays indeed a main role in increasing the surface roughness as well as the slope of the grown mound structures for increasing deposition angle ([54, 55] and later for organic films [56]). Further explanations were given using the pairwise Lennard-Jones potential for the calculations of the trajectories [57]. Figure 2.13(a) shows the different trajectories of three particles (A, B, C) which have a lateral offset in length $\delta_{\text{A,B,C}}$ between their theoretical target point and the real impact position due to different attractive potential caused by a one-monolayer-high island.

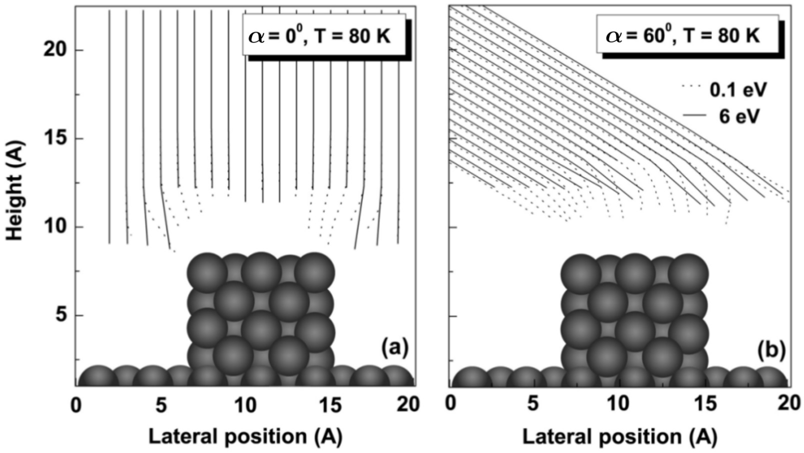

Figure 2.12: Atom trajectories for a surface with a four-monolayer-high Al island by molecular dynamics simulation on a Ni(001) surface. The trajectory calculations were performed for an adatom incident angle of (a) $\alpha = 0°$ and (b) $\alpha = 60°$ each at 80 K with 0.1 eV (dashed line) and 6 eV (solid line) incident energy. (From [53])

The fluctuations in the deposition rate R are plotted in Figure 2.13(b(i)+(iii)) and provide an idea about the lateral mechanisms around the island if to compare with R at normal-incidence deposition in Figure 2.13(b(ii)). There is even an incidence angle (and an energy) dependence of δ which was first demonstrated by Wormeester and Poelsema and is presented in Figure 2.13(c) [57]. It is evident that the steering effect becomes noticable if α is large enough ($\alpha > 50°$ found previously by Dijken [55]). For higher mounds, the effect becomes more crucial due to the increasing fluctuations in R (see Figure 2.13(b(iii)) [55, 58].

Further investigations by experiments and simulations (molecular dynamics and kMC) for the Cu/Cu(001) and many other systems proved what was first conceived by Shevchik [56, 59–62]. Two examples are presented in Figure 2.14 and Figure 2.15. Figure 2.14 show parts of multiscale simulations of the early stages of Cu growth on a Cu(100) surface using a simplified model with ballistic deposition done by Shim et al. [61]. They were able to show that the final structures on the surface are even dependent on the azimuthal deposition angle (indicated with arrows in each image of Figure 2.14. In 2010 Rabbering et al. published scanning tunneling microscopy images (STM images) of similar growth experiments of Cu on Cu(100) and compared them with simulation of a kMC scheme on a lattice of 512 × 512 atoms which is presented in Figure 2.15 [62].

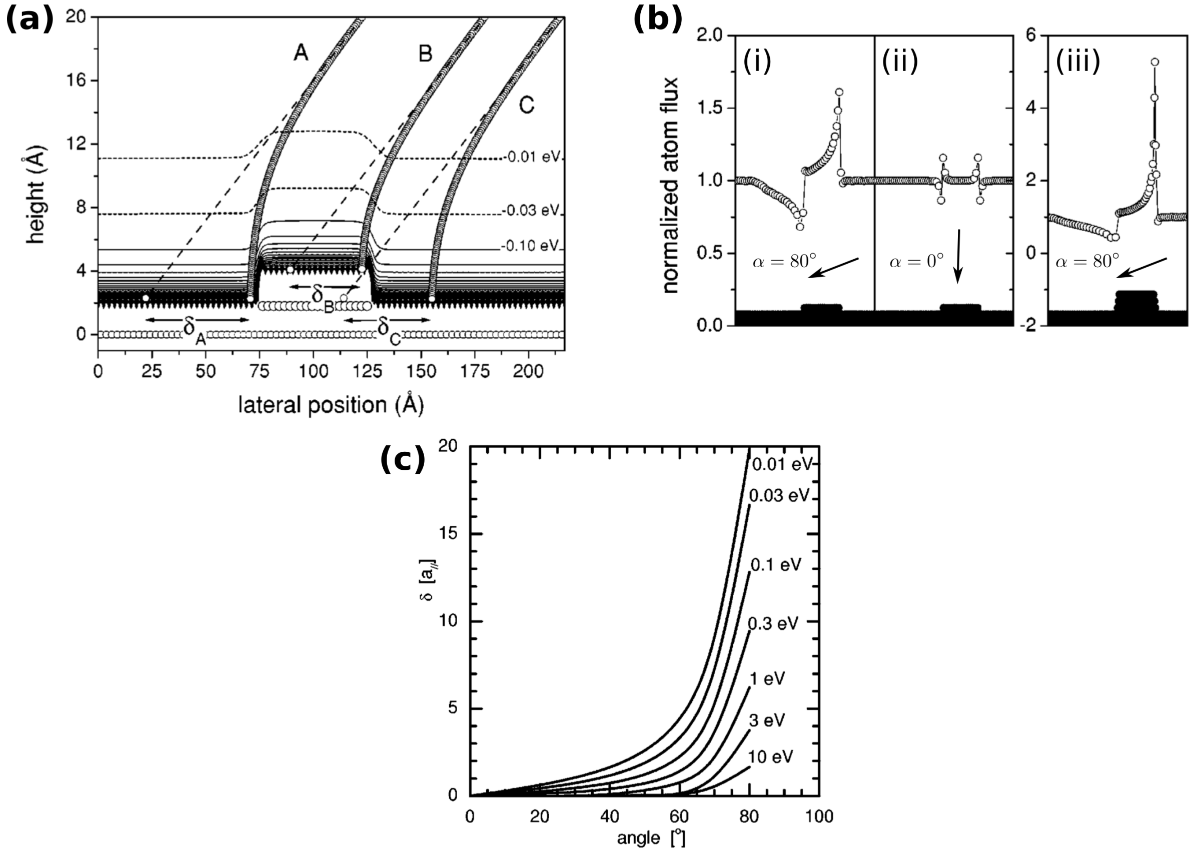

Figure 2.13: (a) Calculated equipotential energy contours and three atom trajectories (A,B,C) for a surface with a one-monolayer-high island on top of it for $\alpha = 80°$ which start at 20 Å above the surface. (b) The deposition rate at the surface calculated and normalized to a homogeneous flux far above the surface: (i) surface with a one-monolayer-high island and $\alpha = 80°$, (ii) with a one-monolayer-high island and normal-incidence deposition, and (iii) with a three-monolayer-high island and $\alpha = 80°$. (From [55]) (c) Energy and incidence angle dependence of the lateral difference in impact position for this case through steering. (From [57])

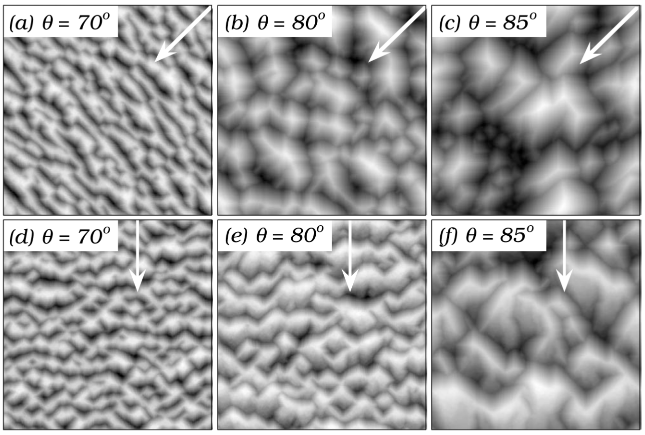

Figure 2.14: Comparison of surface morphology for deposition of Cu on a Cu(100) surface along the [110] direction (top row) with that for deposition along the [100] direction (bottom row) at different deposition angles α and at $\theta =$ 50 ML. Arrows illustrate each deposition direction. It shows that different α and azimuthal deposition directions can influence the metal-metal growth behavior. (From [61])

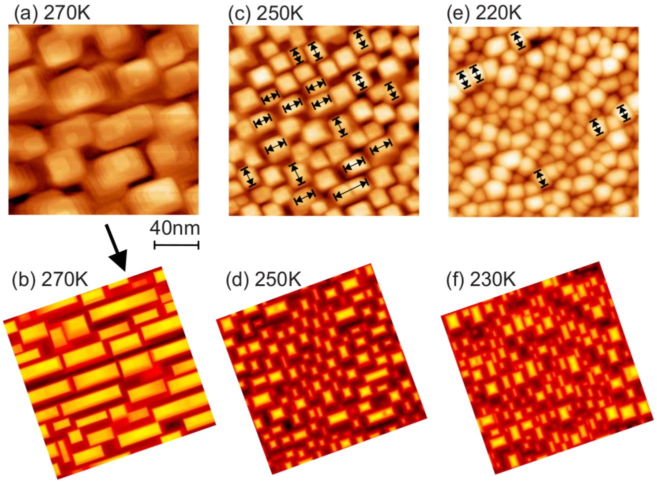

Figure 2.15: Cu/Cu(001) surface morphology result from experiments (upper row, STM topographies) and kMC simulations (lower row) with $\theta = 40$ ML at $\alpha = 80°$ for different surface temperatures. The plane of incidence of the incoming atomic beam is indicated by the black arrow in between pictures and corresponds to the [110] azimuthal direction. The comparison shows a good correlation between experiment and simulation and reveal the influence of temperature. (From [62])

2.2 6P – a semiconducting molecule

The rod-like molecule Para-hexaphenyl (6P, also called Sexiphenyl or Hexaphenyl) which was used within this work is part of the family of the π-conjugated oligophenyls. These molecules are prototypes in organic electronics because of the interesting possibility to prepare thin films of either lying or upright standing molecules [8] and their emission in the blue to near UV-vis spectral region [63–68].
6P consists of six phenyl rings in a para arrangement which results in a rod-like shape (displayed in Figure 2.16(a)). Its basic data are listed in Table 2.3. In the gas phase this molecule can have interring torsional angles of approximately 40° (in Figure 2.16(b) which becomes more or less 0° in its crystalline phase [69] due to attraction forces between molecules in the bulk. It crystallizes in a kind of herring bone structure (compare with the unit cell shown in Figure 2.16(c).

Table 2.3: Fundamental properties of 6P [70–72]

Stoichiometric formula	$C_{36}H_{26}$
CAS Registry number	4499-83-6
Formula mass (amu)	458.59
Density (g/cm^3)	1.288
Melting point (K)	702 – 748
Sublimation enthalpy (kJ/mol)	211
Desorption energy (eV)	2.9 (monolayer) 2.2-2.5 (multilayer)
Band gap (eV)	3.1
Charge carrier mobility (cm^2/Vs)	14 (from [73])
Van der Waals dimensions (nm^3)	$2.85 \times 0.35 \times 0.67$
Crystallographic phase at 300 K	monoclinic
Space group	$P2_1/c$, Z = 2
Lattice vectors a, b, c (nm)	0.81, 0.56, 2.62
Monoclinic angle β (°)	98.2

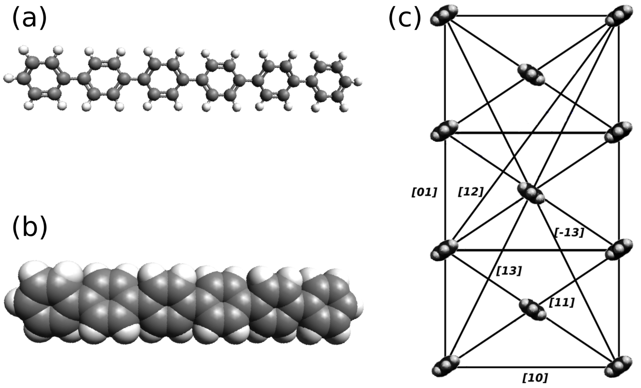

Figure 2.16: (a) The chemical structure of 6P with its six phenyl rings in para arrangement. (b) The Van der Waals spheres shown the molecule in its gas phase with the tilt of phenyl rings out of their molecular plane. (c) The unit cell of a 6P crystal with its herring bone arrangement marked with some of its crystalline orientations [70, 71].

A lot of organic molecules' properties rely on the π-electrons which are according to their energy found either in the lowest unoccupied molecule orbital (LUMO) or the highest occupied molecule orbital (HOMO). Through angle-resolved photoemission spectroscopy (ARPES), the different binding energies for bonding and anti-bonding HOMOs can be visualized for crystalline films of 6P. Figure 2.17 points out the congruence of the ARPES data with different molecule orbitals in real space obtained by density functional theory (DFT) [74].

Former investigations revealed that 6P tends to grow preferably nanofiber structures of lying molecules owing to the anisotropy on crystallographically well ordered substrates (Figure 2.18(a) and (b)), like freshly cleaved mica, Au(111) [75], GaAs(111) [76], Al(111) [77], Cu(110) [78], KCl(001) [79], and In_2O_3(111) [80]. However, such structures are sometimes also found on less ordered substrates like amorphous indium tin oxide [81], as well as different polymers, and heterostructures with others organic semiconducting materials. Such grown thin films provide a nice fluorescence in the blue spectrum and even potential in lasing [66–68]. (Figure 2.18(c)).

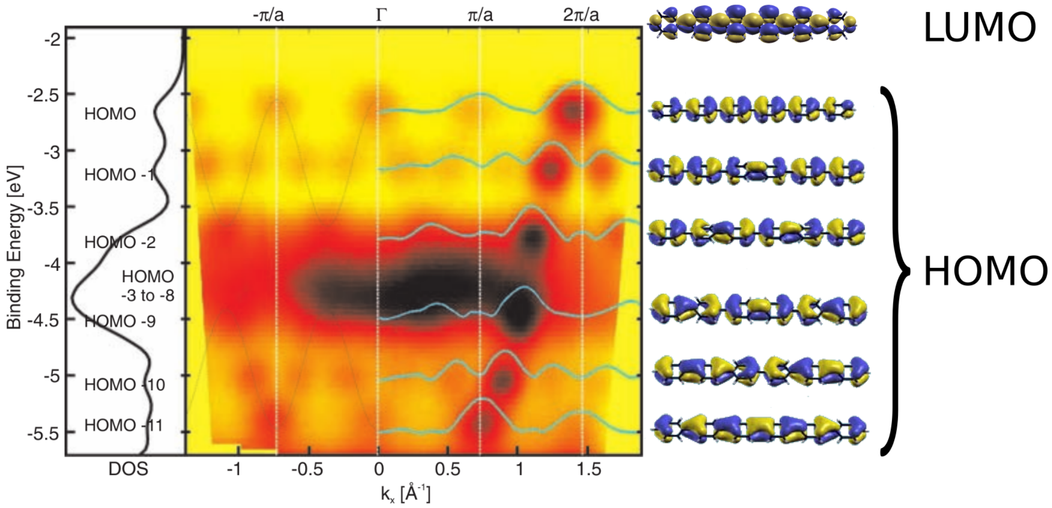

Figure 2.17: The set of ARPES data presented as a contour map. The color scale is linear with highest intensity dark. It shows the binding energy (scaled to the Fermi level of the substrate) to the electron emission momentum (k_x). The density of states (DOS) is on the left with all orbitals enumerated. The Fourier spectra from the DFT-calculated orbitals of an isolated twisted 6P molecule are overlaid on the experimental band map (in turquoise). The corresponding molecule orbitals in real space are on the right (the LUMO structure is only implemented additionally). (Adapted from [74])

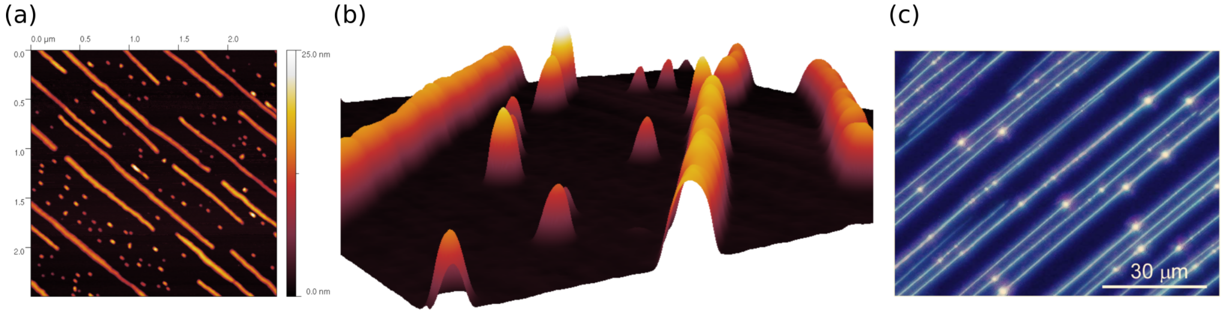

Figure 2.18: 6P nanofibers grown with OMBE under UHV conditions on mica. (a) AFM overview of the morphology of such a 6P film and (b) 3D representation of the same film from [8, 82, 83]. (c) Fluorescence micrograph of Para-hexaphenyl nanofibers deposited on (001)-oriented muscovite mica (from [67]).

Andreev and others have previously shown [8, 82, 83] that 6P can nucleate on amorphous substrates films to compact or dendritic islands consisting of standing molecules which form mounds (like wedding cakes, Figure 2.19(a)) with continuing film growth. Hlawacek et al. [4] found interesting decrease of step heights for the first few layers within the mounds. The first layer is tilted by 43°. In subsequent layers, the molecules are less tilted and after about 4 layers they reach 17° tilt angle with respect to the surface normal [4] (illustrated in Figure 2.19(b)).

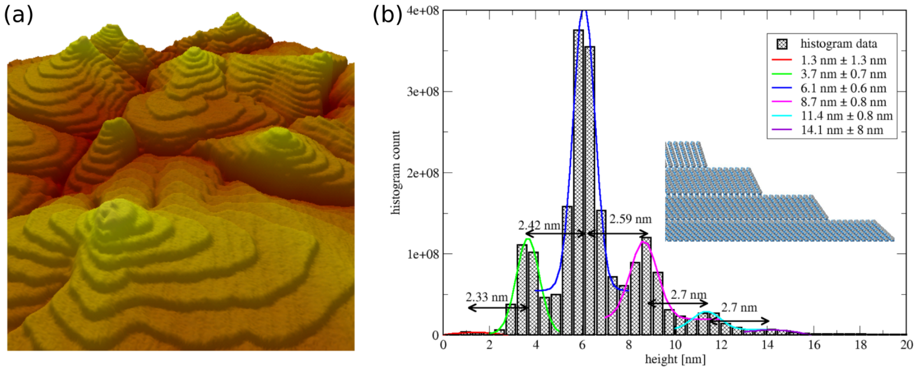

Figure 2.19: (a) 3D representation of the mounded morphology of a 50 nm thick 6P film grown on amorphous SiO_2. (b) Height distribution obtained from a 4 nm thick 6P film on ion-bombarded mica(001). Inset: A sketch of the assumed gradual decreasing of the molecular tilt angle in the first few layers from up (nearly upright standing molecules) to down (more tilted molecules). (Adapted from [8])

Both growth modes mentioned above lead to two completely different fields of applications. While films with lying molecules emit light and therefore offer the use as organic light emitting diodes (OLEDs), films with upright standing 6P molecules can be implementable in lateral organic field effect transistors (OFETs) (see the sketches in Figure 2.20).

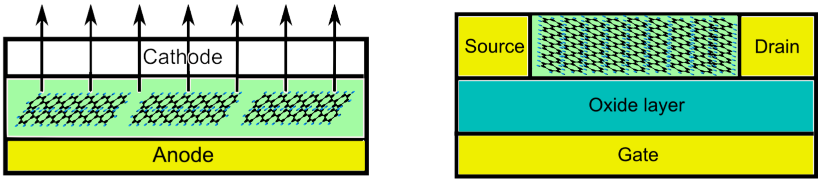

Figure 2.20: Lying 6P molecules between two electrodes can emit light like an OLED (left side). A film of upright standing 6P molecules connecting the source and drain electrodes can form an OFET. The amorphous substrate acts as gate dielectric.

2.3 Substrates

In the beginning it should be mentioned that all substrates which were used for this work have been chosen by the fact to have an amorphous surface. BaF_2 is an exception in this list, but 6P showed there similar growth behavior like on amorphous substrates.

2.3.1 SiO_2

Silicon dioxide (SiO_2) is widespread in nature and exists in crystalline modification like quartz and in an amorphous modification like silica. It is mainly used as insulator material in microelectronics. While quartz is built by well orientated Si-O_4 tetrahedrons, in amorphous silicon dioxide these tetrahedrons have no long-range order (shown in Figure 2.21). Crystalline SiO_2 can have a density between 2.265 g/cm^3 (tridymite) and 2.648 g/cm^3 (quartz) [84]. The density of, e.g., thermally grown amorphous SiO_2 is between (2.15 and 2.25) g/cm^3 [85] and the average length of a silicon oxide bond is 0.162 nm and the distance between the oxygen ions is 0.227 nm [86]. Since the 1950s, SiO_2 plays a major role in the semiconductor technology. Its superior passivating nature made it first choice for electric insulating layers in field-effect transistors based on silicon. This was the most important reason why SiO_2 was selected to be the main substrate material for this work. All SiO_2 samples which were used for growing organic thin films in this work were cleaved from different silicon wafers commonly used in microelectronics industry with a typical surface orientation of (100).

a) Thermally grown oxide onto a common silicon wafer:
   Depending on the kind of usage in producing silicon based microelectronics, two variants of growing silicon dioxide were developed. One method is the diffusion of an oxidizing agent ("wet" oxidation: water or "dry" oxidation: oxygen) into the silicon surface at high temperature in special furnaces where it reacts with the silicon bulk. While the SiO_2 layer grows in thickness, the Si-bulk is slightly thinning. During this method, a high-quality interface between the bulk and the oxide is generated. Here, in the experiments mainly pieces of this kind of wafers with thermal grown oxide were used. Another method uses chemical vapor deposition to deposit SiO_2 layers on top of already existing electronic structures. Industry offers silicon wafers with SiO_2 coverage from a few of tens of nanometers up to six or seven micrometers (standard is 300 nm thickness).

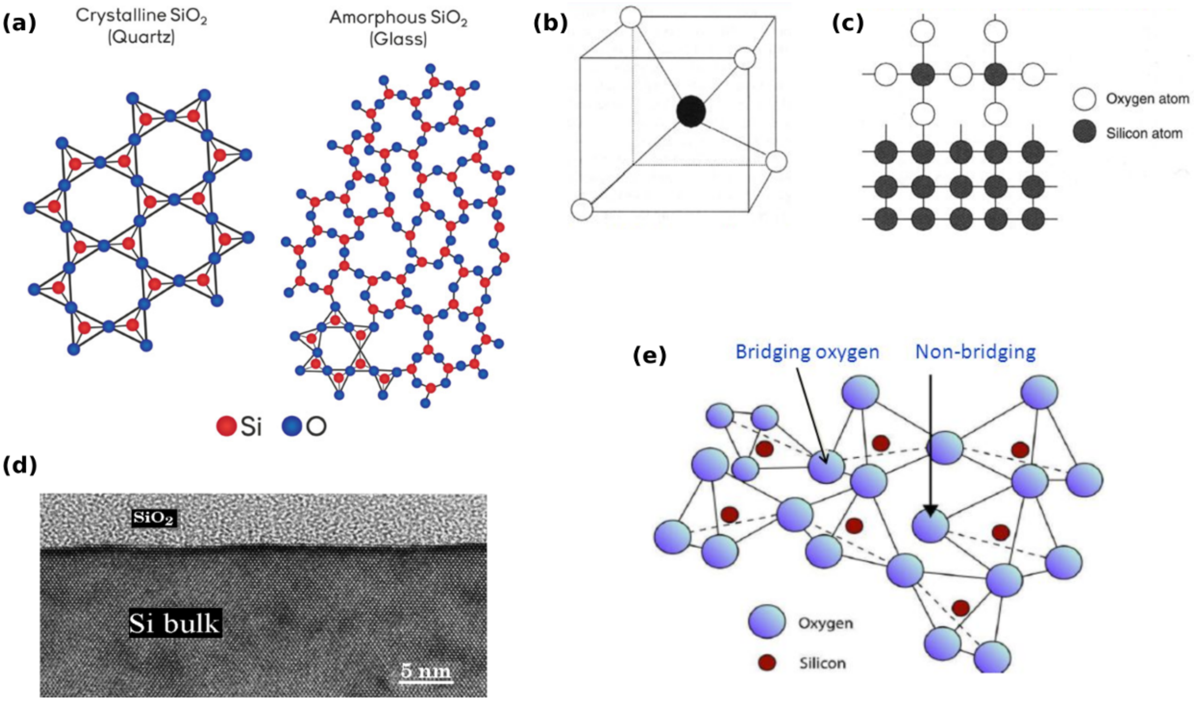
(a)
Crystalline SiO_2
(Quartz)
Amorphous SiO_2
(Glass)
Si
O
(b)
(c)
Oxygen atom
Silicon atom
(d)
SiO_2
Si bulk
5 nm
(e)
Bridging oxygen
Non-bridging
Oxygen
Silicon

Figure 2.21: (a) Comparison of crystalline and amorphous SiO_2 from [87] (b) Unit cell of crystalline SiO_2 and (c) Atomistic sketch of the silicon-silicon dioxide interface from [88]. (d) High-resolution transmission electron microscopy (HRTEM) observation at the bonding interface of hydrophilic Si–SiO_2 bonding from [89]. (e) Three-dimensional sketch of an amorphous tetrahedral network from [88].

b) Silicon wafer with native oxide:
Under ambient conditions, a pure silicon surface is oxidizing by itself. During this natural process, only a very thin layer of SiO_2 is growing. Because soon after the start of this process the SiO_2 layer begins to passivate the silicon bulk so that no more silicon can be oxidized. These layers have usually a thickness of approximately 1 to 2 nm, which is far less than in comparison to thermally grown oxide, but this depends on the growth conditions in air.

c) Plasma etched silicon wafer:
Plasma etching is used on the one hand to clean a surface (of semiconducting materials during their production or metal surfaces for further treatment) and on the other hand to cut trenches in a nanometer range into a surface for microelectronic or micromechanical applications. In a plasma etcher, a process gas is inserted at low pressure and is brought to a plasma state through dielectric breakdown using a high-frequency electric field (in general at a pressure of some tens of Millitorr and a frequency of 13.56 MHz). Typically, oxygen or fluorine-bearing gases are in use as process gas for cleaning, while for etching trenches mostly argon or nitrogen (or similar inert gases) are chosen. Oxygen, because of its reactive behavior, can be even taken for growing an oxide layer onto surfaces. Here in this work, the aim of trying plasma etching was to clean the surface and changing the roughness of the SiO_2 top layer of silicon wafers. Therefore, the samples were only exposed for short time to the plasma in the evacuated chamber of an Oxford Plasmalab System 100.

2.3.2 Mica

Mica is used as a general term for a family of very common rock-forming minerals in the earth crust. It is existing in numerous types – most common are muscovite, biotite, lepidolite, phlogopite, and zinnwaldite. Muscovite mica is especially of interest for the work here, because it is already used in microelectronics as an insolator and has a high ratio of transparency for light. Muscovite mica is part of the group of phyllosilicates which form parallel sheets of silicate tetrahedra with Si_2O_5 or a 2:5 ratio of a monoclinic crystal system (see Figure 2.22(a)). The colleagues associated with the NFN-project from TU-Graz, which sent us samples of 6P grown under UHV conditions for AFM investigations, used muscovite mica with a main plain orientation of (001). The used type of mica consists of potassium, aluminum, silicon, and oxygen with an attached hydroxyl-group on its site ($KAl_2[AlSi_3O_{10}](OH)_2$) [90]. After cleaving, the surface of such a mineral sheet contains potassium ions. This surface is shown in Figure 2.22(b) but without the potassium ions on top. The drawn crystallographic structure is confirmed by AFM images shown in Figure 2.22(c) and more detailed in (d). The further preparation of each sample (before the growth of 6P on it) will be explained in chapter 3.

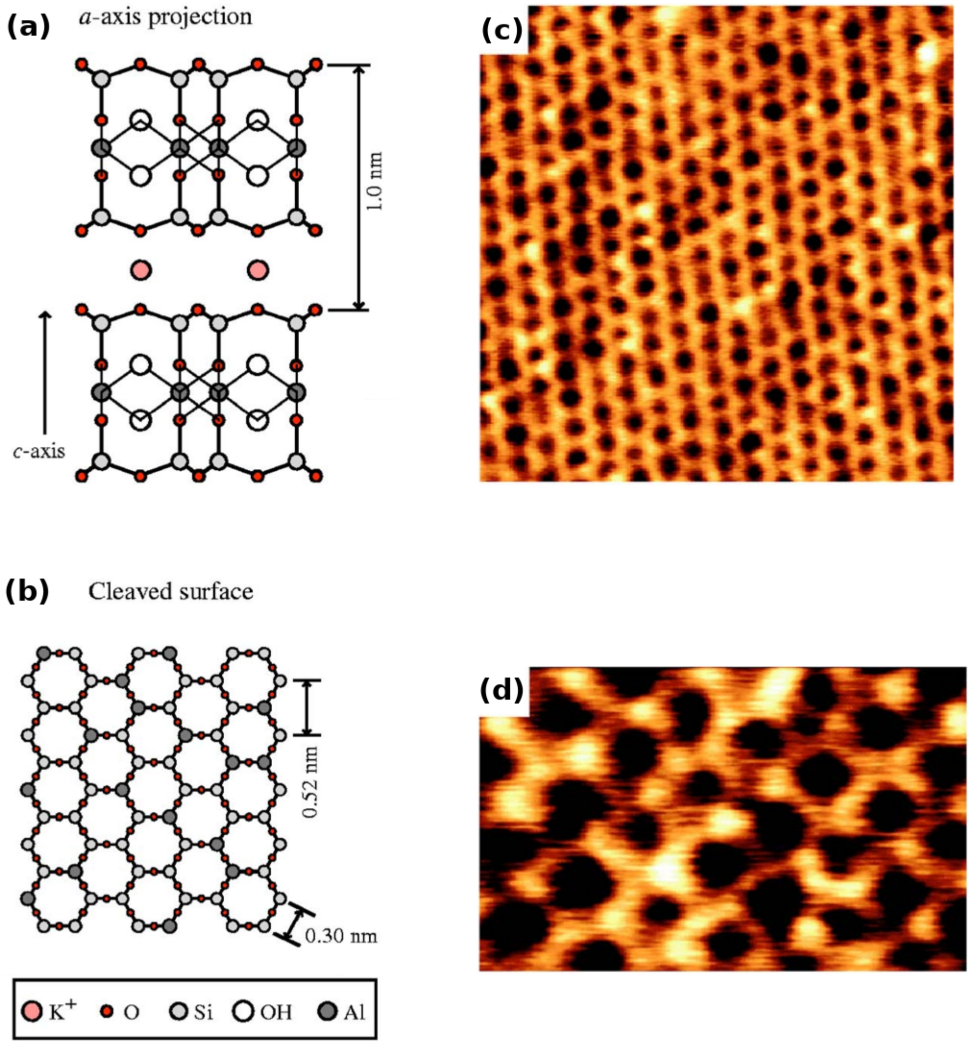
(a)
a-axis projection
1.0 nm
c-axis
(c)
(b)
Cleaved surface
0.52 nm
0.30 nm
(d)
K+
O
Si
OH
Al

Figure 2.22: The crystal structure of muscovite mica; (a) a-axis projection; (b) cleaved surface (K^+ ions are not shown). AFM images of the cleaved (001) surface of muscovite mica taken in water. (c) 8 nm×8 nm; (d) 4 nm×4 nm. (Reproduced from [91])

2.3.3 BaF_2

Barium fluoride (BaF_2) is an alkali-earth fluoride and exists in the solid state as cubic transparent crystals. Figure 2.23(a) shows the unit cell of BaF_2. While BaF_2 has a high transparency for a wide range of wavelengths (from ultraviolet to infrared) it is preferably used as an optical material for windows and lenses (mainly in infrared spectroscopy). Barium and fluorine ions are arranged in an hexagonal array, distributed in trilayers (F–Ba–F), on the $BaF_2(111)$ surface. It can be easily cleaved to obtain an (111) surface. If the cleavage is done with a slight miscut along the $[11\overline{2}]$ direction, terraces with parallel straight steps of about 5 μm occur (shown in Figure 2.23(b)). A cleavage with a slight miscut along the $[\overline{1}10]$ direction leads to more V-shaped terraces with an angle between 15° to 30° on the $BaF_2(111)$ surface (Figure 2.23(c)).

2.4 Deposition technique

In the late 1960s, the successful history of molecular beam epitaxy (MBE) began with the works of J. R. Arthur and A. Y. Cho with highly crystallographic oriented thin films of GaAs by in-situ growth control in ultra-high vacuum (UHV) [92–97]. With MBE, thin films at thicknesses down to an atomic monolayer can be grown. Nowadays, MBE has a wide range of applications, from classical MBE for the deposition of thin film compound semiconductors, metals, or insulators to organic layers (so-called organic molecular beam epitaxy (OMBE)). Mostly OMBE is used for deposition of organic semiconductors, but rather recently it was suitable for desoxyribonucleic acid (DNA) deposition [98]. The principle is very simple. A beam of particles originates in an effusion cell where the growth material is evaporated. The UHV inside the growth chamber offers the possibility that the mean free path of the evaporated molecules or atoms will be longer than the distance between the effusion cell and the substrate. This is preventing the atoms from interacting with each other which provides growth conditions far from equilibrium. The core (filled with the growth material) of the effusion cell is a crucible made of boron nitrid, quartz, tungsten, or graphite where the growth material is heated by heater filaments up to its sublimation point. Commonly used effusion cells are constructed after Knudsen [99–101], like in Figure 2.24(b). The developing of epitaxial layers during growth can be monitored in-situ by mass spectrometers, Auger electron spectroscopy and compact electron diffraction equipment, like reflection high energy electron diffraction (RHEED), or X-Ray techniques.

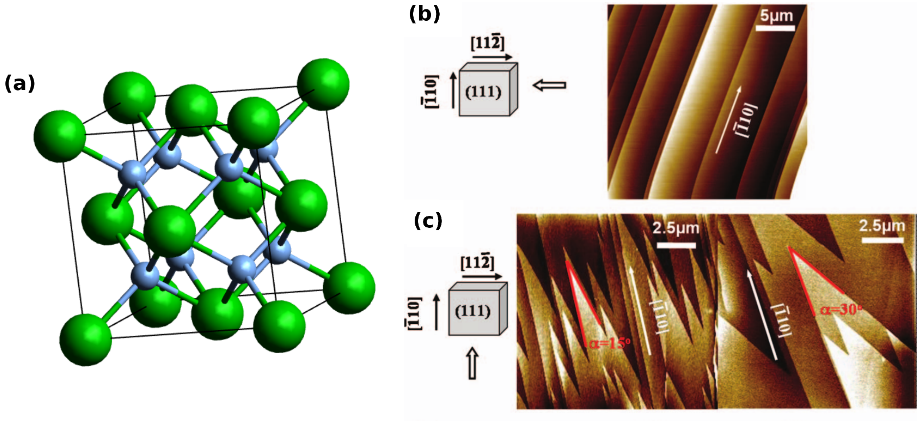
(a)
(b)
[11$\bar{2}$]
[$\bar{1}$10]
(111)
5μm
[$\bar{1}$10]
(c)
[11$\bar{2}$]
[$\bar{1}$10]
(111)
2.5μm
[$\bar{1}$10]
α=15°
2.5μm
[$\bar{1}$10]
α=30°

Figure 2.23: (a) Unit cell of BaF_2 (green: Ba^{2+} ions, light blue: F^- ions); (b) and (c) Topographic AFM images of $BaF_2(111)$ surfaces obtained by cleavage along the [11$\bar{2}$] and [$\bar{1}$10] directions (hollow arrows indicate the cleavage directions). (From [102])

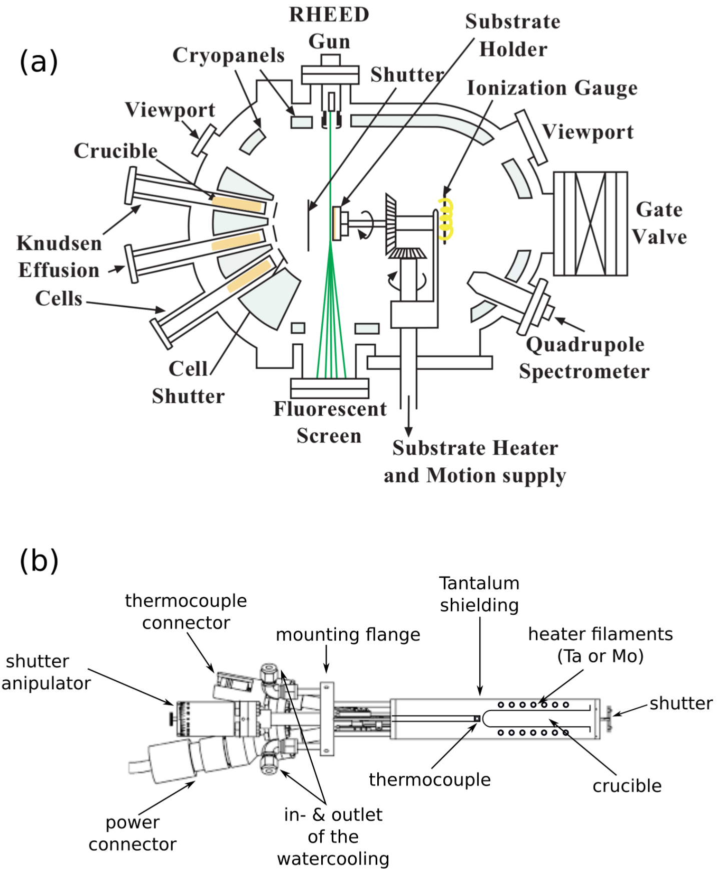
(a)
RHEED Gun
Substrate Holder
Cryopanels
Shutter
Ionization Gauge
Viewport
Viewport
Crucible
Gate Valve
Knudsen Effusion Cells
Quadrupole Spectrometer
Cell Shutter
Fluorescent Screen
Substrate Heater and Motion supply
(b)
Tantalum shielding
thermocouple connector
mounting flange
heater filaments (Ta or Mo)
shutter manipulator
shutter
thermocouple
crucible
power connector
in- & outlet of the watercooling

Figure 2.24: (a) Scheme of a general molecular beam epitaxy growth chamber (From [97]). (b) Schematic drawing of a typical Knudsen cell with a cross section of the main core interior (heater with crucible) adapted from [103].

2.5 Characterization techniques

2.5.1 Atomic force microscopy (AFM)

As main characterization method in this work, atomic force microscopy (AFM) [104] was used which belongs to the scanning probe microscopy (SPM) family. AFM probes the interaction between a sharp probe tip and the surface by interpreting the forces between the atoms with help of Lennard-Jones potentials. Like presented in Figure 2.25, from the Lennard-Jones potential graph two main regimes are obvious as possible working points for the AFM: the contact mode (quasi-static) in the repulsive regime and the non-contact mode (oscillatory) in the attractive regime. This will be discussed in the next sections. Nevertheless, an AFM offers the possibility of measuring all materials, even insulating surfaces (not like a scanning tunneling microscope) at potential resolutions within sub-nanometer scale.

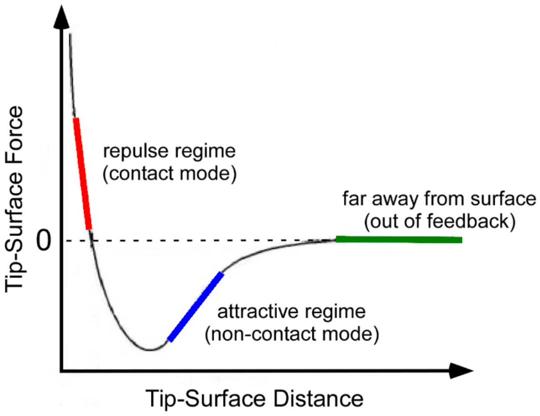

Figure 2.25: Graph of a Lennard-Jones potential describing the interaction between the tip atoms and the surface atoms which indicates the two working regimes for AFM.

In principle, an AFM is constructed in a very simple way. It consists of a small tip at the end of a cantilever mounted to (or is part of) a small silicon chip (Figure 2.26(a)). The cantilever has the function of a spring and is more or less easy to bend which depends on its spring constant. This bending results from the tip-sample interaction forces when the tip is moved across the sample by piezoelectric step motors. To record the cantilever deflection due to topography changes on the samples surface, a LASER beam is reflected from the back side of the cantilever into a position-sensitive detector – a four-section split photo diode. Small deviations of the LASER-beam position, caused by the bending of the cantilever, are recorded as an electric signal. The deflection of the cantilever as the tip is scanned across the surface is continuously monitored and all corrections of the movement are done by a feed back loop to the step motors. The most frequently used piezoelectric scanners are either so-called tube scanners where the x–y–z-movement is performed by a single piezoelectric tube or linear scanners where x–y–z-movements are independently performed by seperate piezo elements. The general parts of the AFM system are displayed in Figure 2.26(b).

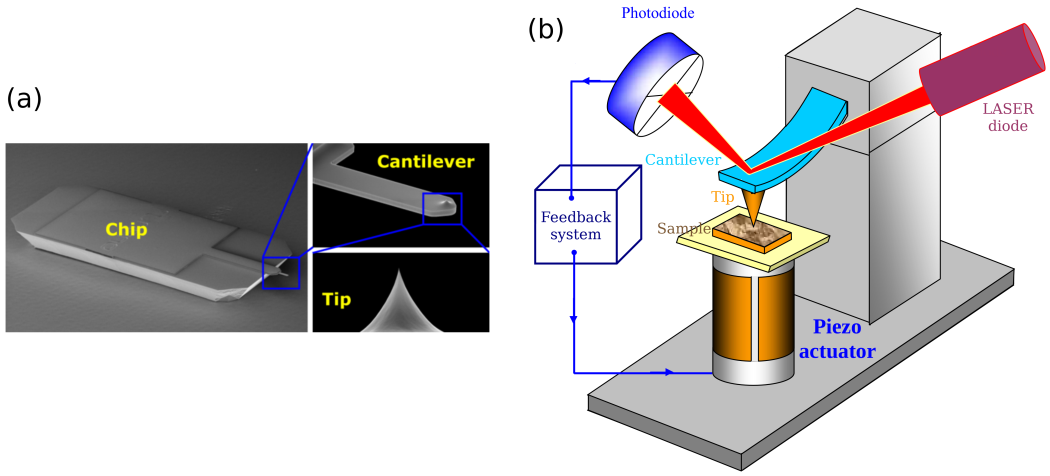

Figure 2.26: (a) An electron microscopic image of the chip with the cantilever and the tip on it from [105]. (b) The schematic overview of a typical AFM system from [106].

Contact mode

In contact mode, the tip is in direct contact with the surface and the forces of repulsion and attraction are counterbalanced by the bending of the cantilever. This needs soft cantilevers with small stiffness. The two main procedures are described as scanning at a “constant force” or at “constant average distance” towards the sample (through the control in the feedback loop). At “constant force” mode, the system provides a constant value of the interactive force by adjusting continuously the height. The advantage of this procedure is that it is less damaging the surface and/or the tip with a small applied force, but the disadvantage can be that it is depending on electronics with a good feedback loop. In “constant height mode”, the cantilever moves the whole time with the same distance to the surface and the topography is directly received from the deflection of the cantilever. In this mode forces can become high and easily damage the tip and/or

the surface. Further, the tip can lose the contact to the surface while scanning across a deep hollow in the surface. The advantage of scanning in "constant height mode" is that there are less feedback artifacts, because the height is measured directly.
So due to the strong mechanical interaction – especially potentially high lateral forces – the contact mode may damage easily the tip and/or the surface. It is possible that the tip begins to push soft materials around, like organic molecules or biological material, on the substrate.

Friction Force Microscopy (FFM)

A special method performed in contact mode is friction force microscopy (FFM) also called lateral force microscopy (LFM) [107, 108]. For this mode the fast scanning direction of the cantilever is in direction perpendicular to its long axis. Frictional and adhesive forces between the tip and the surface make the cantilever torsionally twisting about its long axis which can also be detected by the four-section split photo diodes of the detector. As shown in Figure 2.27 (a) the cantilever torsion results from different frictional forces due to different materials or from the sample topography. However, the topography induced torsion just changes sign when changing from trace to retrace scan direction. By subtracting the friction force image for trace from that of the retrace direction, the topographically induced torsion is canceled out and only the material difference related friction is obtained.

In Figure 2.27 (b) transverse shear microscopy (TSM) is presented [110]. Here, the fast scan direction is along the cantilever's long axis, but again the torsion of the cantilever is recorded. The torsion in this case is related by the shear response of the substrate to the force exerted by the AFM tip. For crystalline organic thin films this shear is related to the local orientation of the molecules within the film. Thus, TSM offers a possibility to distinguish the azimuthal molecular orientation within, e.g., a self-assembled molecular layer on the substrate.

Non-contact mode and intermittent-contact mode

During non-contact mode, the tip is not in direct contact with the surface, but the cantilever reacts on attraction caused by van der Waals forces between tip and substrate. Mostly, the cantilever is brought to oscillate at a small amplitude (~ 1 nm) constantly

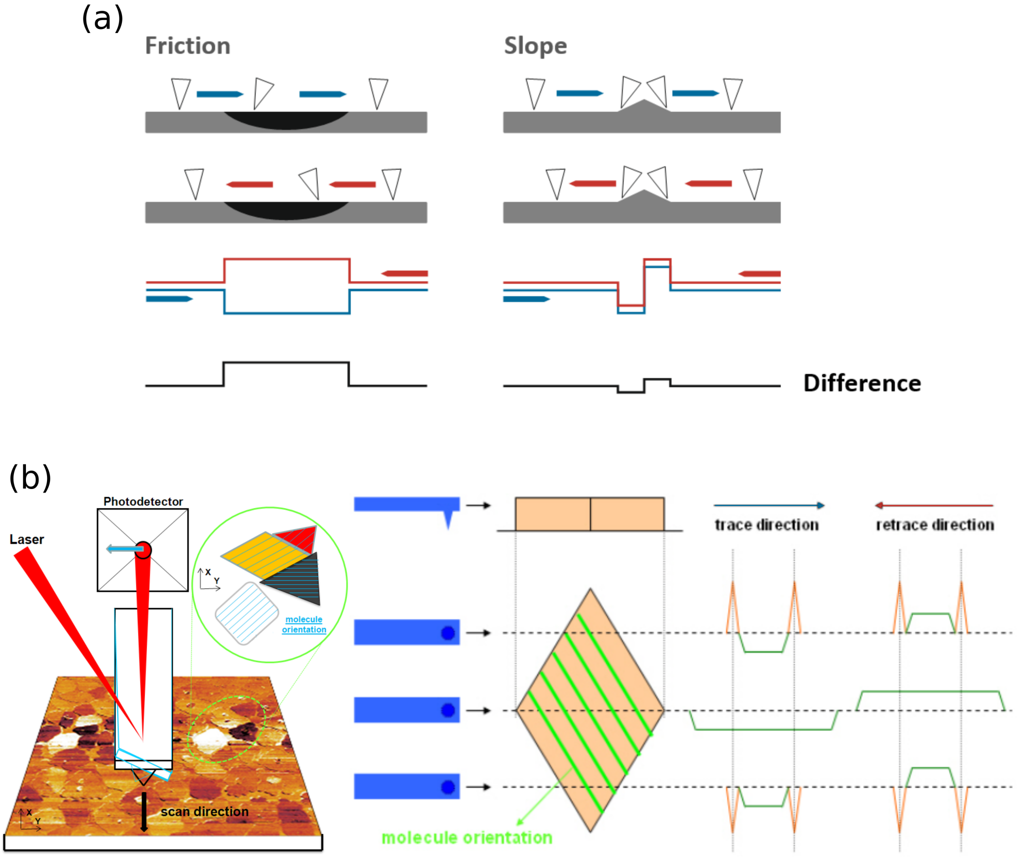
(a)
Friction
Slope
Difference
(b)
Photodetector
Laser
molecule orientation
scan direction
X
Y
trace direction
retrace direction
molecule orientation

Figure 2.27: (a) The sketches show how the signal in FFM should be interpreted in case of moving over structures which differ in material (left) or in height (right) from [109]. (b) The schemes show how TSM works in principle. The arrows indicate in (a) and (b) the scanning directions (blue for trace and red for retrace). (Courtesy by Q. Shen)

near its resonance frequency by a piezoelectric actuator. When approaching, to the surface the tip “feels” more and more the van der Waals forces. Those forces cause a shift – depending on the chosen feedback – in the phase or the frequency of the cantilever. A feedback loop is set to adjust the tip-surface distance in order to keep a user defined phase shift (or frequency shift) constant. The obtained variations in tip-sample distance as function of the lateral tip position can be displayed as topography image. It is mainly performed in UHV to obtain images of a superior resolution, and it deals no damage to the surface.

Intermittent contact mode imaging is the most frequently used imaging technique for AFM. Under ambient conditions a free oscillation amplitude of the cantilever, typically significantly larger than what is used in non-contact mode is set (several 10 nm). When the tip-surface distance is reduced the interaction causes a damping of the amplitude, which is used as feedback parameter. The height adjustments necessary to keep a certain amplitude (for this work typically 50-60% of the free amplitude) is recorded as function of tip position generating a topographical image. In this mode the tip typically gently touches the surface at the bottom of its swing. That is why this mode lies between the real non-contact and contact mode. Often this intermittent-contact mode is called tapping mode. In contrast to contact mode, this mode generates images of the surface morphology without strong damage to tip or sample because of reduced lateral forces. This makes it the most preferable mode in choosing a balanced method for surface investigations of soft matter. Due to the fact that the typical oscillation amplitude is larger than the thickness of a water film present on the surface, it is easy to get well-defined topographic images during measurements even under ambient conditions.

Phase mode imaging

When the tip, operated in intermittent contact mode, moves across materials with different viscoelastic and adhesive properties the forces acting on the tip vary. These variations cause a phase shift of the cantilever oscillation with respect to the oscillation of the driving piezo, which can be recorded simultaneously to the topography image. This way a map revealing local differences in elastic and/or adhesive properties can be obtained [111] (illustrated in Figure 2.28 (b)).

Because of the large difference in mechanical properties of soft organic thin films and

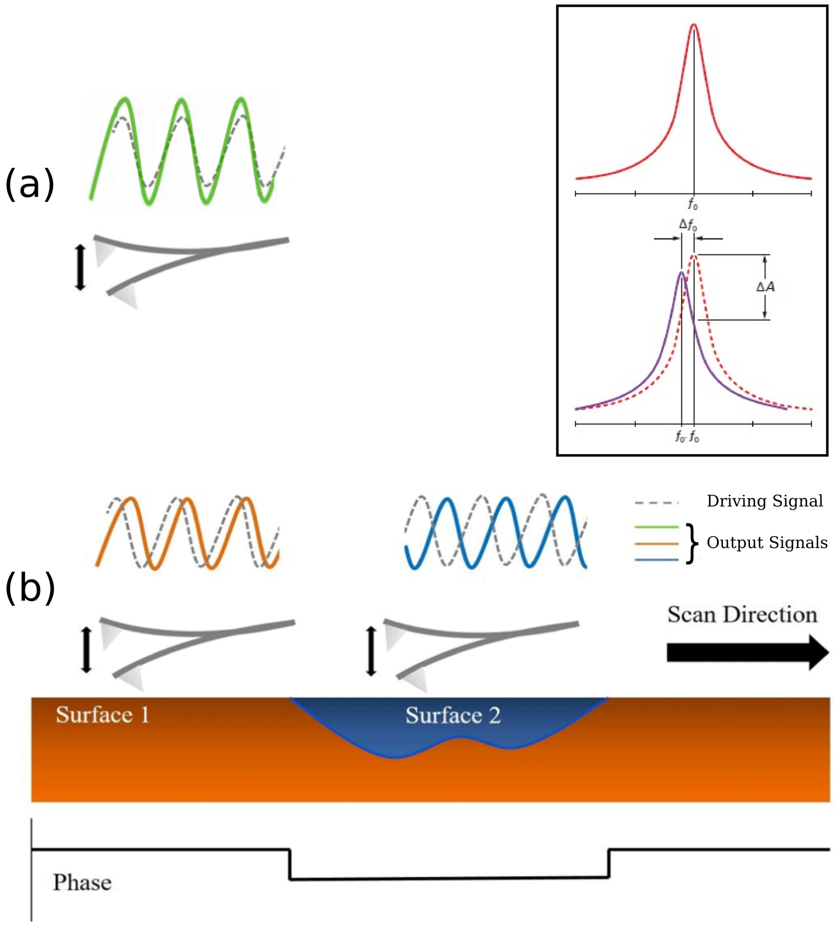
(a)
f_0
Δf_0
ΔA
f_0' f_0
(b)
Driving Signal
Output Signals
Scan Direction
Surface 1
Surface 2
Phase

Figure 2.28: Illustration of phase mode imaging in tapping mode. (a) The cantilever is lifted off the surface in non-contact mode and oscillating with “free” amplitude. (b) The cantilever is oscillating on surface 1 with a reduced amplitude and a small phase shift. During scanning from surface 1 to surface 2 a bigger phase shift occurs. This can be explained by differencies in tip-sample interaction which arise from variation in the adhesive forces and/or different mechanic response of the surface (from [112]). The inset shows an example for a change in amplitude and in frequency of the cantilever before and after contact with the surface where f_0 is the resonance frequency and Δf is the phase shift (from [113]).

(mostly) hard substrates, clear phase images can be obtained without problems (but it is even capable if this difference is not so high). Only one drawback towards measuring of soft materials should be mentioned. During the scan, the tip can be easily contaminated by picking up material which often results in defacement or even in a complete loss of the phase image.

Kelvin Probe Force Microscopy (KPFM)

An additional AFM technique based on tapping mode AFM, is the Kelvin Probe Force Microscopy (KPFM) (in amplitude modulation mode) which was introduced by Nonnenmacher et al. in 1991 [114]. This method is working in a two-pass scheme. In a first step, the topography is recorded in tapping mode. In a second step, the cantilever is lifted off from the surface by a few nm and scans the same trajectory again but with an additional constant height away from the surface with applying the sum of an AC- and a DC-voltage between the tip and the substrate. The amplitude of the cantilever oscillation at the AC-frequency is measured which is induced by the electrostatic force and is proportional to it. the occurring force component at the AC-frequency results from the contact potential difference (CPD) between tip and surface. The lock-in amplifier is tuned to the frequency of the AC-bias. The deflection beam signal is minimized by controlling the DC voltage to match the CPD [115]. The CPD is the work function difference between the material of the tip and of the surface. The KPFM image is a map of the distribution of surface potential (for further detailed information consult [116] and [106]).

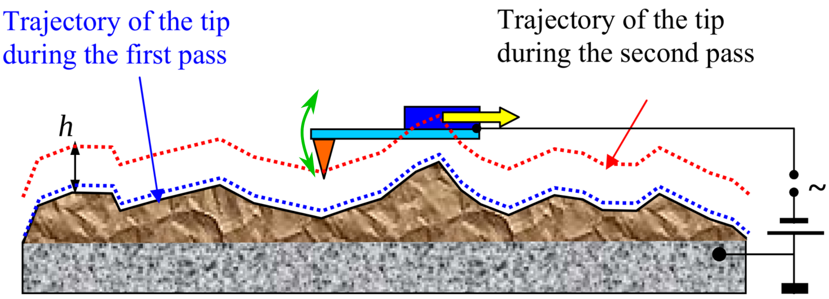

Figure 2.29: Schematic overview of the KPFM measurement as a two-pass technique. (From [106])

2.5.2 Helium Ion Microscopy (HIM)

A helium ion microscope combines the analyzing capabilities of an electron microscope and the structuring and manipulation possibilities of nano–sized features of a focused ion beam with only one source of ionized helium atoms (gas field ion source (GFIS)). For recording images of the specimen with ultra-high resolution, the whole imaging process can be devided in three stages [117, 118]:

a) Helium gas is ionized in the vicinity of a three-atom-sharp pyramidally shaped tip. With an aperture, the ions are accelerated by about 35 keV towards the specimen.

b) Through deflectors and lenses, the beam is controlled and focused before it hits the surface of the specimen.

c) During the interaction of the ions with the specimen secondary electrons, backscattered helium ions, and photons are generated which can be used in imaging and analyzing the material and structure of the specimen.

The advantages over scanning electron microscopy (SEM) are obvious: secundary electrons are generated in a smaller area which increases the resolution, no damage to the specimen from electrostatic charging, surface detail information is enhanced due to physics of signal formation, depth-of-field is about five times larger than the SEM, ...

All this makes HIM an interesting alternative to SEM for investigations of organic semiconducting thin films or organics in general.

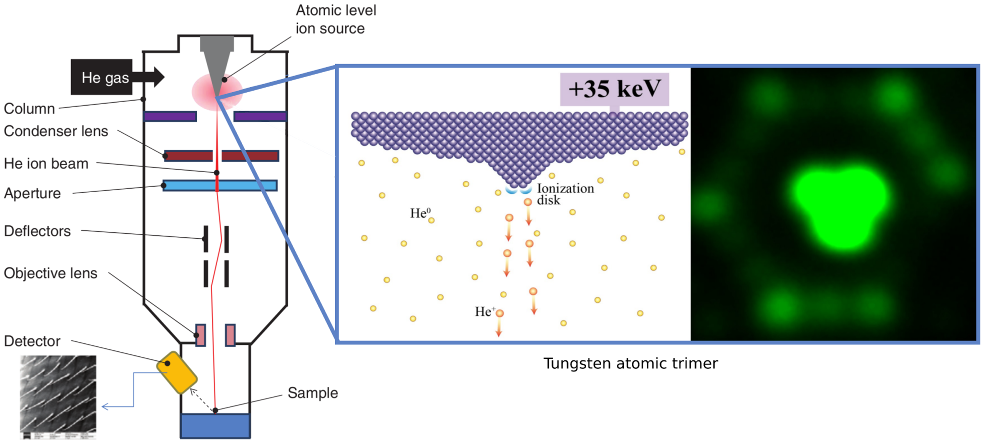

Figure 2.30: Schematic setting of a HIM. Inset: Scheme of the GFIS and the apex of the tip consisting of three tungsten atoms. (Reproduced from [119] and [118]

3 Experimental

3.1 Preparation of substrates

This chapter is addressed primarily to the preparation of samples on SiO_2 substrates which were mainly used for this work. The samples with 6P-films grown on sputtered mica were prepared by Thomas Potocar under supervision of professor Adolf Winkler at the Institute of Solid State Physics, TU-Graz and kindly given to us for AFM investigations. Therefore, the description of the sample preparation made in Graz will be only brief and for further information the reader is referred to the master thesis of Thomas Potocar [90]. Finally, a short number of growth experiments were done on crystalline BaF_2 substrates and their preparation will be only supplementary.

In general, the whole preparation process can be split into two main parts:
a) ex-situ (pre-preparation under ambient conditions)
b) in-situ (concerns the main part – the thermal cleaning of the substrates and growth of thin films in ultra-high vacuum (UHV))

3.1.1 SiO_2

As mentioned before the main material used as substrate were small pieces of silicon wafers (Si(001) covered by SiO_2) which are commonly used in surface science and semiconductor industry. As described in chapter 2.3.1 three different modifications of SiO_2 were used for thin-film growth:
a) Si-wafer with native SiO_2,
b) Si-wafer with thermally grown SiO_2, and
c) Si-wafer with SiO_2 layers which were plasma etched.

In case a) and b), the ex-situ preparation was similar. With a diamond scriber small rectangular pieces of the sizes up to maximum 10x20 mm^2 were carefully cut from an industrially manufactured silicon wafer. These pieces were fixed on sample holders (made of steel, molybdenum, or tantalum) with screws and wires either from stainless steel or tantalum.

Then, the samples on their holders were inserted to a transfer sledge in the load lock of the UHV system. After a pumping and bake-out procedure, the samples were transported to a six-way-cross and from there onward to the growth chamber where the in-situ preparation was performed.

In the growth chamber, a wobble stick was used to transfer the sample holder from the sledge to a homemade electron bombardment heater which was rotatable around one axis. The electrons were accelerated with 1 kV towards the back side of the sample holder. The standard cleaning was done by annealing the sample at about 780 K for 15 minutes. Then the power of the heater was switched off or lowered until the desired temperature of the substrate for the film growth was reached. Most of the growth experiments were done at room temperature (RT) of the substrate. Non-standard procedures will be separately specified for the corresponding samples in chapter 4.

Parallel to the sample cleaning, the Knudsen-cell was slowly brought to a predefined temperature above 500 K (in most cases 523 K) and held there for 20 minutes to get a uniform molecular beam for the growth. Preventing a contamination of the specimen during this process, the shutter of the Knudsen-cell was closed and the heater was turned away by 180° from the evaporator's orifice.

For thin-film growth, the heater with the sample was brought in a position to face directly the orifice of the evaporator. Then a Quartz Crystal Balance (QCB) was positioned next to the heater at the same level of the samples' front for monitoring the increase in film thickness.

Figure 3.1 exemplifies the evolution of the temperature and the pressure during a typical growth experiment of 6P on SiO_2. Most of the time, the UHV system had a pressure around 10^{-9} mbar. The graph in Figure 3.1 shows how fast the pressure rises after starting the heater due to the begin of outgasing of the heater filament. The second peak in the pressure curve during sample heating arises after activating the high voltage source between the filament and the sample to accelerate electrons towards the back side of the sample holder to further increase the temperature. Typically, the specimen needed 80 to 100 minutes to return to RT after annealing. The growth of the 6P film followed right after cooling to prevent surface contamination from the residual gas in the chamber. The next rise in the pressure curve results from ramping up the temperature of the evaporator while 6P already begins to evaporate (but the shutter is still closed). As described above, the temperature of the evaporator was held for a while at a defined value for stabilizing the Knudsen-cell. The film growth took place at a pressure in the range from 5 to $9 \cdot 10^{-9}$ mbar. At the end of every growth procedure first the shutter was closed to immediately interrupt the molecular beam before the evaporator was switched off. If the sample was grown at a higher substrate temperature than RT, the heater was turned off at the same moment when the shutter was closed. All this can be seen in Figure 3.1 by a fast drop of the pressure in the growth chamber.

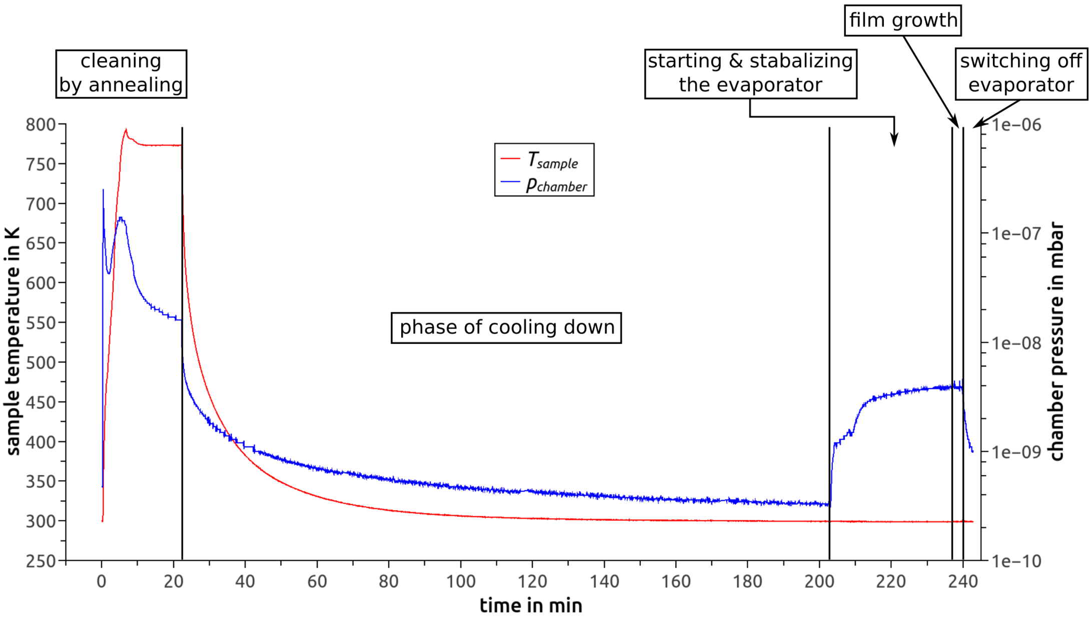

Figure 3.1: Evolution of temperature (red curve) and pressure (blue curve) with time during a typical growth experiment of 6P on SiO_2 at room temperature (RT).

For growth investigations on different SiO_2 surfaces, parts of silicon Si(001)-wafers with native and thermally grown SiO_2 were used. These two kinds of SiO_2 were modified by etching with O_2 plasma at the Chair of Polymeric Chemistry, University of Leoben, Austria with the help of Thomas Griesser and Matthias Edler. Within this experiment, the samples underwent the same preparation like all other samples, but before mounting onto the sample holder they were processed for 15 minutes at about 0.05 mbar with

O_2 plasma in an Oxford Plasmalab System 100, a 100 mm reactive ion etching tool designed for a variety of etches and commonly used in semiconductor fabrication. The O_2 flux was held at 50 sccm[1] for a duration of 5 minutes at 13.5 MHz and 100 W. After plasma treatment, the samples were immediately mounted on the sample holders and transferred to the growth chamber of the UHV system within 15 minutes after the etching process. The time in air between etching and film growth was held as short as possible to prevent contamination (or reconstruction by air-oxygen) of the plasma treated SiO_2 surface. The growth was done as described before (with the following parameters: $p_{\text{chamber}} \approx 8.5 \cdot 10^{-9}$ mbar and $T_{\text{sample}} = 350$ K).

3.1.2 Mica

The samples with 6P grown on sputtered mica were prepared at the Institute for Solid State Physics, Graz University of Technology, Austria by Thomas Potocar. These samples were sent to the Institute of Physics, University of Leoben, Austria for further ex-situ investigations by AFM.

The preparation procedure for the samples from Graz was taken from Potocar et al. [27] and is shortly summarized here (for more detailed information please refer to [90]). First a piece of mica(001) with the size of 10x10x$\sim$0.01 mm^3 was prepared by cleaving a mica sheet with the help of an adhesive tape. To prevent contamination with carbon in air, the sample was attached to a sample holder of steel via tantalum wires and immediately inserted into a UHV chamber after cleaving. Then the surface was sputtered for about 10 minutes by Ar^+ ions at 600 eV at an argon partial pressure of $5 \cdot 10^{-5}$ mbar and a temperature of 110 K. The main process of 6P deposition was done with a Knudsen-cell at a working pressure in the range of 10^{-8} mbar. The substrate behavior during sputtering and growth was in-situ investigated by thermal desorption spectroscopy (TDS), Auger electron spectroscopy (AES), and X-ray photoelectron spectroscopy (XPS) [27].

---

[1] sccm stands for Standard Cubic Centimeters per Minute which is a unit of flow measurement indicating cubic centimeters per minute (cm^3/min) in standard conditions for temperature and pressure of a given fluid. (from https://en.wikipedia.org/wiki/Standard_cubic_centimetres_per_minute)

3.1.3 BaF_2

The BaF_2 samples were prepared by cleaving from a cubic mono-crystal. The final sample size was 15x15x<1 mm^3 and the sample surface was (111) oriented. After a bake-out in the load lock the samples were transferred to the growth chamber, where they were cleaned by heating up to 553 K for 15 minutes, and then thin films of 6P were deposited as described for the SiO_2 samples (described in section 3.1.1).

3.2 The ultra-high vacuum setup

The UHV system at the Institute of Physics, University of Leoben, Leoben, Austria, which was used for the sample preparation, consists of these main parts (see Figure 3.2):

- Load lock (with a rotary vane pump and a turbo molecular pump) for sample transfer without the need to break the vacuum in the main system.

- Six-way-cross for sample transfer from the load lock to the main system. A turbo molecular pump, rotary vane pump and an ion getter pump are mounted together with an ion gauge for pressure measurement to the six-way-cross.

- Growth chamber with a Quartz Crystal Balance (QCB), a wobble stick, a home-made heater (for sample transfer and passive cooling it can be lowered and the sample can be rotated manually for 360° from outside around one axis), an evaporator (water-cooled Knudsen-cell [99–101]) with a shutter able to open/close mechanically by a manipulator from outside).

- Omicron RT-AFM with an Anfatec controller, a wobble stick for sample transfer, a second ion getter pump and an ion gauge. This offers the ability to run the in-situ AFM measurements self-sustaining in UHV by separating this part from the rest of the system.

Figure 3.3 illustrates the refilling procedure of the Knudsen-cell. Therefore the evaporator needs to be disassembled from the UHV system. Before putting new 6P into the quartz glass crucible, it must be cleaned very well. The crucible, the thin tantalum net and all parts of the tantalum shield were cleaned for several minutes in “Caro’s acid” (peroxymonosulfuric acid H_2SO_5, a solution made from concentrated sulfuric acid mixed

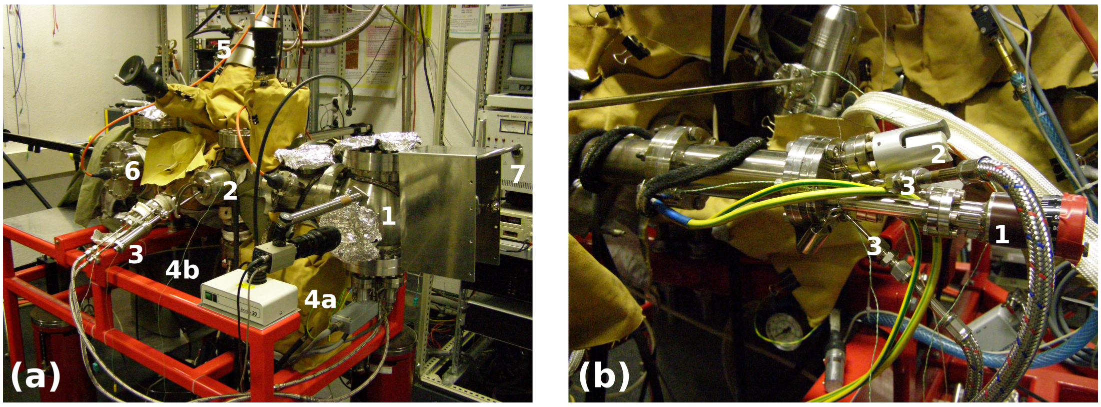

Figure 3.2: (a) UHV system at the Institute of Physics, University of Leoben, used in this work (1...in-situ Omicron AFM, 2...growth chamber, 3...Quartz Crystal Balance with its water cooling tubes, 4a & 4b...two ion getter pumps, 5...turbo molecular pump, 6...six-way-cross, 7...power supply for the electron bombardment heater; load lock, evaporator and rotary vane pumps are in the rear and not visible on the image). (b) A detailed image of the evaporator containing the Knudsen-cell mounted to the UHV system (1...manipulator for the shutter, 2...connector for the thermocouple, 3...feedthroughs for the water cooling; the power connector is not visible on the image).

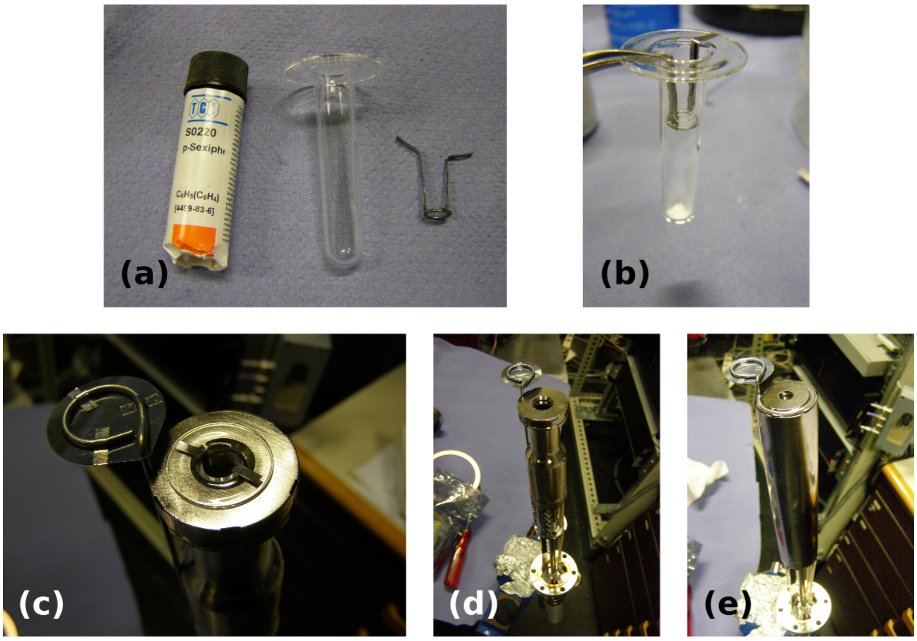

Figure 3.3: Reassembly of the evaporator after cleaning and refilling of the Knudsen-cell. (a) Phial with 6P powder, quartz glass crucible & thin metal net with holder made of tantalum. (b) Refilled crucible. (c) Crucible back in its position in the heater of the evaporator. (d) Evaporator without crucible and tantalum shield. (e) Reassembled evaporator with its tantalum shield.

with hydrogen peroxide) with the help of Thomas Griesser (Chair of Polymeric Chemistry, University of Leoben, Austria).

For the deposition at grazing incidence, the geometry of the heater resulted in a shadowing effect for the molecular beam on the sample. Like presented in Figure 3.4(a), the side mounting plate of the heater can block the molecular beam if the heater is rotated by a very small angle towards the evaporator's orifice in order to realizing very high deposition angles. To bring the sample surface onto the same level of the side mounting plate, the whole geometry of the heater and the sample holders had to be revised.

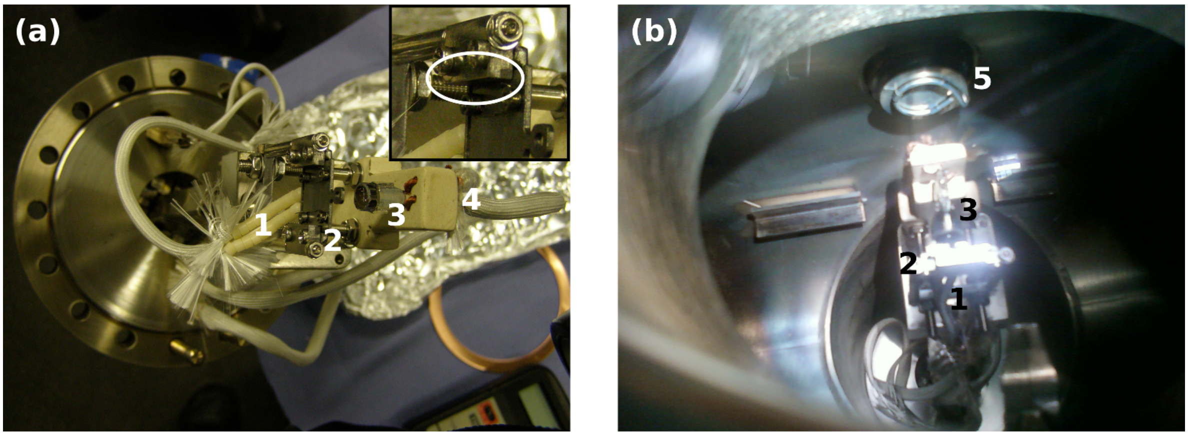

Figure 3.4: (a) Old version of the home made heater with attached sample holder (ex-situ view). The white circle in the inset indicates where the molecular beam shadowing happens during growth at grazing incidence. (b) New version improved for growth at grazing incidence (view from inside of the growth chamber). 1...isolated cables of the thermocouple, 2...steel mounting with sample holder, 3...heater filament, 4...power cables for the filament, 5...evaporator's orifice closed by the shutter.

The sketches in Figure 3.5 show schemes of the revised construction and the final version installed in the growth chamber is shown in Figure 3.4(b). First the sample mounting level was lifted on the holder which resulted in a too thick metal sample holder. This made the thermal cleaning difficult because of the much higher heat capacity. Due to the lack of an "active" sample cooling, the cooling-down time was much longer as for the original sample holder. The prolonged cooling times would have made the samples prone to enhanced contamination before thin-film growth. Therefore, as much material was milled out from the back side of the new sample holder as was necessary to obtain about the same thickness comparable as the old holder. However, after milling, the contact area between the sample holder and the back plate of the heater was significantly reduced. Therefore, a big part was cut out of the back plate allowing the accelerated electrons to hit directly the back of the sample holder which resulted in a faster heating.

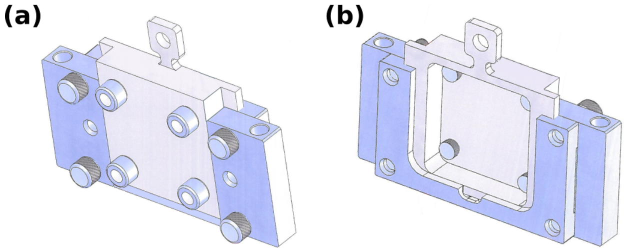

Figure 3.5: Sketch of the new version of the heater (blue) and the sample holder (grey) for growth at a grazing incidence ((a) front view, (b) back view).

While in different UHV systems, the specimen can often be cooled during deposition via Peltier elements or have feedthroughs for “active” cooling with liquid nitrogen, this UHV system here doesn’t offer such possibilities. There is only a slim steel tube coiling around the lower part of the growth chamber (seen in Figure 3.6(b) covered by ice) which allows for cooling the whole bottom flange by purging a cooling agent through it. After the standard annealing, the heater was lowered in the position indicated by **d** in Figure 3.6(b). In this case liquid nitrogen was used for cooling of the flange and the sample was cooled passively down to (280±2) K. For the deposition, the heater had to be put back into the upper position, indicated by **u** in Figure 3.6(b). There, the sample temperature rose up to values of (288±5) K during growth. Figure 3.6 gives an overview of the system setup during growth at temperatures below RT.

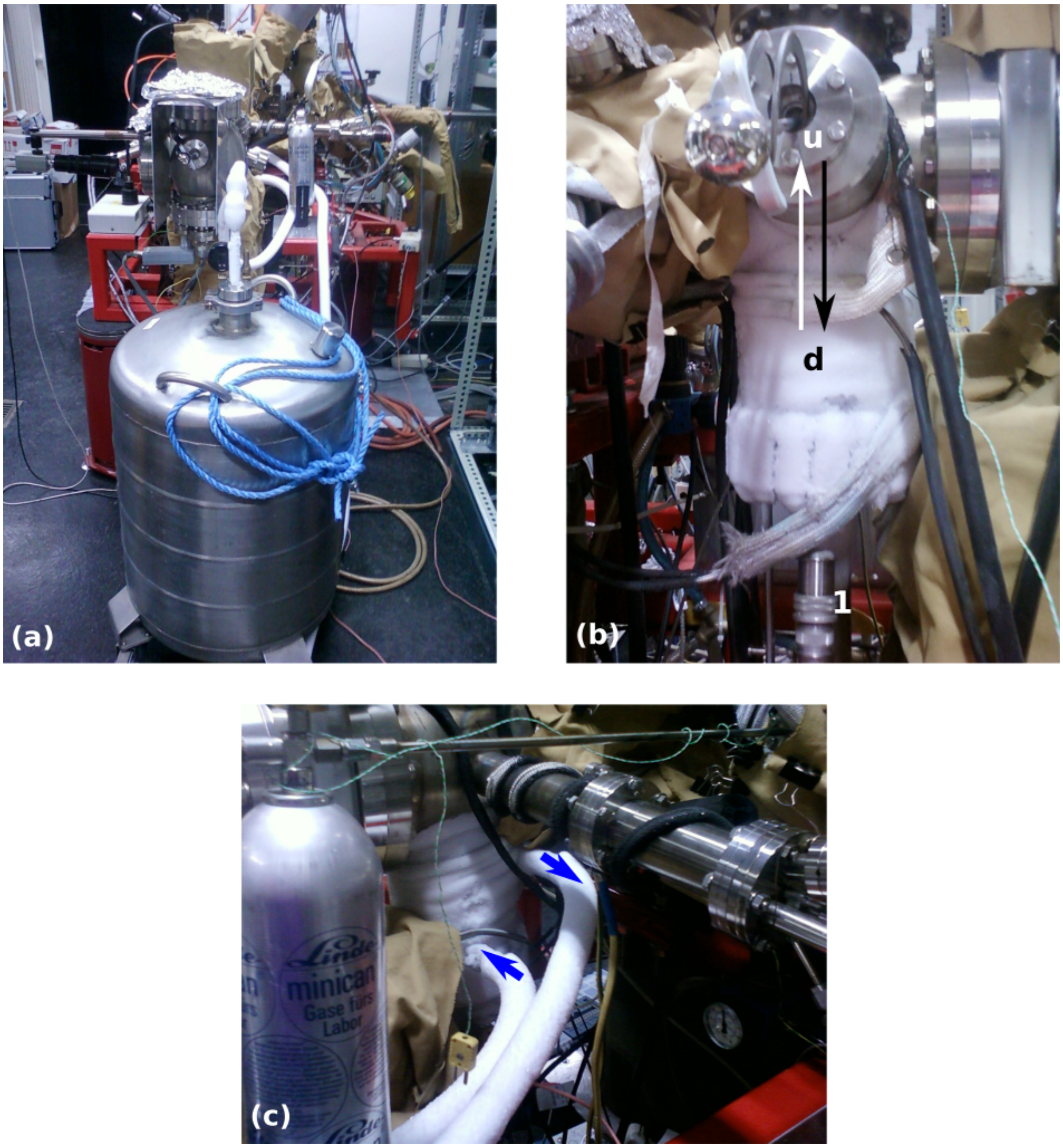

Figure 3.6: Growth experiments with passive cooling by liquid nitrogen. (a) Dewar filled with liquid nitrogen in front of the UHV system. (b) Front view of the growth chamber with its lower part cooled from outside (1...manipulator of the heater; **u** and **d** indicate the approximate heater upper position during annealing & thin-film growth and lower position during sample transfer & passive cooling; white and black arrows indicate the vertical moving direction of the heater inside the growth chamber). (c) Rear view of the passive cooling system (blue arrows indicate the flow direction of the liquid nitrogen).

3.3 Characterization of samples

This section is divided into two parts. The first part deals with the AFM equipment which was applied for characterization of the samples. And the second part deals with the software which was used for further data analysis.

3.3.1 AFM equipment

For characterization three different AFM systems were in use which are situated at the Institute of Physics, University of Leoben, Austria.

Omicron AFM/STM

The Omicron AFM/STM system operating at room temperature equipped with an Anfatec controller is installed in the UHV system. It is used for AFM investigations under UHV conditions. The system can only be operated in contact mode with a maximum scan size of 6x6 μm^2. Figure 3.7(a) displays the main part of the AFM with a slot for the sample holder on one side and on the opposite side a smaller slot for the AFM probe holder. The AFM probes must be glued onto steel holders and put into special transfer holders for the sledge in the UHV system. These transfer holders look similar to the sample holder presented in Figure 3.5 and Figure 3.7(a).

Digital Instruments Nanoscope IIIa Multimode AFM

The AFM which was mainly used for this work was the Multimode AFM with a Nanoscope IIIa controller from Digital Instruments/Veeco (DI) equipped with a AS-130 (J) piezoscanner. Figure 3.7(b) shows this measurement system with an optical microscope attached on top connected with a screen for precise LASER positioning onto the cantilever. It can be employed for different AFM modes under ambient conditions. The possible maximum scan size is 100x100 μm^2 with a maximum vertical deflection of 4.7 μm.

MFP-3D Asylum Research

Some of the images in this work were done with this AFM mostly in comparison or in addition to the before mentioned DI instrument. The MFP-3D offers a maximum scan size of 85x85 μm^2 with a maximum height range in z-direction of 10 μm. Figure 3.7(c) shows the MFP-3D scanner head staying on an operation table with the x-y-scanner. The scanner table can be coarsely moved in x- and y-directions with micrometer screws to reach different positions on the sample. The LASER adjustment and engagement of the cantilevers tip towards the surface are done by thumb wheels on the scanner head.

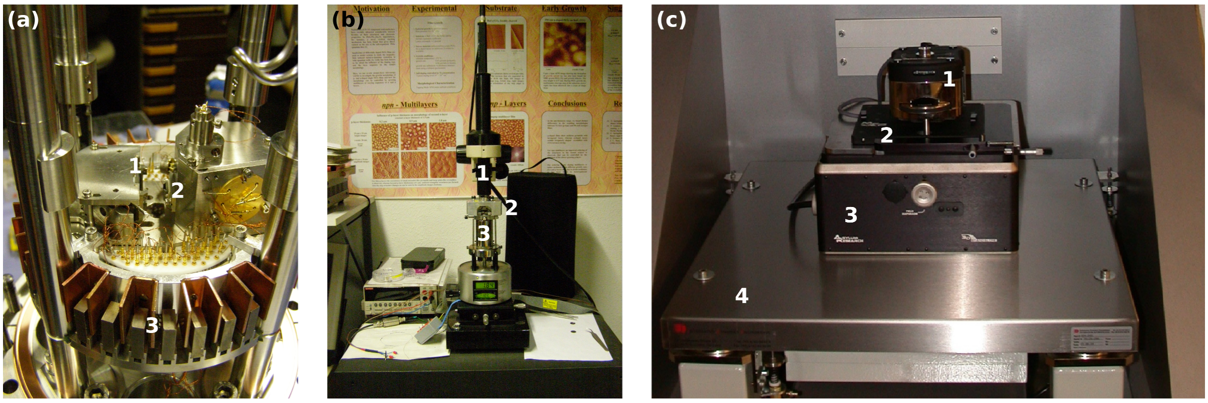

Figure 3.7: (a) Omicron AFM outside of the UHV system during a service maintenance (1...slot for the sample holder, 2...slot for the AFM probe holder, 3...magnetic damping system). (b) Digital Instruments Nanoscope IIIa Multimode AFM (1...optical microscope for LASER positioning, 2...scanner head, 3...AS-130 (J) piezo scanner with the sample on top). (c) Asylum Research MFP-3D AFM (1...scanner head with thumb wheels in front for engaging tip towards sample and on both sides for LASER adjustment, 2...scanner table, 3...AFM base, 4...air-damped table for undisturbed measurement).

AFM probes

Table 3.1 lists all AFM probe types with their technical data which were used for this work. Mostly, the PPP-NCHR probes from NanoSensors (Neuchatel, Switzerland) were deployed to investigate the topography of the 6P thin films.

Table 3.1: List of used AFM probes (data from [1] www.nanoandmore.com and [2] www.ntmdt-tips.com)

Type	Manufacturer	Tip coating	Resonance frequency [kHz]	Force constant [N/m]	Tip radius [nm]	Tips' half cone opening angle [°]	Used AFM mode	
PPP-NCHR	NanoSensors (Switzerland)	None	∼300	∼40	<8±2	10	Tapping mode	[1]
AC160	Olympus/OPUS (Sofia, Bulgaria)		∼300	∼26	<10	<9		[1]
AC240			∼70	∼2	<10	<9		[1]
NSG03	NT-MDT (Moscow, Russia)		∼90	∼2	<10	10		[2]
NSG30			∼320	∼40	<10	10		[2]
PPP-LFMR	NanoSensors (Switzerland)		∼23	∼0.2	<7	10	FFM/TSM	[1]
CSG01	NT-MDT (Moscow, Russia)		∼10	∼0.03	<10	10		[2]
CSG10/Au		Gold	∼23	∼0.2	<10	<10		[2]
DCP11		Diamond (conductive doped with nitrogen)	∼150-250	∼5-12	<100	<10	KPFM	[2]
NSG30/TiN		TiN	∼320	∼40	<10	10		[2]

3.3.2 Software and its usage for characterization

Gwyddion

This program[2] is an open-source software and a great tool for processing the raw data after AFM measurement [120]. It offers different functions to get high-quality topographic images, statistic evaluations of surface parameters (roughness, grain size,...), and data display. For example, to get the topographic images shown in this work, the raw data of every measurement was processed by the same routine. First, a basic line correction function was applied to the data which made that the median of height differences becomes zero. In a next step, a plane was subtracted to level the data. Finally, a subtraction of the background by a polynomial (mostly cubic) forced the start-value of height (zero) down to the lowest point of the surface and corrected even the leveling off plane if there remained some kind of undulation over the image.

QtiPlot

This program is an open-source software and freely available like Gwyddion. It is a cross-platform scientific application for data analysis and visualization [121]. All graphs of data or statistics in this work were plotted with QtiPlot[3].

MATLAB & GNU Octave

MATLAB is a commercial program for various numerical calculations and simulations developed by MathWorks[4] [122]. It offers the possibility for developing own scripts but also provides a huge number of pre-built scripts. In this work it was used for Monte Carlo simulations and together with the script “boxcount.m” to estimate the fractal Hausdorff-dimension of 6P islands. The values from “boxcount.m” were compared with

---

[2] www.gwyddion.net

[3] www.qtiplot.com

[4] www.mathworks.com/products/matlab.html

values calculated from FracLab which is another toolbox in MATLAB for fractal analysis (developed by INRIA, Saclay[5] [123]).
GNU Octave[6] [124] has a syntax which is very similar to MATLAB, but it is open-source and freely available. Unfortunately, not all pre-built functions of MATLAB are compatible with GNU Octave. Here, it was mainly used for (i) the Voronoi tessellation, (ii) the calculation of the parameters for the general Wigner surmise distribution function in CZD and for the scaling distribution function in ISD, and (iii) the execution of least-square fits to evaluate different critical nucleus sizes.
MATLAB and GNU Octave further offer a variety of 2D and 3D plot functions.

Grace

This free 2D graph plotting tool for Unix-like operating systems (Graphing, Advanced Computation and Exploration[7] of data [125]) was employed due to its well-working Levenberg-Marquardt algorithm, which was used to determine the best fit to the distribution of data from measured island sizes and capture zones by Voronoi tessellation within the investigations of critical island sizes.

---

[5] project.inria.fr/fraclab/

[6] www.gnu.org/software/octave/

[7] plasma-gate.weizmann.ac.il/Grace/

4 Results

4.1 Nucleation

4.1.1 Determination of the critical island size

While the approach by Venables [21] to obtain the critical island size i^* needs a whole series of growth experiments using the same amount of deposition material and substrate at different deposition rates R (RE), the ansatz of Amar et al. [18, 25] offers the possibility to obtain the value of i^* faster. Here, i^* can be determined from only one growth at an arbitrary R for different substrate temperatures T, because of using statistical interpretation of a scaled island-size distribution function (ISD), which is described in chapter 2.1.2. Even the enhancement in utilizing the island-surrounding capture zones for ISD by Mulheran & Blackman and Brinkmann et al. [28, 30] shows the improvement against the RE of Venables and ISD was until now in inorganic and organic MBE well established. In 2007 Pimpinelli & Einstein introduced a new approach in using these capture zones to obtain i^* and suggested a generalized Wigner surmise distribution (CZD, see chapter 2.1.2) which revealed a more reliable fit to the distribution of the scaled size of capture zones. Applying this new CZD to OMBE was the motivation to grow 6P on SiO_2 and on mica together with Adolf Winkler and coworkers from the Institute for Solid State Physics, Graz University of Technology (TU-Graz). The results were compared with results obtained from ISD.

In case of 6P on SiO_2, two kind of thin films were grown at room temperature (RT) and at 373 K substrate temperature, both with an approximate coverage of 12 % (or a nominal thickness of 3 nm assuming monolayer high islands of almost upright standing molecules). Both films were grown at a deposition rate R of about 0.03 ML/min for the RT sample and about 0.06 ML/min for the 373 K sample which is in both cases, due to their coverage, a growth in the aggregation regime after Michely and Krug (chap. 2.3.1, p.29 in [126]). The sample preparation was performed like described in chapter 3.1.1

in the UHV system at the Institute of Physics, University of Leoben. Ex-situ AFM investigations using tapping mode led to topographic images (see chapter 2.5.1 section non-contact mode and chapter 3.3.1). Then these AFM images were processed in Gwyddion like described in chapter 3.3.2 and fed to a MATLAB script written to get the distribution of capture-zone area sizes. For this purpose, the script reduces the colors of the image to black and white contrast to make it easier finding the center of mass of the islands. Based on these points the MATLAB routine “voronoin.m” was used to establish the Voronoi tessellation. These calculated areas of the Voronoi-cells needed a rescaling to real image size with a scaling by the normalization of eq. (2.25). Then they were displayed in a distribution graph as a histogram of $P(s)$ with an optimal bin size ν suggested by Scott [127]

$$\nu = 3.49 \cdot \sigma \cdot N^{-1/3}, \tag{4.1}$$

where N stands for the sum of data points and σ is the standard deviation of all scaled capture-zone areas. The factor 3.49 in eq. (4.1) results from using the Gaussian density as a reference standard. Although the Gaussian density is the base of eq. (4.1), this assumption is not so strong that it can even be used for non-Gaussian data. The histogram obtained by the use of this binning will not look Gaussian. Knuth presented in a more recent work another algorithm to calculate the optimal bin size of histograms [128]. He offers a MATLAB script with this algorithm which is based on finding the mode of the marginal posterior probability of the number of bins in a piecewise-constant density function. Using the algorithm of Knuth which was simple to be implemented in the main MATLAB script of this work, it turned out that nevertheless the binning with Scott’s formula in eq. (4.1) was more appropriate to find the best fit of the distribution of capture-zone areas versus their scaled area size. This is due to the fact that Scott’s formula reacts better with the Gaussian decay of the distribution which was then chosen for calculating the bin size in the histograms.

With another MATLAB script the data of the distribution function $P_\beta(s)$ from eq. (2.24) for different i^* and their best least square fit $\langle R^2 \rangle$ were calculated and plotted in the same graph together with the data from the measurement $P(s)$ for better comparison. Finally, this graph was complemented with the best fit of $P_\beta(s)$ towards the measured data using a Levenberg-Marquardt algorithm from the program Grace (already mentioned in chapter 3.3.2).

The following results are based on [129]. Figure 4.1 shows the results of one of seven AFM images which have been taken from a sample grown at RT. While Figure 4.1(a) displays the typical morphology of such a submonolayer film, Figure 4.1(c) gives a detailed view on a single island. The islands are irregularly shaped and have a mean lateral diameter of 500 nm. The average fractal dimension D_{fb} is about 1.98 which means that these are nearly compact islands (which have a fractal dimension of 2). Like in Figure 4.1(a) and (c) visible, some of the islands exhibit already a second-layer island of the same height which is underlined by the height profile in (d). This circumstance is owing to the presence of an effective Ehrlich-Schwoebel barrier for interlayer mass transport (explained in chapter 2.1.1) and already well investigated [4].

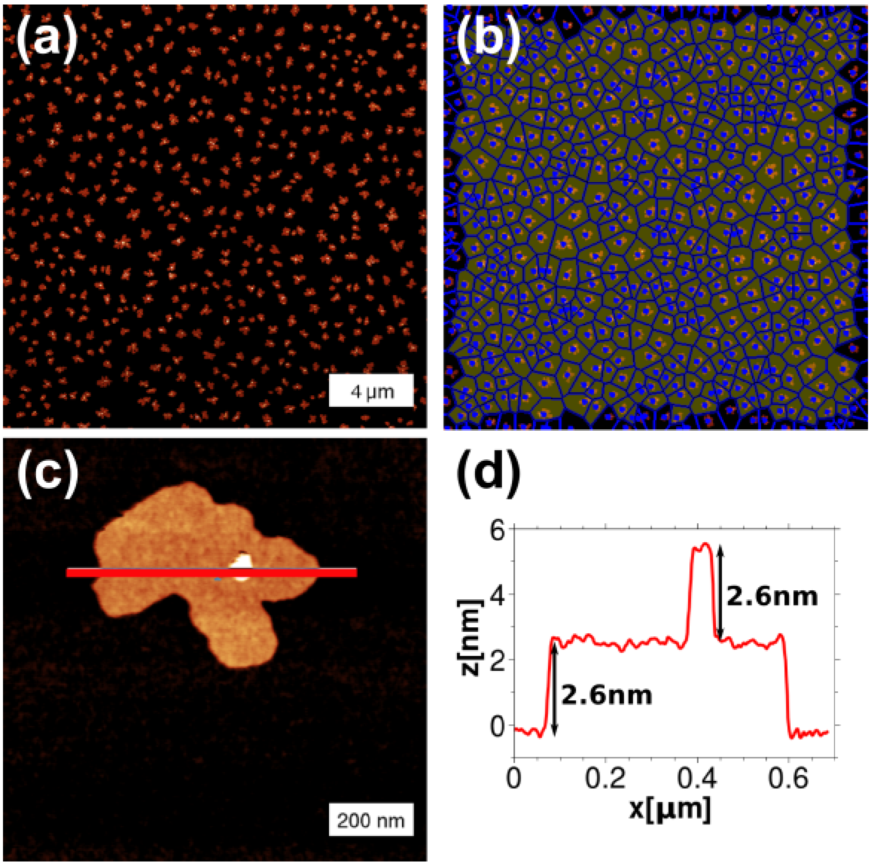

Figure 4.1: (a) One of seven 20x20 μm^2 AFM images of a 6P submonolayer film grown at RT with a z-scale of 5 nm. (b) Original AFM image from (a) masked with the capture zones calculated from Voronoi tessellation. (c) 1x1 μm^2 AFM image from a single island of the same sample. (d) Corresponding height profile represented by the red line in (c). (From Lorbek et al. [129])

Figure 4.1(b) shows an example of obtaining a Voronoi tessellation. Altogether, about 2700 capture-zone areas were determined from seven 20x20 μm^2 AFM images for the CZD analysis and the areas at the rims of each AFM image were already neglected. These images were taken from seven randomly chosen positions of the sample surface. For the comparison with ISD, the island sizes – and not the capture-zone areas like originally proposed by Amar and Family [18] – were taken to get better statistics which were the sum of a bit more than 2700 islands.

The AFM results of the sample grown at a substrate temperature of 373 K are exemplarily displayed in Figure 4.2. While the island density at higher temperature decreases and the average island size increases which is in agreement with the classical nucleation theory (seen in Figure 4.2(a)), the islands' average fractal dimension decreases from 1.98 to 1.75, i.e., becoming more ramified compared to room temperature growth. This seems to be in contradiction to classical nucleation, but Yang et al. observed such a behavior for the same system in 2008 and explained this with another growth mechanism that stable compact islands are formed by the dissociation and reorganization of the metastable disorder film [130]. Figure 4.2(c) and (d) demonstrate – like in the case of RT growth – that the islands consist of nearly upright standing 6P molecules.

While in Figure 4.1(b) the original AFM image was masked by the Voronoi tessellation, in Figure 4.2(b) the binary image for the MATLAB script was masked to provide the reader an impression of the procedure calculating the Voronoi-cells. In both images (but maybe better visible in Figure 4.2(b)) the center of mass of each island is marked with a blue point. Here, five 100x100 μm^2 and eight 85x85 μm^2 AFM images were analyzed from randomly chosen positions. However, due to the low island density only about 250 capture-zone areas were suitable for CZD analysis. Even in this case, the CZD analysis was compared with the result of an ISD analysis. For ISD analysis, about 430 islands could be taken into account which means a significant improvement of statistics.

In a first approach, expecting a pure diffusion limited growth, within CZD the variable β was set to $i^* + 2$, like proposed in [20] with which all calculations were performed to obtain the graphs in Figure 4.3(a)&(c). With the appropriate island numbers, like mentioned before, the results of ISD analysis are presented in Figure 4.3(b)&(d). For the overlaid fits for several i^*, the ISD functions were calculated with values from Table 2.1 (see chapter 2.1.2) for C_{i^*} & a_{i^*} and the CZD functions were obtained by using the values

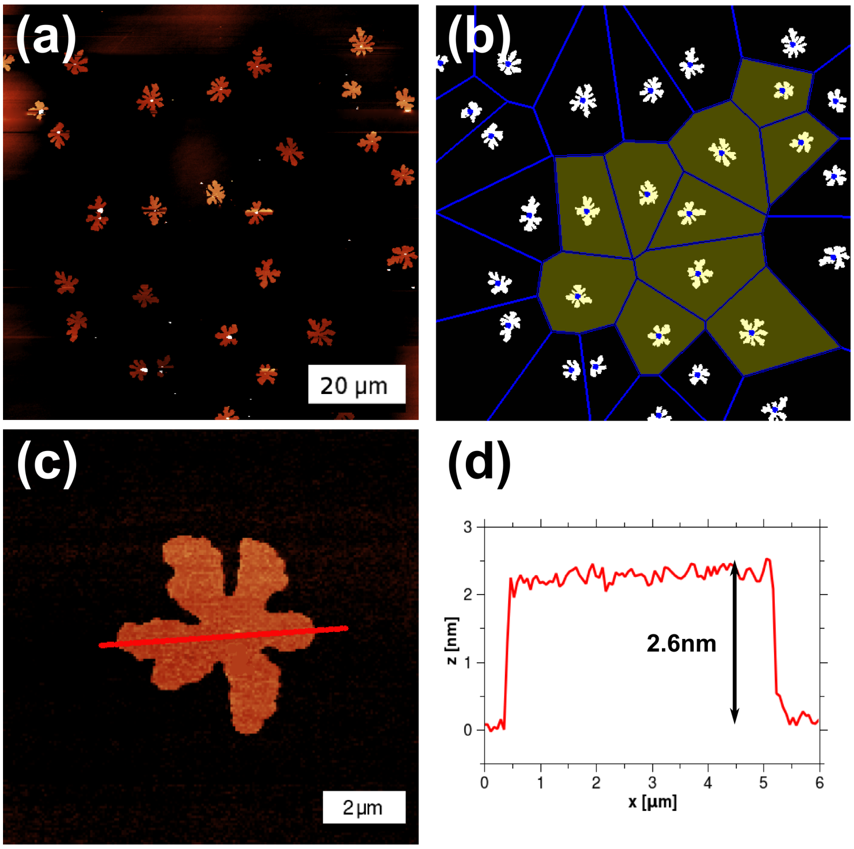

Figure 4.2: (a) 85x85 μm^2 AFM image of a 6P submonolayer film grown at 373 K, z-scale 5 nm. (b) AFM image from (a) after processing with MATLAB masked with the capture zones calculated from Voronoi tessellation. (c) 10x10 μm^2 AFM image from a single island of the same sample. (d) Corresponding height profile represented by the red line in (c). (Adapted from Lorbek et al. [129])

for a_β & b_β from Table 2.2 (chapter 2.1.2).

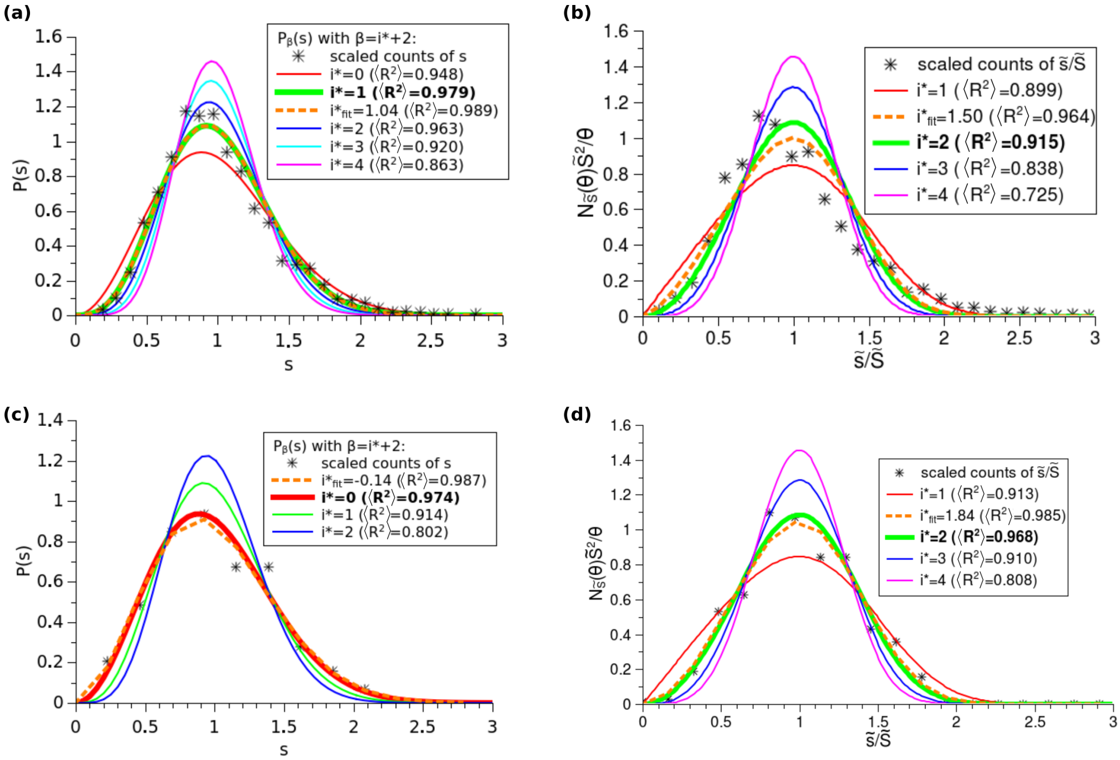

Figure 4.3: Upper row shows the (a) capture-zone and (b) island-size histograms obtained from the 6P film grown at RT on SiO_2. In both cases, a data set of about 2700 values were analyzed separately from each other by the model of Pimpinelli-Einstein [20] and Amar-Family [18]. The lower row shows the (c) capture-zone histogram obtained from 250 Voronoi-cells and (d) island-size histogram using 430 6P islands from the sample grown at 373 K on SiO_2 and their analysis with each model. The overlaid fits for several i^* were computed from the distribution functions of the two models for comparison. The dashed line is the best least square fit to the data of the histogram. The thick line marks the selected i^*. (Reproduced from Lorbek et al. [129])

While the ISD analysis for RT growth yields an i^* between 1 and 2 with a direct fit to the data, the better $\langle R^2 \rangle$ is obtained for the ISD function with $i^* = 2$. After the model of Amar and Family, in this case three molecules must form a stable nucleus. According to the best fit of $i^* = 1.5$, the stable nucleus can have two or three molecules. Comparing with the result of CZD this is in good agreement, because there $i^* = 1$ results in a stable nucleus of two molecules. As shown in Figure 4.3(a), in comparison with (b) the CZD calculations have a better correlation with the asymmetric data set than the more symmetric function of Amar and Family which was already observed before [19]. At the same time, a similar analysis was performed together with colleagues from TU-Graz for the system 6P on ion-bombarded mica [27]. The analyzing procedure to obtain i^* from ISD and CZD was equal to the one used for 6P on SiO_2. The system 6P on mica obtains the same as observed for the SiO_2 system, that the CZD correlates better with the data set than the ISD. The best fit in ISD yields an $i^* = 3 \pm 1$ and the superior method of CZD leads to an i^* between 2 and 3 for 6P on mica grown at a substrate temperature of 300 K [27]. However, Potocar et al. [27] proved this value of i^* applying rate theory (RE) with the growth of a series at different deposition rates R. Figure 7 in [27] shows a slope of the scaling exponent $\chi = 0.55 \pm 0.05$. Using $\chi = i^*/(i^* + 2)$, results in a value of $i^* = 2.5 \pm 0.5$ which means that a stable nucleus can be a trimer or a tetramer. The result of RE shows again how well CZD works.

Considering the result of the CZD analysis for the growth of 6P on SiO_2 at 373 K substrate temperature, it seems that CZD yields unreliable results. From CZD calculation the fit of i^* is even negative which is physically irrelevant. Therefore, i^* is assumed to be zero. Here, the ISD analysis proves a more useful result of i^* of about 2. Anyway, a value of zero would mean that a single 6P molecule is immobile on the surface acting as a nucleation center for other molecules – a so-called spontaneous nucleation. It can also be understood in the context of heterogeneous or defect nucleation [131, 132]. But due to higher substrate temperature, defects on the surface should not play such a dominant role like at lower temperatures, because the molecules should have enough energy to overcome such defects more easily. A possible reason for the discrepancy between the CZD and ISD may origin in the nature of Voronoi tessellations. Mulheran and Blackman [133] pointed out that a Voronoi tessellation for obtaining the capture-zone areas will overestimate the size of small islands and underestimate the size of large ones. In addition, the capture-zone boundaries are more likely equidistant from the edges of neighboring islands instead of their centers of mass. Popescu, Amar, and Family [134] have shown that the mean-field distributions of dendritic islands have sharp peaks and diverge because of their dependence on coverage. But this is in contradiction to the model of CZD where no dependence of the generalized Wigner surmise was postulated [19, 20]. It seems that the mean-field assumption to derive $P_\beta(s)$ with $\beta = i^* + 2$ cannot be true for the case of ramified islands. Tumbek and Winkler [135] investigated 6P thin films on ion-bombarded mica at substrate temperatures from 150 to 400 K with different deposition rates. Within RE, they obtain two different slopes χ instead of one. This results in two different values of i^* (compare Figure 3 in [135]). They explain this behavior of χ with the ideas of Kandel [35] and Venables & Brune [136] who address this fact to the hindrance of approaching monomers to be incorporated at the island edge because the attachment barrier is significantly higher than the diffusion barrier. During incorporation, the lying 6P molecules which are diffusing on the surface become upright standing and, therefore, need to overcome this attachment barrier. This means for the case of 6P on SiO_2 growth at 373 K that the attachment barrier becomes significantly high that the diffusion-limited growth changes to an attachment-limited growth. In the attachment-limited growth, the slope of χ can be between 0.5 to 2 [135] and its formula changes to $\chi = 2{\cdot}i^*/(i^*{+}3)$ after [35]. In 2014, Pimpinelli et al. demonstrated for upright standing 5A thin films on ion-bombared mica that for the attachment-limited growth the variable β in the $P_\beta(s)$ undergoes a change, too, becoming $(i^*+3)/2$ instead of i^*+2 for a pure DLA driven growth [36]. While χ changes with the fractal dimension D_{fb} of the islands, β remains without effect of D_{fb}. For compact islands with a D_{fb} of 2, the scaling exponent can have two expressions for diffusion-limited and attachment-limited growth [36]:

a) DLA driven growth: $\chi_{\mathrm{DLA}} = \dfrac{2 \cdot i^*}{2 \cdot i^* + 2 + D_{\mathrm{fb}}}$ and

b) ALA driven growth: $\chi_{\mathrm{ALA}} = \dfrac{2 \cdot i^*}{i^* + 1 + D_{\mathrm{fb}}}$.

In Figure 4.4, a redone CZD analysis with $\beta = (i^* + 3)/2$ is presented for the growth of 6P on SiO_2 at RT and 373 K assuming that the growth mechanism is mostly attachment-limited driven. The result of the best fit of i^* in the case for 373 K was expected to be higher (see Figure 4.4(b)). And with a value of $i^* = 1$, it seems to be more suitable within classical nucleation theory by forming stable nuclei of dimers instead of exhibiting spontaneous nucleation at higher temperatures. The calculations were rerun for the sample grown at RT (shown in Figure 4.4(a)) and surprisingly i^* has now a value between 3 and 4 which is much higher than in comparison with the result of ISD (compare Figure 4.3(b)). These calculations were made for this thesis long after publishing [129].

In conclusion, the analysis with CZD is a relative new method based on a generalized Wigner surmise and has high potential for usage in organic thin-film investigations. Nevertheless, it has some problems with using Voronoi tessellation in overestimating the size of capture zones [133]. Due to the fact that it should be distinguished between diffusion-limited and attachment-limited growth, the CZD is a strong tool and its distribution

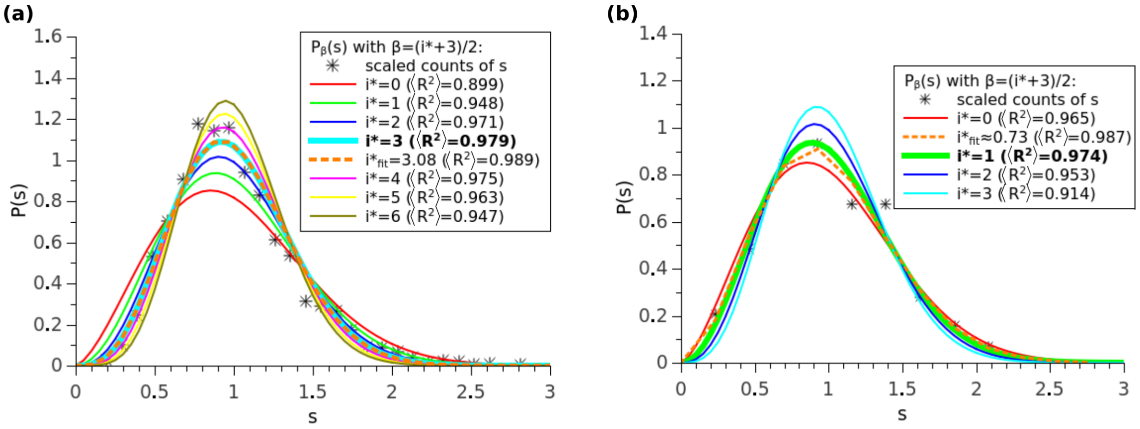

Figure 4.4: Calculations with a new β (expecting attachment-limited growth for 6P on SiO_2) yield new graphs for several i^* in case of (a) RT and (b) 373 K (compare Figure 4.3(a)&(c)). The capture-zone areas for the histograms are still the same. The dashed line is the best least square fit to the data of the histogram. The thick line marks the selected i^*. (From Lorbek unpublished)

function $P_\beta(s)$ provides a better fit to the data sets than ISD. The investigations here lead to an i^* between 1 and 2 in case of RT growth of 6P on SiO_2 and $i^* = 1$ for a growth at 373 K. For investigations of 6P on ion-bombarded mica, i^* is slightly higher and is between 2 and 3 [135]. This means that on ion-bombarded mica a stable nucleus is in general one molecule bigger than on SiO_2. And it seems that the attachment barrier begins to play a major role at higher temperature which is documented in a better fit for i^* according to attachment-limited aggregation (not only at higher deposition rates like stated in [135] for 6P and in [36] for 5A both grown on ion-bombarded mica). So it emerges that at RT the growth is mainly diffusion-limited driven and with higher substrate temperatures a more attachment-limited driven growth scenario is taking over.

4.1.2 Growth on plasma etched SiO_2 surfaces

This part is addressing investigations of the growth morphology of 6P on native silicon oxide and thermally grown silicon oxide surfaces after plasma etching. The specimens of both oxides were etched by O_2 plasma (preparation described in the end of chapter 3.1.1). After 6P growth, their AFM topographic images were compared with images of specimens grown at the same conditions but not treated by O_2 etching.

Figure 4.5 shows the topography of four samples. In all four cases, the coverage θ is 0.15 ± 0.02 monolayers (ML) by virtue of their similar growth conditions. An immediate observation is the difference in island density between the plasma-treated and the not-plasma-treated samples. The etching with O_2 plasma obviously results in a higher density of – consequently – much smaller islands. Even the island shape differs in this way that the islands on non-treated surfaces are more ramified (e.g., compare Figure 4.5(f) with (h)). While the difference between the growth after the plasma etching on thermally grown and on native SiO_2 is not so noticeable, the non-treated surfaces show very well that there is a discrepancy in the island growth. While the number of nucleation sites seems not to differ much, the growth on native SiO_2 produces islands with more dendritic shape than on the thermally grown SiO_2 (compare Figure 4.5(b) with (f)).

A possible explanation for this discrepancy in the island shape may be the thickness of these two different SiO_2 surfaces. The crystallographic structure of the Si(001) through the thinner native SiO_2 can have an influence on the substrate morphology. This may hinder the 6P molecules in their diffusion on the surfaces. While the thermally grown SiO_2 is thick enough that the influence of the Si(001) underneath becomes less and offers the 6P molecules a higher mobility, even for the diffusion along the island edges.

Returning to the difference in growth on plasma-treated and non-plasma-treated samples, it seems that the 5-minutes-etching with O_2 plasma was sufficient to change the morphology of the surface tremendously. The much higher number of nucleation sites on both SiO_2 surfaces indicates that the molecules have a lower mobility across the surface. This is a sign for a roughening of the surface through the etching process. The AFM images in Figure 4.5(c) and (g) show that the etching can abrogate the difference in morphology between the SiO_2 surfaces that a similar growth condition arises on both surfaces. This is even obvious by the similar shape of the islands (compare Figure 4.5(d) and (h)). Tumbek and Winkler found something similar by varying the ion-bombarded time from 3 to 60 minutes [135]. With increasing the ion-bombardment time, the 6P thin film exhibits more smaller islands with a higher island density. Their results underline the hypothesis that either plasma-treating or ion-bombardment changes the morphology of the surface rather than a change of the chemical composition. Therefore, in both cases the increasing roughness of the surface offers for 6P more nucleation sites and is hindering the diffusion of the molecules on the surface.

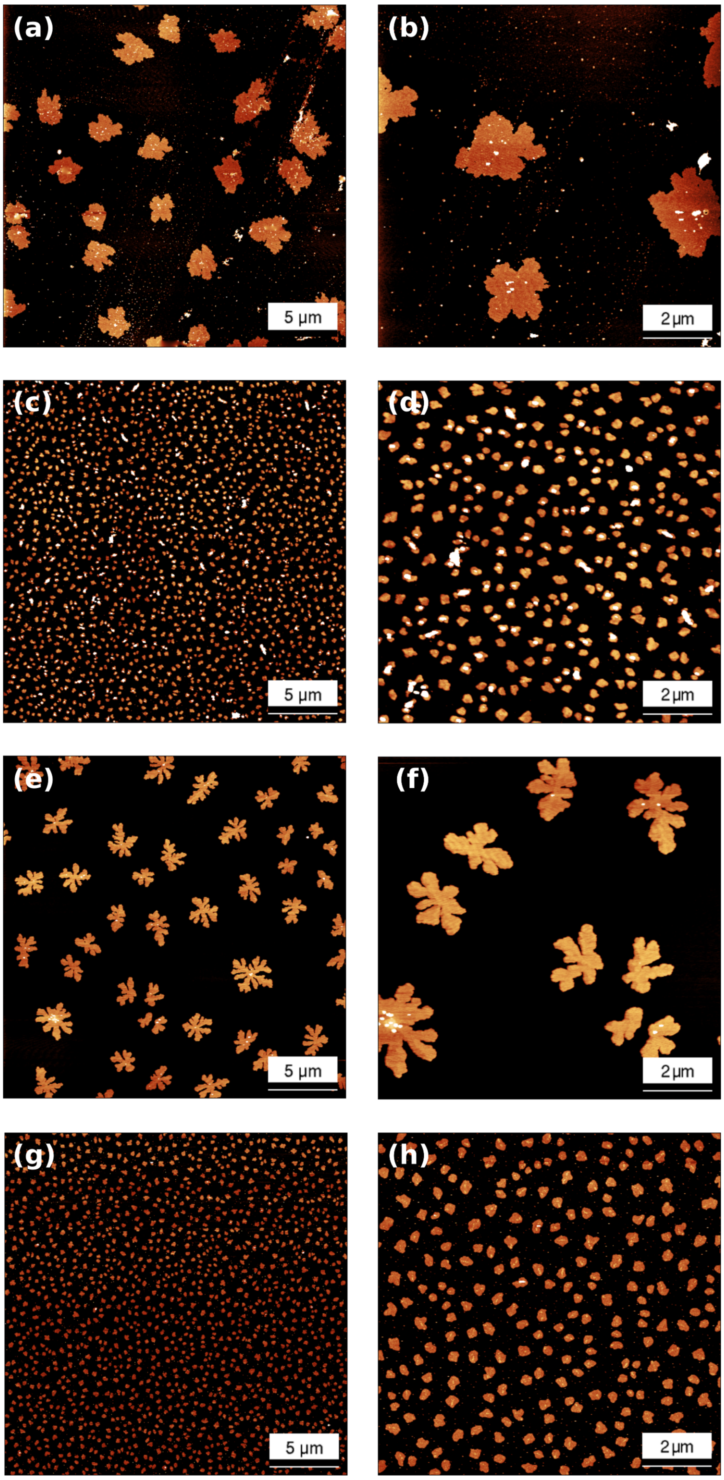
(a)
5 µm
(b)
2µm
(c)
5 µm
(d)
2µm
(e)
5 µm
(f)
2µm
(g)
5 µm
(h)
2µm

Figure 4.5: (a) & (b) 6P islands on thermally grown SiO_2 without plasma etching. (c) & (d) 6P on thermally grown SiO_2 after plasma etching. (e) & (f) 6P on native SiO_2 without plasma etching. (g) & (h) 6P on native SiO_2 after plasma etching. (a),(c),(e) and (g) are 25 x 25 μm^2 AFM images. (b),(d),(f) and (h) are detailed 10 x 10 μm^2 views of (a),(c),(e) and (g). All AFM images have a z-scale of 4 nm.

4.1.3 Growth on SiO_2 after different thermal cleaning procedures

Most samples of 6P growth on SiO_2 were prepared with the same standard procedure of a thermal cleaning in the UHV system in Leoben by annealing them at 773 K for 15 minutes with a homemade electron bombardment heater (mentioned in chapter 3.1.1 and 3.2). According to the findings in chapter 4.1.2 for different treated SiO_2 surfaces and different ion-bombarded mica in [135], the question occurs what kind of effect a different heating treatment (in duration and temperature) of the SiO_2 surface canhave on the growth of 6P can have. Whereas etching with O_2 or bombardment with Ar^+-ions means an active modification of the surface, annealing via heating in UHV is more passive, giving a crystallographic structure the ability and time to relax the tensions inside the crystal by itself with the help of higher temperatures. Annealing is used very commonly in semiconductor production (chap. 13.5.2, p.479-481 in [137]). This leads to the hypothesis that this thermal relaxation should allow surfaces for restructuring and consequential for decreasing their roughness. Additionally, the heating of samples in UHV can reduce the surface contamination by impurities.

To investigate the changes which may occur on the surface, a series of SiO_2 samples was annealed at temperatures between 323 K and 1073 K, in a first step with the standard annealing time of 15 minutes and an additional bombardment with electrons which were accelerated at 1 kV towards the back side of the sample holder (see in chapter 3.1.1). In a second step, the annealing was done at different temperature for the same 15 minutes but with a much lower electron acceleration at 20 V. For the last step, a series of samples was annealed at 773 K with 1 kV for the electron acceleration for 10, 15, and 20 minutes. These three samples were then compared with samples which were either not annealed or annealed at 773 K without using electron bombardment at all. The growth parameters at room temperature (RT) were chosen suchlike that the average 6P coverage over all samples were similar.

Figure 4.6 shows 10x10 μm^2 representative AFM images of samples which were handled with different annealing temperatures grown like described above. While Figure 4.6(b) - (h) are representative for the standard annealing procedure at different temperatures, Figure 4.6(i) - (l) display the annealing at different temperatures with low accelerated electrons during the bombardment. Figure 4.6(a) was added to provide a comparison with a sample without any annealing before growing 6P onto it.

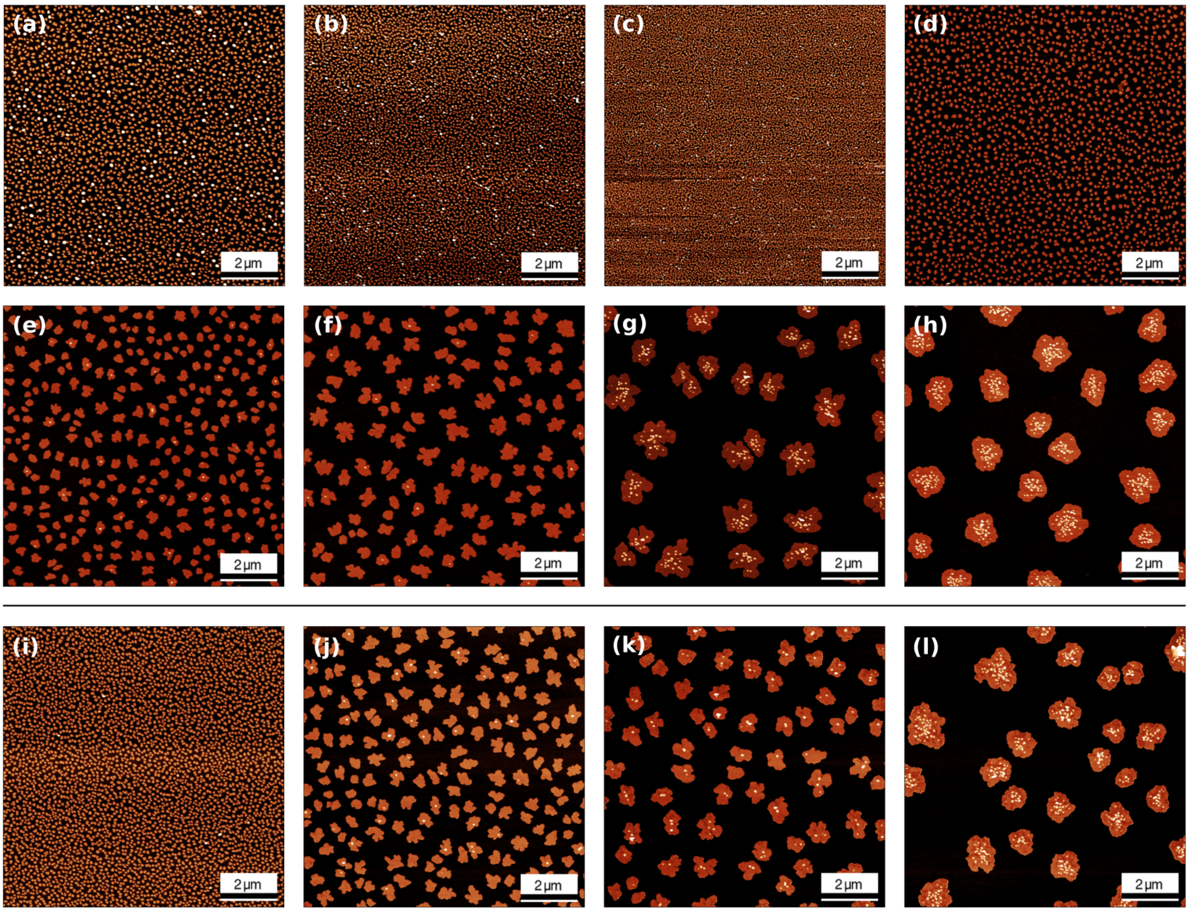

Figure 4.6: 10x10 μm^2 AFM images with a z-scale of 6 nm of samples grown at RT with a similar deposition rate $R = 0.035 \pm 0.006$ ML/min to reach the same coverage in average. (a) Sample grown without annealing procedure. The samples (b) to (h) were annealed with 1 kV electron bombardment before growth for 15 minutes at (b) 323 K, (c) 373 K, (d) 473 K, (e) 573 K, (f) 673 K, (g) 773 K, and (h) 1073 K. The lower row shows samples grown after an annealing with 20 V e$^-$-bombardment and for 15 minutes at (i) 473 K, (j) 573 K, (k) 673 K, and (l) 773 K.

The results of the island densities from all grown samples are summarized in the plot of Figure 4.7. The numbers next to the symbols in the plot represent the mean values of the island densities in islands per μm^2 obtained from AFM images at different positions on each specimen. The orange symbols are two samples which were only put into the plot at 300 K for comparison but didn't see any annealing procedure. The second sample has more than the double island density than the first sample. This due to the fact that the second sample was during the back-out in the load lock at about 360 K for more than 15 hours. Normally a bake-out of the load lock lasts half the time. Here, it is interesting to see, not the annealing but a longer bake-out shows the same result in island density than a standard annealing at 323 K.

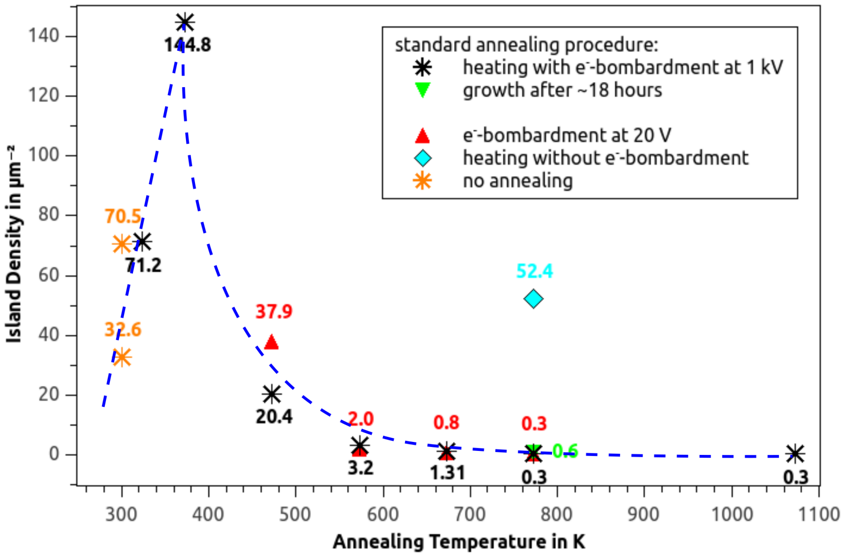

Figure 4.7: Graph with the island densities of SiO_2 samples which were annealed at different temperatures for 15 minutes. The first two values in orange at 300 K are plotted only for comparison, they were not annealed before growth of 6P. The samples in black are annealed at different temperatures with 1 kV electron bombardment. Triangular marks in red present the annealing at different temperature with 20 V electron bombardment. The sample with a green triangular mark was annealed with a standard procedure but stayed in the heater about 18 hours before growth. The sample marked in blue was annealed at 773 K without support by electron bombardment. The error bars covers approximately the size of the used symbols. The dashed dark blue line is a guide to the eye.

The trend in island densities of samples annealed with the standard procedure is illustrated by a dashed line in Figure 4.7. It reveals that there is a nearly linear and steeply increase until an annealing temperature of 373 K followed by an exponential decay for annealing temperatures higher than 373 K. The samples annealed in step two with 20 V electron bombardment seem to follow the same trend like the standard samples. At 473 K there is a similar island density like at the sample without annealing, only this sample has an obvious lesser second layer nucleation than the sample without annealing (compare their AFM images in Figure 4.6(a) and (i)). While the samples annealed at 573 K and 673 K show a lower island density than the standard samples, at 773 K the slight difference is only a result of statistics and has no meaning. They have the same amount of second layer nucleation, only that the islands seem to be less dendritic on the sample with 20V electron bombardment (compare the AFM image in Figure 4.6(l) with (g)). The three other samples reveal no difference in island shape comparing with their vis-a-vis of standard samples at the same temperature (Figure 4.6(d) and (i), Figure 4.6(e) and (j), Figure 4.6(f) and (k)). Two samples annealed with 773 K (indicated with light blue and green symbols in Figure 4.7) were handled specially. While the light blue marked one was only heated for 15 minutes without help of electron bombardment, the other sample stayed after the annealing process about 18 hours in the sample holder of the heater before the growth started. Generally, the SiO_2-substrate in this setup needs not more than 2 or 3 hours to reach RT in the phase of cooling down passively after the standard annealing procedure (shown in chapter 3.1.1 in Figure 1). In Figure 4.8 the surface morphology of these two samples is compared with two others annealed with electron bombardment at 1 kV and 20 V.

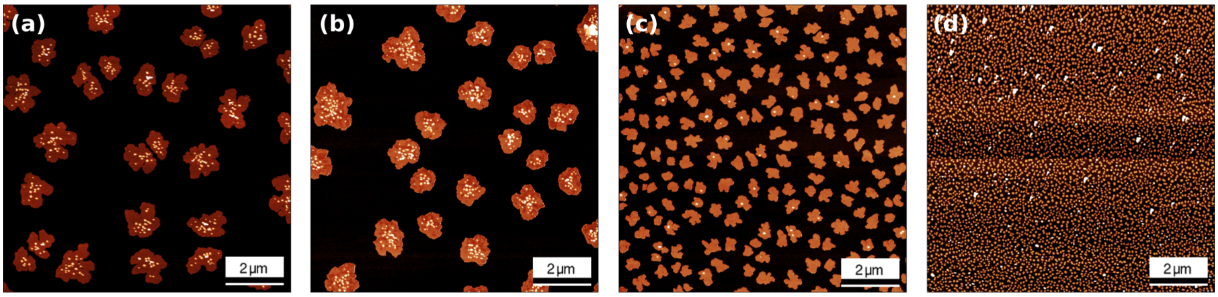

Figure 4.8: 10x10 μm^2 AFM images with a z-scale of 6 nm of four 6P submonolayer thinfilms on SiO_2 annealed at 773 K for 15 minutes and grown at RT. Samples presented in (a–c) were annealed with help of electron bombardment with (a) & (c) 1 kV and (b) 20 V, while (d) was heated without electron bombardment. (c) was not deposited immediately after cooling down, only after a stay in the heater of about 18 hours.

Comparing the four AFM images in Figure 4.8 with each other, there is nearly no difference in island density between the two first samples annealed with 1 kV and 20 V electron acceleration. However, as mentioned before, the islands are more compact after annealing with 20 V acceleration. The third image in Figure 4.8 of the sample which was not grown immediately after cooling down to RT shows a more than doubled island density (between ninety and even two hundred times higher according to the different positions on the sample investigated by AFM). And the fourth sample has much higher island density. The island shape on this sample is comparable with samples at 20 and more islands per μm^2 (look Figure 4.6(a)-(d) and (i)).

Like described in the beginning of this section, in a third step samples were prepared before growth with an annealing temperature of 773 K with 1 kV electron acceleration for different times: 10 and 20 minutes (and then compared with the standard annealing procedure for 15 minutes). In Figure 4.9, the mean values of island densities from AFM investigations are presented together with exemplary AFM images as insets. All samples show a dendritic growth behavior, and the island size is increasing with longer annealing time. While the differences in island density at 15 and 20 minutes are small, the island density for 10 minutes annealing time is 4 to 7 times higher.

In conclusion, these investigations show a noticeable influence of temperature and time during the heating before growth. It is evident that the cleaning and the annealing process starts to be effective beyond 373 K. Below 373 K, the restructuring of the surface seems to increase the roughness that more traps for the adsorbed 6P molecules appear and the desorption of surface impurities has not started working yet for them to become additional nucleation sites. Above 373 K, the trend in Figure 4.7 shows that the effect of annealing to obtain a smoother surface and the decreasing amount of impurities results in an exponential decay in island density until 673 K. Beyond this annealing temperature, the effect of smoother surfaces becomes less. Something similar can be interpreted from the investigations of different heating times. But it should be mentioned that with higher temperatures, the duration of cooling down becomes longer and this may result in a recontamination of the sample in UHV. This behavior is demonstrated the sample (green indicated in Figure 4.7) which remained in UHV for about 18 hours before the growth. Within this time, the effect of recontamination results in a doubled island density, while the decreased roughness of the surface by annealing is expected to remain unchanged after heating. It should also be mentioned that the samples needed a certain time to reach the chosen annealing temperature, then they were held for 15 minutes at this temperature, and finally the samples took a long time reaching RT for growth. So, the annealing and the desorption of impurities does not happen within these 15 minutes only, it begins already before in the phase of temperature ramping and lasts even longer

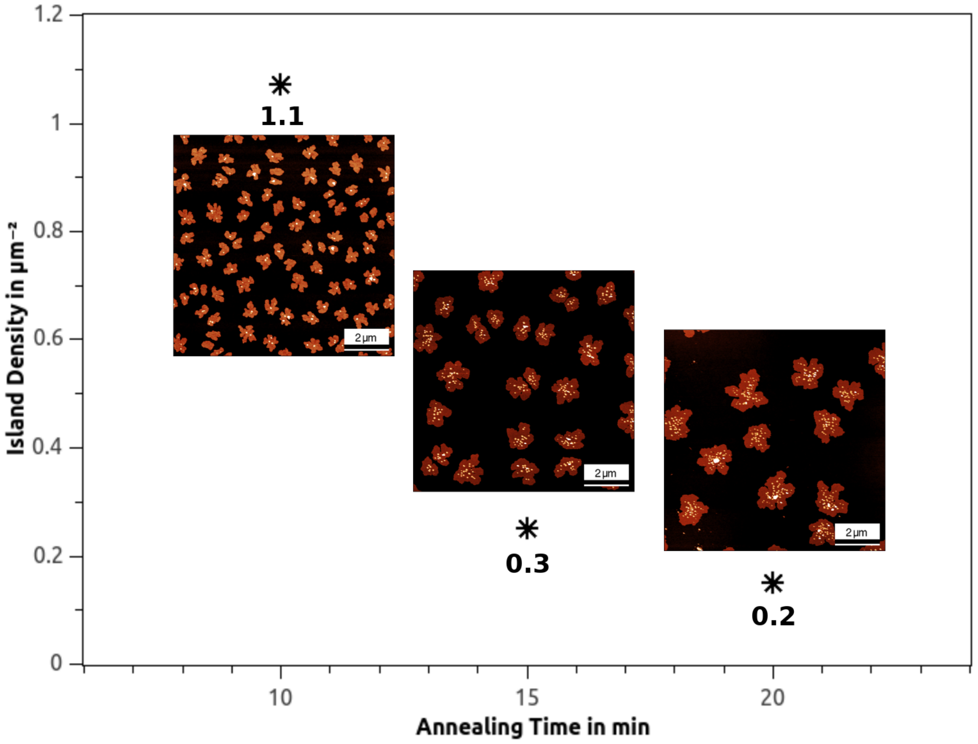

Figure 4.9: Graph with the island densities of SiO_2-samples which were annealed with different times at 773 K. The numbers below the symbols are mean values of the island density. The error bars cover approximately the size of the used symbols. Insets: exemplary 10x10 μm^2 AFM images with a z-scale of 6 nm for each annealing time.

into the phase of cooling. The effect of surface restructuring by annealing in general needs high temperatures and a longer time than the desorption of impurities. Therefore, the much higher island density for electron bombardment with 20 V compared with 1 kV at 473 K results not from a different annealing but from the amount of impurities. Higher electron acceleration of the bombardment means shorter time to reach the chosen annealing temperature. Therefore, reaching high temperatures during the heating phase in a shorter time reveals that the impurities desorb faster from the surface as in comparison to a longer heating-up time. This can even explain why the island density on the sample annealed at 773 K without the help of electron bombardment (light blue data point in Figure 4.7) is that high. The slow ramping up to reach 773 K should be enough time for the annealing but has a very small effect on the desorption of impurities. In the case of 573 K and 673 K, the samples with 20 V electron bombardment show smaller island densities than with 1 kV. This can be explained that reaching this temperatures needs longer, and this long time allows balancing both mechanisms – annealing and desorption.

4.1.4 Growth at different substrate temperatures

6P thin films were grown onto SiO_2 at different temperatures of the substrate ranging from 285 K to 453 K. For temperatures above room temperature (RT), the samples were held at a certain temperature by heating from the back side within the homemade heater but without using high voltage for electron acceleration. To reach temperatures below RT, the growth chamber was cooled passively from outside by liquid nitrogen as described in chapter 3.2. Owing to the lack of good thermal conductivity in vacuum, it was only possible to reach substrate temperatures around 280 K, but not below. All samples went through the same standard thermal cleaning procedure before growth. During growth, the deposition rates were approximately constant for each sample at 0.03 ML/min reaching similar coverage of (0.25 ± 0.05) ML.

Figure 4.10 shows AFM images of this temperature series. Two main points are conspicuous while surveying the images and comparing with each other. First of all, the islands seem to be more compact at low temperature and become more dendritic at higher temperatures. Secondly, the island area increases from an approximate radius of 0.3 μm at 285 K to 3 μm at 423 K and decreases for higher temperatures down to a minimum radius of 0.4 μm at 453 K. At a substrate temperature of 398 K, a change in the film morphology takes place. Now the islands tend to become less dendritic and slightly smaller. Their density decreases due to the fact that more small islands appear between the bigger ones. This behavior is called bimodal growth and will be referred to later.

As displayed in Figure 4.10(i), there are no islands visible at the highest applied substrate temperature. There are higher structures (white) observed which have a diameter between 0.8 and 2 μm with a maximum height in average up to 150 nm. There is no evidence of compact or dendritic islands of a first layer or with a second layer like shown in Figure 4.10(a) to (h).

Figure 4.11 presents an attempt to compare this investigation on SiO_2 with previous results of 6P on mica which were published by Potocar et al. in 2011 [27] and Tumbek

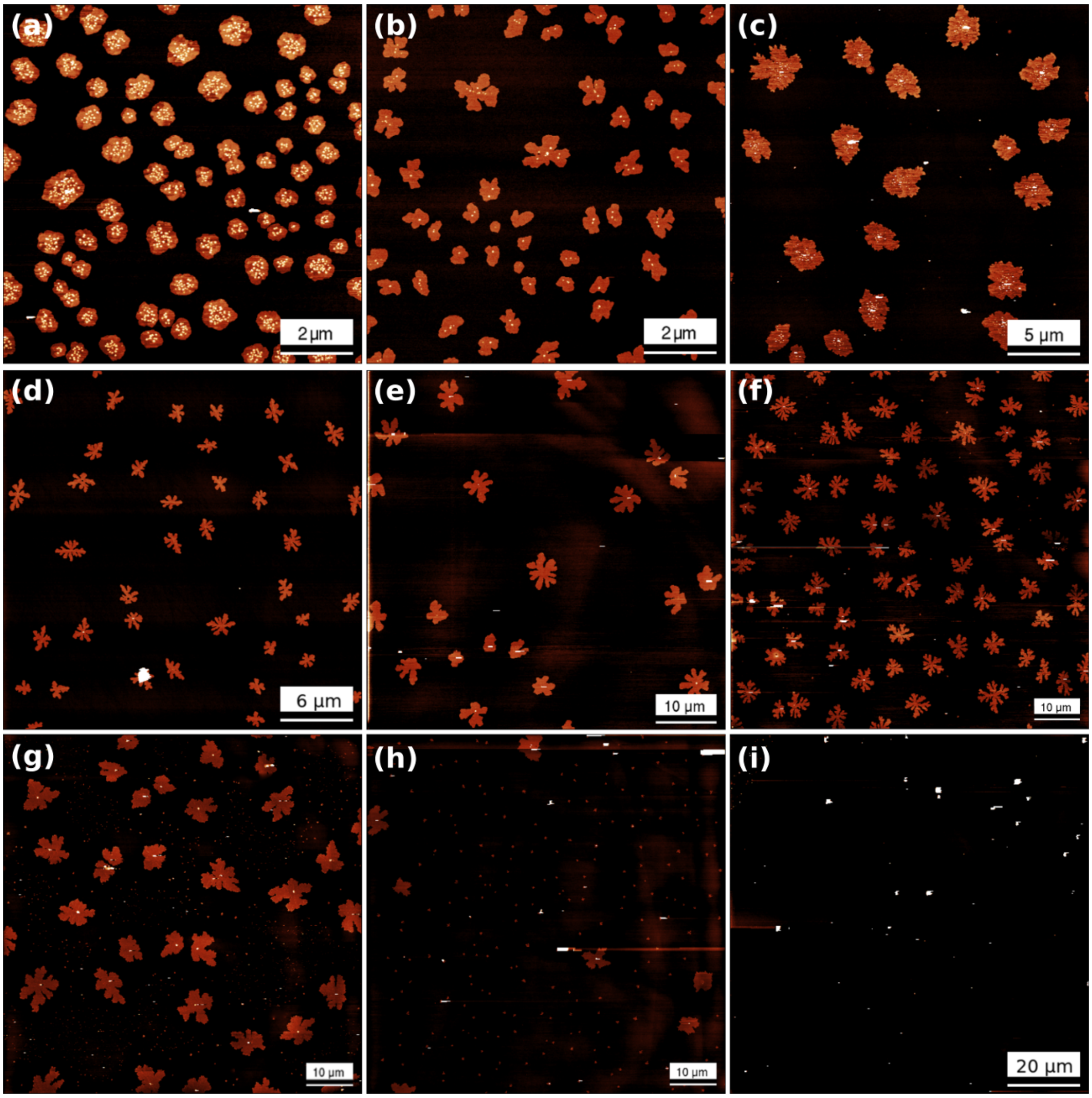
(a)
2 µm
(b)
2 µm
(c)
5 µm
(d)
6 µm
(e)
10 µm
(f)
10 µm
(g)
10 µm
(h)
10 µm
(i)
20 µm

Figure 4.10: Representative AFM images recorded from samples grown at different substrate temperatures as examples (with a z-scale of 6 nm). 10x10 μm^2 images of samples grown at (a) 285 K and (b) RT; (c) 25x25 μm^2 image of a sample grown at 343 K; (d) 30x30 μm^2 image of a sample grown at 348 K; (e) 60x60 μm^2 image of a sample grown at 373 K; 80x80 μm^2 images of samples grown at (f) 398 K, (g) 423 K and (h) 448 K; (i) 100x100 μm^2 image of a sample grown at 453 K.

and Winkler in 2012 [135]. The slope of a plot in such a ln(island density N) versus reciprocal substrate temperature ($1/T$) diagram is a function of the involved activation energies. In theory, the plot should yield a straight line if there is only one process involved. Even there was no possibility to reach the same low temperatures like for the growth on mica, the plot for the growth on SiO_2 in the $\ln N$ vs. $1/T$ diagram shows in a temperature range from 285 to 373 K the same nonlinear relationship. As mentioned before, a change in growth occurs at a temperature above 398 K, which is obvious in the graph in Figure 4.11 with the change of its slope to a negative value.

In many cases, a deviation from a linear relationship is observed [130, 138, 139]. The ideas to explain this behavior range from a proposed post-deposition nucleation and growth being responsible for the leveling-off at low temperature [138], a possible desorption at high temperature [139], to a change in the growth mechanism as a function of temperature [130]. Nevertheless, Winkler and his group suggest an other plausible explanation for this phenomenon with the idea that the 6P molecules are in a so-called hot-precursor state (which was introduced in 2014 by Morales-Cifuentes, Einstein, and Pimpinelli [140, 141]) when the molecules are impinging onto the surface during deposition [72, 142]. The molecules possess initially a kinetic energy according to the evaporator temperature (Knudsen cell temperature). This kinetic energy cannot be completely dissipated upon the impact on the surface. The equilibration of excited rotational and vibrational states of the 6P molecules leads to the effect that the molecules are confined to the surface but have still some transient mobility along the surface until they become fully accommodated as illustrated in the scheme in Figure 4.12 (taken from [72]). As a consequence to this ballistic-like motion in this hyper-thermal sojourn, while the molecules have an effective temperature higher than the surface temperature, the molecules can meet other diffusing molecules to form unstable or stable nuclei, or become incorporated into an existing cluster which can cause even breaking the clusters apart or detaching single molecules from them due to the high energy in the precursor state.

The model of a hot-precursor state for the impinging molecules can be even used to explain the behavior of the film growth at higher substrate temperatures. If the substrate temperature is higher than 373 K it seems that the molecules stay longer in this precursor state. Thus, they are able to move faster and over longer distances on the surface. And the probability of building unstable nuclei or destroying already stable islands becomes higher at higher temperature. The evidence of the very high structures (up to 150 nm)

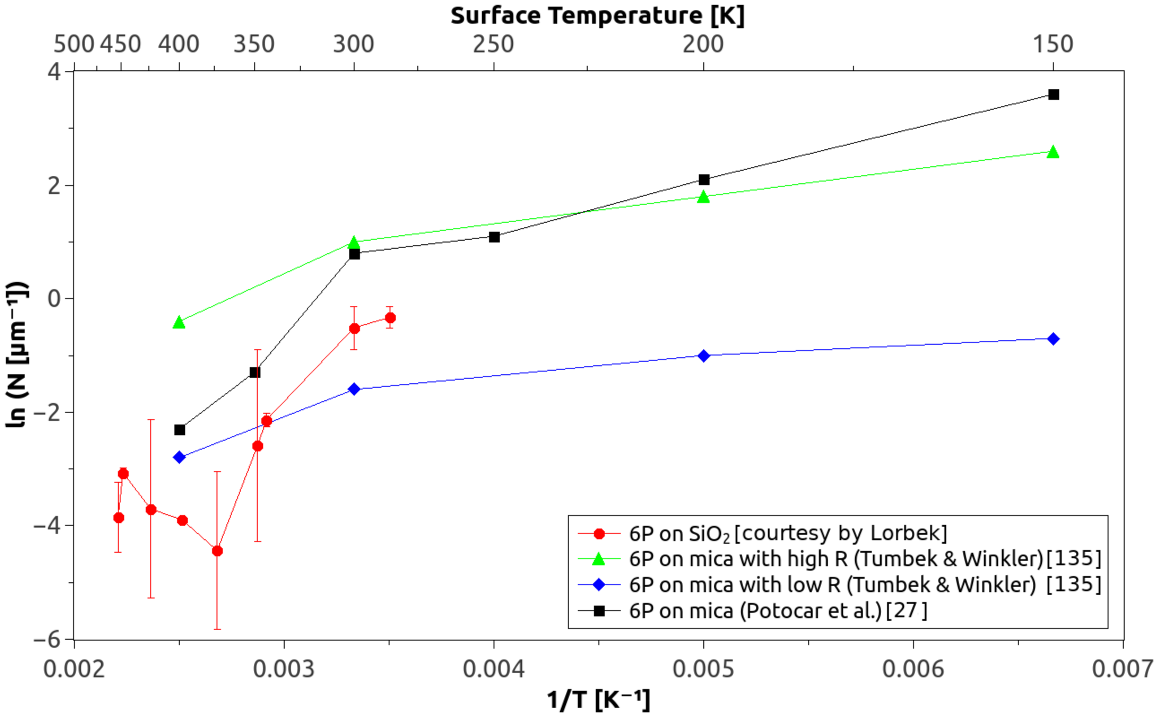

Figure 4.11: Substrate temperature dependence of the island densities for various film/substrate 6P systems, taken from [27] and [135] supplemented with the results of 6P on SiO_2 (error bars present the standard deviation).

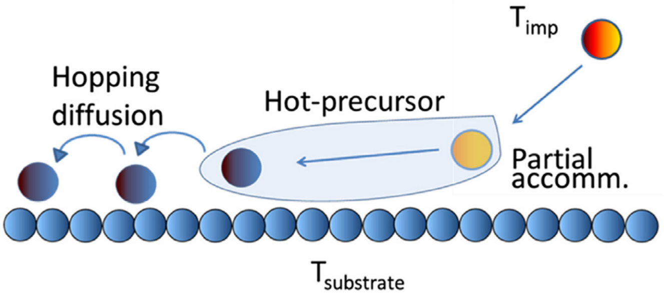
T_{imp}
Hopping diffusion
Hot-precursor
Partial accomm.
$T_{substrate}$

Figure 4.12: Scheme of the hyper-thermal diffusion of an impinging molecule during deposition up to the final thermal accommodation. (From [72].)

with small diameters (down to 0.8 μm at high temperatures (453 K) can be explained that it is easier for the molecules with higher kinetic energy to overcome energy barrier at the terrace's edge which is slightly higher than the Ehrlich-Schwoebel-barrier for upward jumps instead of a perseverative edge diffusion until the molecules can incorporate into an existing island.

4.1.5 Growth with different deposition rates

The main attention of this work was not laid on investigating thin-film growth at different deposition rates R. The interest was mainly focused on a rate-independent finding of the critical nucleus i^* using CZD of Pimpinelli and Einstein comparing with ISD of Amar and Family (see chapter 4.1.1). Nevertheless, a few experiments with 6P were performed on SiO_2 at different deposition rates by varying the evaporation temperature of the Knudsen-cell in the growth chamber. The standard evaporation temperature was 523 K. Within this growth series, the cell temperature started at 503 K and was increased until 523 K. The topographic images of these samples are displayed in Figure 4.13(a) to (c). In all cases, the substrate temperature during growth was held at RT. With increasing Knudsen-cell temperature, the deposition time was decreased to get an average coverage θ similar for all samples of about 0.14 ML. Figure 4.13(d) and (e) are presenting the behavior of the island area size and the island density versus deposition rate.

Figure 4.13(d) already reveals what the AFM images in (a) to (c) display that with higher deposition rate, which is proportional to the Knudsen-cell temperature, the island size decreases while the island density increases. This can be explained by the fact that the kinetic energy of the impinging molecules is related to their temperature during evaporation. Higher energy means higher probability of detaching from islands and even hitting more often other diffusing molecules to generate more nucleation sites. Although, a higher R results in a higher chance for the molecules to meet each other at the substrate. With plotting $\ln N$ vs. $\ln R$ in Figure 4.13(e) and adding a linear fit and connecting the result of its slope with RE of Venables et al. like mentioned in chapter 2.1.2 the scaling exponent χ is easy to obtain. Here, χ has a value of 1.3 ± 0.3 which results in a critical nucleus size i^* of -8 in case of DLA or 6 for ALA. Both results are in contradiction to the result obtained from CZD and ISD which lies between 1 and 2. The findings in chapter 4.1.2 revealed that at RT the growth is mainly diffusion-limited driven, and not like the result from RE shows here. However, there are more than three data points needed to obtain a reliable result. Therefore, performing more experiments is recommended.

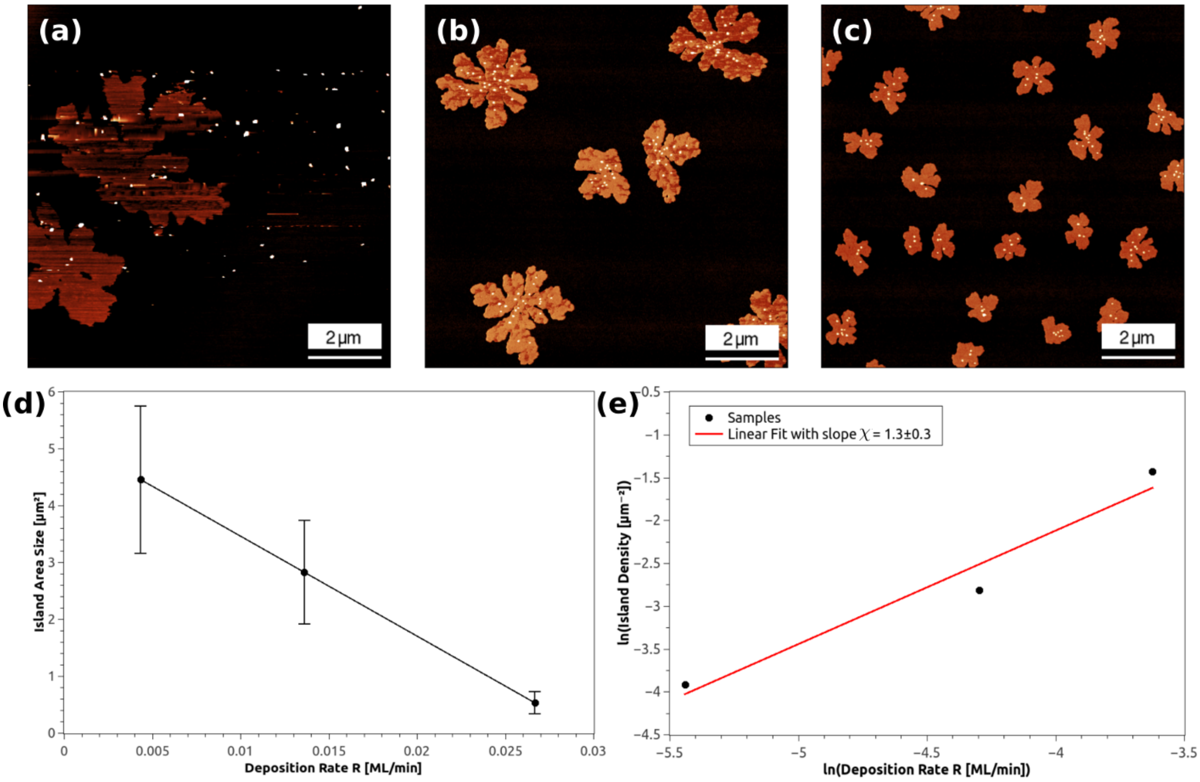

Figure 4.13: Upper row: 10x10 μm^2 AFM images of the film topography of samples grown at RT with different evaporation temperatures of the Knudsen-cell, (a) 503 K, (b) 513 K and (c) 523 K (each z-scale is 6 nm). (d) Plot of the island area size vs. deposition rate R (error bars present the standard deviation). (e) Plot of the ln(island density) vs. $\ln R$ added by a red line which is the linear fit through the sample data points with a slope of 1.3±0.3.

Tumbek and Winkler found for 6P on mica that there are two different slopes for lower and for higher depositions rates [135]. Their result of χ for higher R is 1.4 ± 0.1 which is comparable with the χ of this work. Nevertheless, the deposition rates here are more similar to the low deposition rates of Tumbek and Winkler but resulting there in a χ which is only the half of the value at higher R. This is one more proof that the growth morphology on SiO_2 is similar to the growth on mica but with differences in activation energies which result in different i^* for the two different substrate materials.

4.1.6 Bimodal island-size distribution in thin-film growth

Already Potocar et al. [27] found the evidence of a bimodal island-size distribution on samples of 6P on amorphous mica at a substrate temperature of 400 K. Small islands with an average diameter of 0.1 μm appeared between the expected islands of average size which had an average diameter of 1.2 μm (compare Fig.8(d) in [27]). Tumbek et al. [143] performed a detailed investigation of this effect with growing 6P on the same kind of amorphous mica at the same temperature and a deposition rate of about 0.1 ML/min but with different coverages. Using thermal desorption spectroscopy (TDS) they were able to prove that during deposition a wetting layer of mostly lying 6P molecules must arise. The molecules from this wetting layer begin only to nucleate islands of upright standing molecules after venting the UHV system. They explained this post-nucleation with a dewetting by virtue of the exposure to air, most probably because of water co-adsorption. Based on islands which are in equilibrium with the 2D gas phase during deposition, the exposure to air can induce a subsequent nucleation in a particular coverage regime afterwards. Their model was even proved with kMC simulations of this adsorbate-induced subsequent nucleation process [143].

During this work of 6P thin-film growth on amorphous SiO_2, a bimodal island-size distribution was found too. Samples were grown not only with different coverages, but even at different substrate temperatures (348 K, 373 K, and 423 K). The investigation of these samples by AFM under ambient conditions is presented in Figure 4.14.

First of all this investigation shows what Tumbek et al. have already found that until 373 K a bimodal island-size distribution occurs for higher coverages around 0.12 ML while for a coverage of around 0.05 ML the number of small islands is negligible (compare the images (a) to (d) with each other column by column in Figure 4.14). If the substrate temperature is chosen higher than 373 K, Figure 4.14(e) and (f) show that in both cases of low and high coverage, a bimodal island-size distribution appears. Only at low coverage, the number of small islands decreases but they increase in size comparing with samples at higher coverage. The size of big islands is comparatively stable in both cases, but their number is much higher in the case of higher coverage. At the images with a bimodal island-size distribution in Figure 4.14, a denuded zone around the larger islands is clearly visible like reported by Tumbek et al. who explained this as a consequence of the decreased monomer density in the immediate vicinity of the stable islands

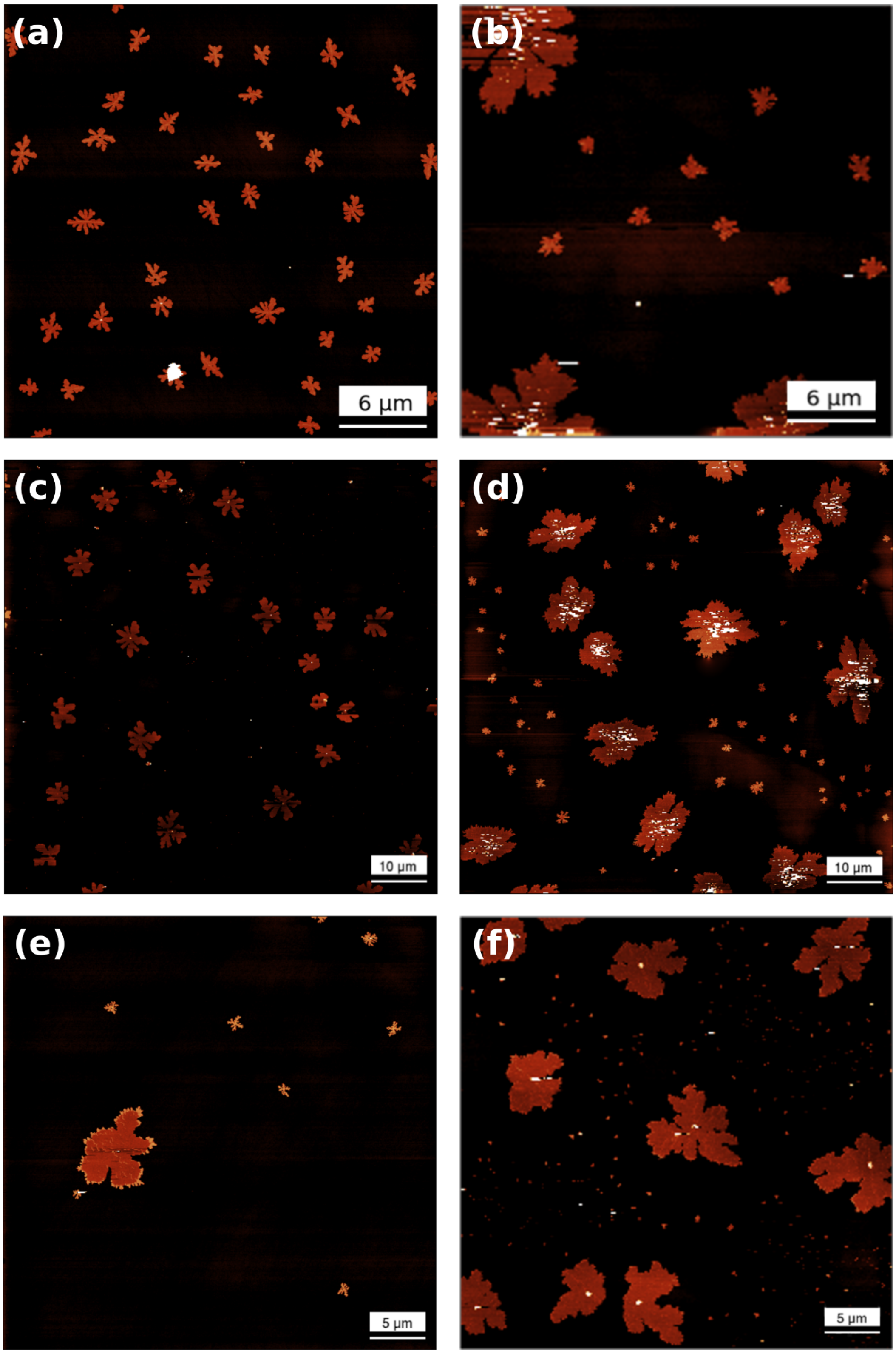

Figure 4.14: AFM images with a z-scale of 6 nm of six different samples grown at three different substrate temperatures with an average coverage of 0.05 ML (left column) and 0.12 ML (right column). (a) and (b) are 30x30 μm^2 images grown at 348 K. (c) and (d) are 80x80 μm^2 images grown at 373 K. (e) and (f) are 40x40 μm^2 images grown at 423 K.

in agreement with the diffusion-limited aggregation model [144].

Figure 4.15 displays the densities of large and small islands dedicated to substrate temperatures used during growth. For a coverage between 0.09 and 0.14 ML, the graph indicates the same, what the AFM images in Figure 4.14 already showed, that at temperatures higher than 373 K the small islands become dominant.

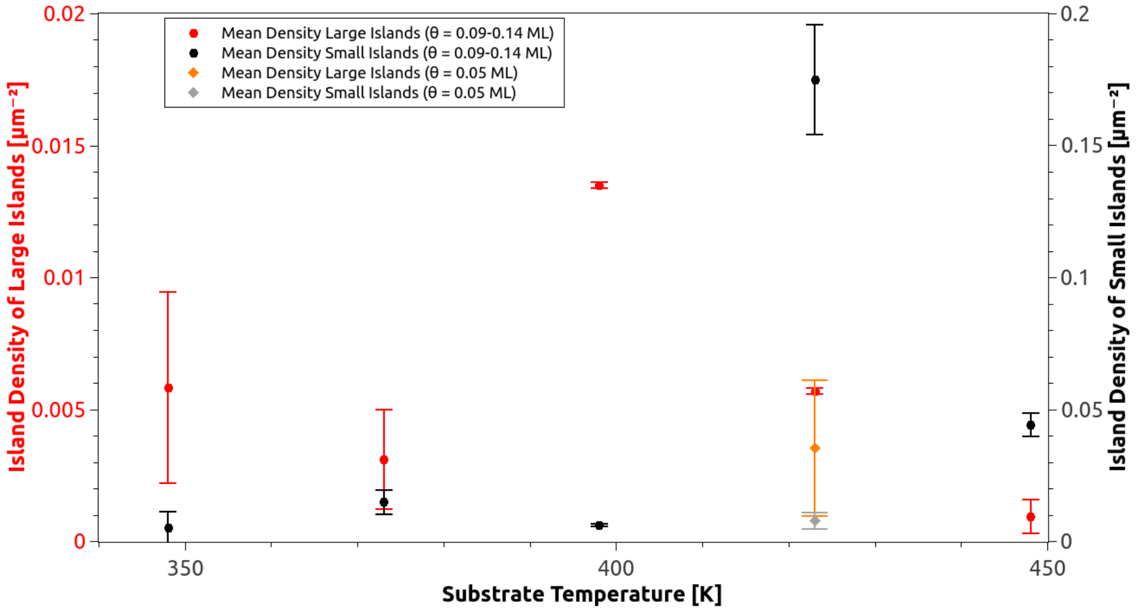

Figure 4.15: Island densities vs. substrate temperatures. Black marks represent the density of small islands and red marks represent the density of large islands for a coverage between 0.09 and 0.14 ML. At 432 K, the orange and gray marks stand for a coverage of 0.05 ML which are added for comparison. Error bars present the standard deviation of measured data.

The added data for a sample with bimodal island-size distribution with a coverage of 0.05 ML reveals that there is no coverage dependence on the occurrence of bimodal island-size distribution at higher temperatures, but the island density of small islands is significantly lower than at higher coverage. This can be explained by the lower amount of lying molecules in the wetting layer which is formed during deposition. More material in the wetting layer results in a higher amount of post-nucleated islands, but then they are much smaller in size.

From the data of samples grown with different coverage the graph in Figure 4.16 was plotted like the one produced before the investigations of 6P on amorphous mica (compare Figure 7 of [143]). To have a better view for comparison the same colors and symbols were chosen as in [143].

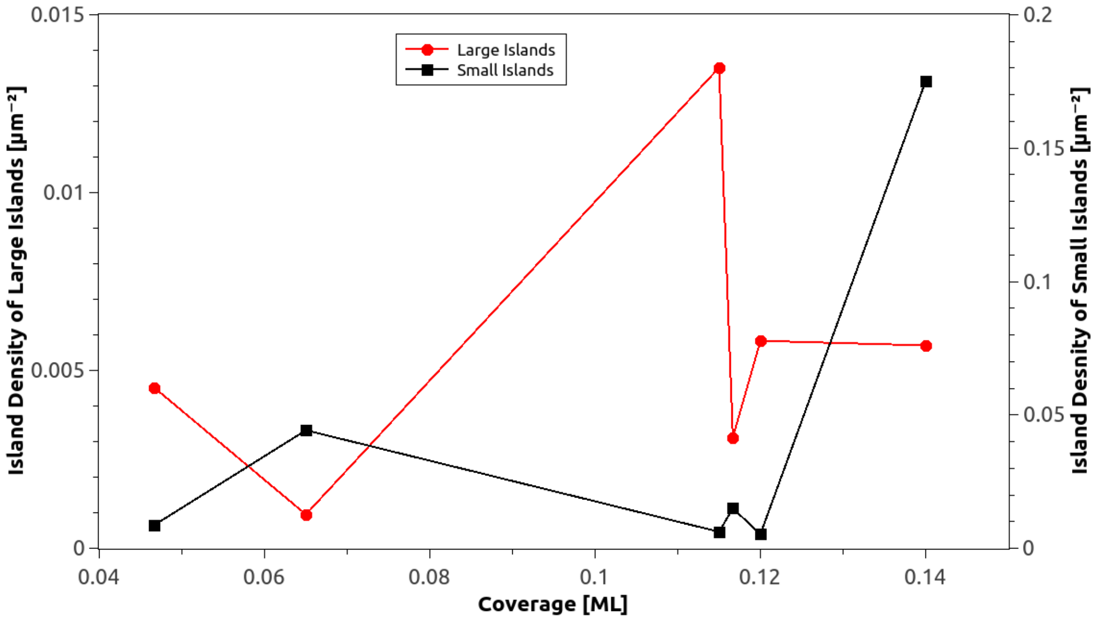

Figure 4.16: Coverage dependence of small and large island density for 6P on SiO_2. The lines are guides to the eye.

Whereas for 6P on ion-bombarded mica [143], a decrease in island density of small islands above a coverage of 0.03 ML for 6P is observed, for 6P on SiO_2 this decrease is taking place above a coverage of 0.65 ML. The same can be observed for the behavior of large islands for both substrate materials, where their density increases with higher coverage. While the density of large islands in case of mica is growing continuously, the density of large islands on SiO_2 seems to drop suddenly by more than half. Figure 4.16 shows that the sample at a coverage of 0.14 ML has a completely different morphology than the other samples with a sudden jump in the density of small islands. For this sample, the attempt of an explanation with a diffusion-limited aggregation model of Tumbek et al. [143] fails. For better understanding of this effect, further growth experiments and simulations would be needed. Because of the lack of a TDS in the UHV system in Leoben the proof of this suggested model by [143] for 6P on SiO_2 is furnished with difficulties. The only possibility would be the use of the Omicron AFM inside of the UHV system. Due to the limited scan size of 6x6 μm^2, th problem is to find a proper spot on the sample where the zone between large islands can be imaged. The images in

Figure 4.14 reveal that large islands can be bigger than 5x5 μm^2 and than it is difficult to distinguish between 1st layer of an island and the substrate surface or a first and a second layer. After many attempts, one AFM image could be recorded where a small part of the first and second layer of an island is visible and the rest of the image can be identified as the substrate surface. It is presented in Figure 4.17(a). This sample was grown at 373 K and has a coverage of approximate 0.4 ML, which is far more than all samples before. Here on SiO_2, still no coalescence is showing up like in Figure 6(b) in [143]. But in comparison on SiO_2 the large islands are positioned far from each other so that there is enough place for a post-nucleation after exposure to air (see Figure 4.17(b)).

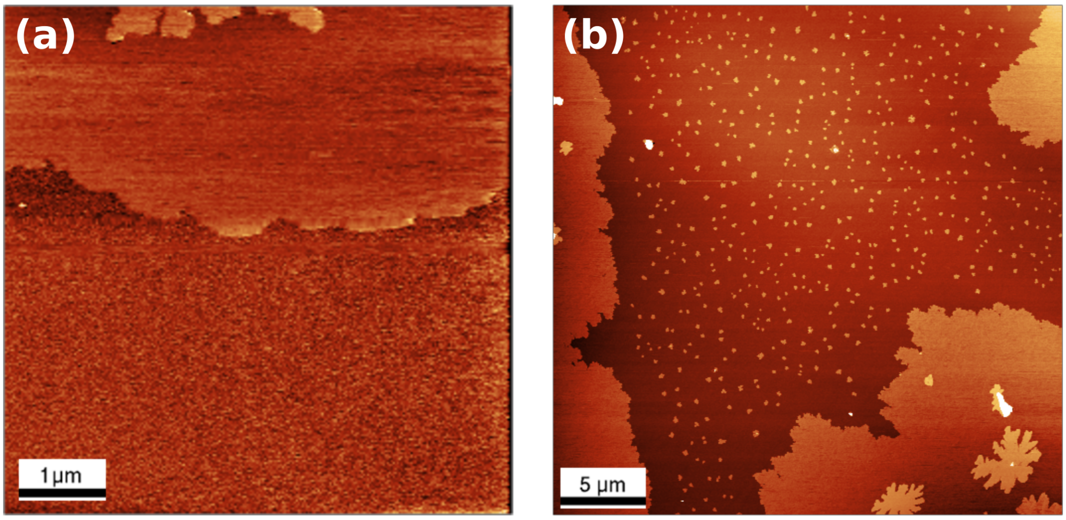

Figure 4.17: In-situ and ex-situ AFM images 0.4 ML 6P on SiO_2 grown at 373 K. (a) 6x6 μm^2 image by Omicron AFM in UHV with a z-scale of 5 nm. (b) 30x30 μm^2 image of the same sample by ex-situ AFM under ambient conditions (z-scale 12 nm).

While Figure 4.17(b) shows a large number of small islands between the large islands with a denuded zone size of about 1-2 μm, there is no indication of small islands in the 3 μm vicinity of the large island in Figure 4.17(a). This is in agreement with the TDS results in case of 6P deposition on amorphous mica [143], indicating that the same mechanism must take place when the SiO_2 samples are exposed to air. In this case, a wetting layer even surrounds stable islands during deposition. But these molecules cannot erect and be incorporated into already stable islands. During the procedure of taking samples out from the UHV system the load lock is vented slowly with nitrogen. Exact in the moment of opening the load lock, the water vapor in air which floods the load lock can induce a post-nucleation by co-adsorption.

4.2 Investigations of 6P on SiO_2 when performing a short annealing after film growth

In this section, morphological changes upon annealing of thin 6P films are investigated. Annealing is a common method in semiconductor industries to smooth surfaces or interfaces, to release stress in crystalline material, or to support diffusion of atoms or molecules into the bulk material. Here, the question occurs what may happen to a thin film of 6P on SiO_2 during an annealing step right after the deposition.

For this case, a series of samples with a mean coverage of 0.04 ML was grown at a substrate temperature of 373 K and a deposition rate of 0.02 ML/min, after the substrates experienced the standard thermal cleaning procedure. Exactly at the end of deposition, when the shutter of the Knudsen-cell was closed, the substrate heater was set to higher temperatures reaching fast substrate temperatures between 383 K and 423 K. Then the sample was held for 5 to 10 minutes at these temperatures. The AFM images in Figure 4.18 taken under ambient conditions show the topography together with the corresponding phase images of four samples which represent this series after the annealing.

As one can see, with higher annealing temperature or longer annealing time the islands of the submonolayer are shrinking by size (compare Figure 4.18(a) and (c)) until they begin to vanish completely at some sites (like shown in Figure 4.18(g)). At other sites, 6P molecules begin to pile up to needle-like structures from some tenth up to a few hundreds of nanometer height. Investigations of islands on samples annealed at lower temperatures than 403 K show no influence of the annealing procedure at all. Therefore they are not depicted here. During recording topographic images in tapping mode, mostly phase mode images are acquired simultaneously. Surprisingly, the phase images display the original size of the islands in their maximum extension at the end of the deposition while the topographic images show only the remnants of the islands after the annealing step. Figure 4.18(h) shows in comparison with Figure 4.18(g) even the “footprints” of islands whereas in the topography images these islands disappeared completely. These footprints – which are even found surrounding the diminished islands in Figure 4.18(b)

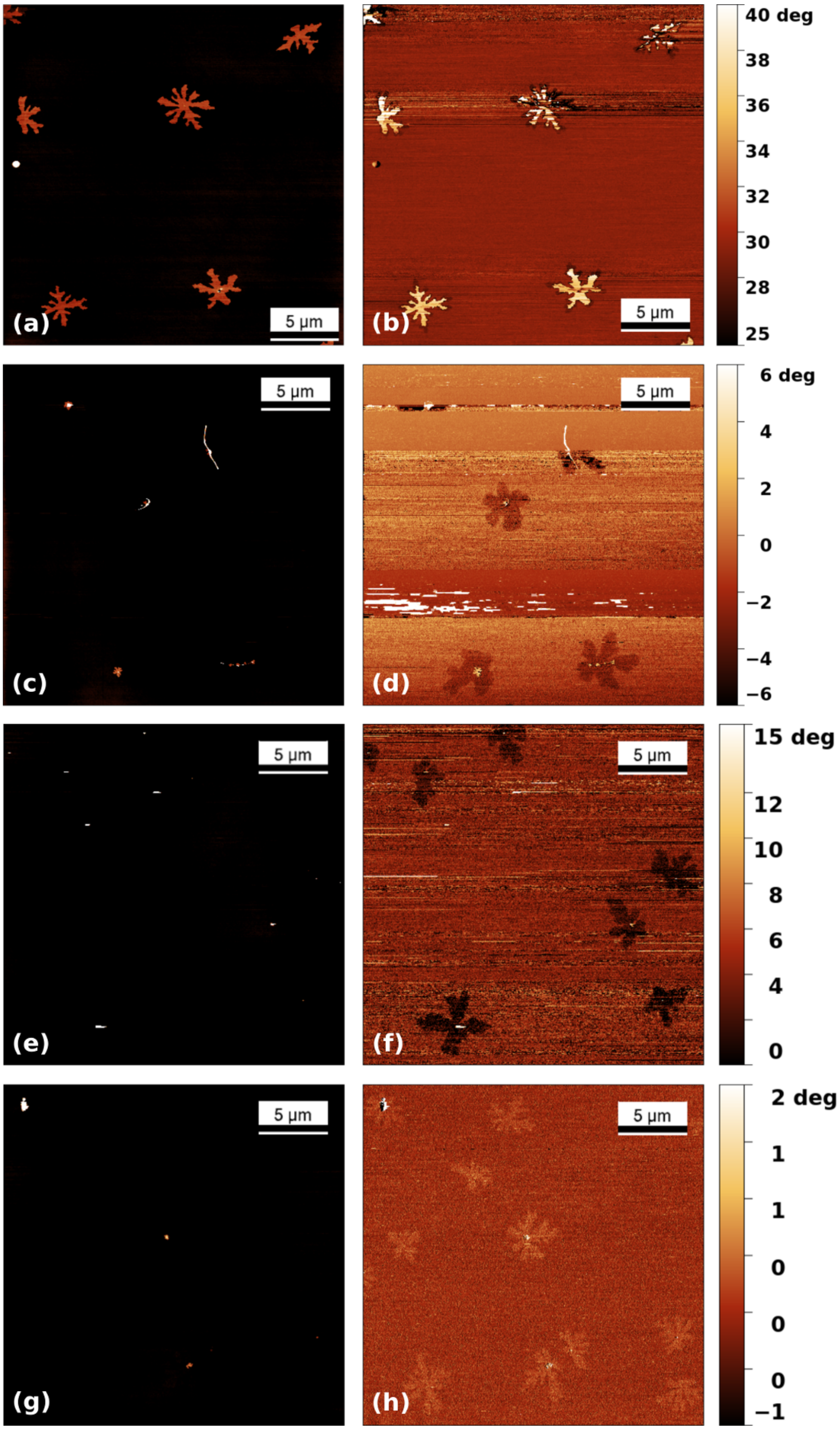
(a)
5 µm
(b)
5 µm
40 deg
38
36
34
32
30
28
25
(c)
5 µm
(d)
5 µm
6 deg
4
2
0
−2
−4
−6
(e)
5 µm
(f)
5 µm
15 deg
12
10
8
6
4
0
(g)
5 µm
(h)
5 µm
2 deg
1
1
0
0
0
−1

Figure 4.18: Left column displays the topographic images (25x25 μm^2 images with a z-scale of 6 nm) and right column the corresponding phase images (their z-scale is indicated by the false color rulers). Annealing procedure: (a) & (b) 403 K for 5 min, (c) & (d) 403 K for 10 min, (e) & (f) 413 K for 5 min, and (g) & (h) 423 K for 5 min.

as 250-500 nm wide dark rims – have another contrast than the surface or the islands' residuals. In general the "softer" islands consisting of upright standing 6P molecules appear in a lighter contrast than the "stiffer" surface in the phase images. Interestingly, the islands' footprints are represented by a darker contrast in Figure 4.18(b), (d), and (f), but by a brighter contrast in Figure 4.18(h) compare to the surface. One reason could be a difference in the viscoelastic properties for the surface and the islands.

A closer look on one island yields a detailed view on this shrinking process during the annealing which is presented in Figure 4.19 which is obtained from the sample as in Figure 4.18(c). Figure 4.19(b) reveals the same information on the viscoelastic properties from the phase image like discussed before. But in this case of a single island, the topographic image was masked by the footprint from the phase image and then two height profiles cover a similar distance from surface to surface over the islands' residual and its footprint. Both profiles are displayed by different colors (Figure 4.19(d)): the blue profile in Figure 4.19(e) is going directly through the center of the island and the red line in Figure 4.19(f) gives the profile which is slightly off-center parallel to the blue one.

The blue profile in Figure 4.19(e) shows the height of the island which is about one molecule length (2.6 nm) and indicates that it still consists of almost upright standing 6P molecules. The needle-like structure in the island's center is about 37 nm. To have a better view of the height at the footprints, the second profile in red is presented in Figure 4.19(f). While all phase images in Figure 4.18 and Figure 4.19 reveal a noticeable shift in the phase of the cantilever's oscillating frequency at the footprints, both depicted profiles doesn't show any evidence of a different in height of the surface caused by residuals of the island.

Like shown in Figure 4.19(c), Honjo et al. had recorded pictures every 20 seconds during the growth of a NH_4Cl crystal in a two-dimensional cell and arranged them overlapping each other which show the DLA-like growth, step by step [145]. They demonstrated that only splitted branches can grow outward and the other interface cannot grow much which was already predicted by simulations of Witten and Sanders in 1983 [37]. This represents a screening effect characteristic in the diffusion field. In comparison with this DLA-like growth, the observed shrinking of the 6P islands caused by annealing looks similar. Moreover, the rest of the island together with the footprint can provide an in-

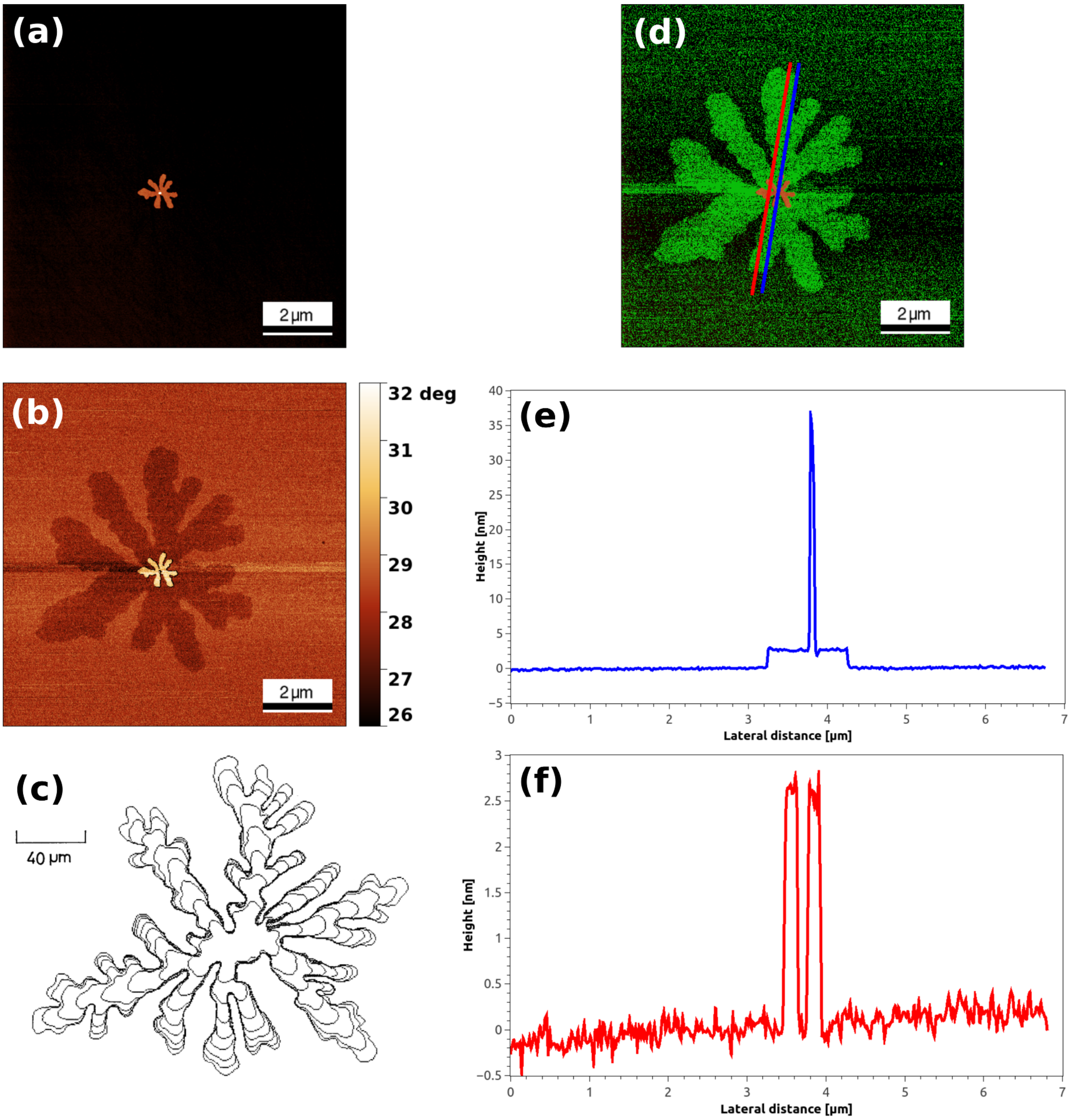

Figure 4.19: (a) 10x10 μm^2 topographic AFM image with a z-scale of 6 nm displays the residual of a single island from the sample annealed at 403 K for 10 min. (b) phase mode image of (a) with the same size. (c) overlapped pictures of DLA-like NH_4Cl crystal growing in two-dimensional cell with randomly roughened surface from [145]. (d) 10x10 μm^2 topographic AFM image from (a) masked by the footprint of (b). Two height profiles are marked in (d) by a blue and a red line which are presented in (e) and (f).

sight how an island of upright standing 6P molecules undergoes its growth to reach the observed dendritic shapes. To quantify this observation, the fractal dimension D_f was analyzed. Taking the original extension of the islands before annealing, D_f is in average about 1.85 ± 0.05 calculated from the footprints. After annealing at 403 K for 5 minutes D_f is decreasing a little bit to 1.75 ± 0.05. These values agree well with the model of two-dimensional DLA. If the annealing temperature is higher or the annealing time is prolonged up to 10 minutes, the average value of D_f drops down to 0.95 ± 0.05 for the residuals of the islands.

Further, the two-pass AFM technique Kelvin probe force microscopy (KPFM) was used to obtain the contact potential difference (CPD) which may yield information on these footprints. The result is exemplarily presented in Figure 4.20. The footprints are not visible in the topographic image in Figure 4.20(a) but show definitely up in the phase image of Figure 4.20(b) like expected. Furthermore, they can be tracked in KPFM images exhibiting different CPD compared to the surface and the residual of islands (displayed in Figure 4.20(c)).

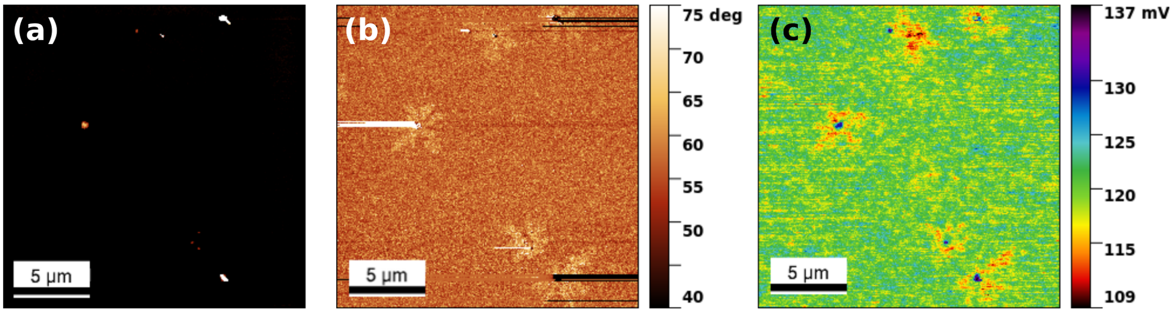

Figure 4.20: (a) 20x20 μm^2 topographic AFM image with a z-scale of 6 nm of a sample annealed at 423 K for 5 min. The corresponding phase image is displayed in (b) and the CPD map of the area in (c) (both z-scales are indicated by false color rulers).

Conspicuously, most KPFM investigations reveal that the islands' remnants have the highest CPD (for example in Figure 4.20(c) it is around 135 mV) and the footprints' CPD value is even below the one shown for the surrounding surface (in Figure 4.20(c) it is between 120 and 125 mV for the surface and around 112 mV for the footprints). This coincides with results from phase image investigations.

Additionally, contact mode AFM techniques like friction force microscopy (FFM) and transverse shear microscopy (TSM) were applied to this samples to uncover maybe something overseen in phase images or CPD maps. Figure 4.21 illustrates the results from (b) FFM and (c) TSM images with the corresponding topographic image in (a). The added graph of the height distribution in Figure 4.21(d) underlines that all investigated islands are consisting of upright standing 6P molecules (already proved in [4]).

While the FFM investigation show only a glimpse of footprints surrounding the islands' branches, the TSM image reveals nothing new about these footprints. However, the different colors of the remaining islands in the TSM image give a hint about the crystalline orientation of the 6P molecules within the bulk of the islands. Same color means same orientation. Therefore some islands have the same molecular orientation in Figure 4.21(c) whereas in other islands the 6P molecules seem to be tilted in a different direction towards the surface's normal [4, 110].

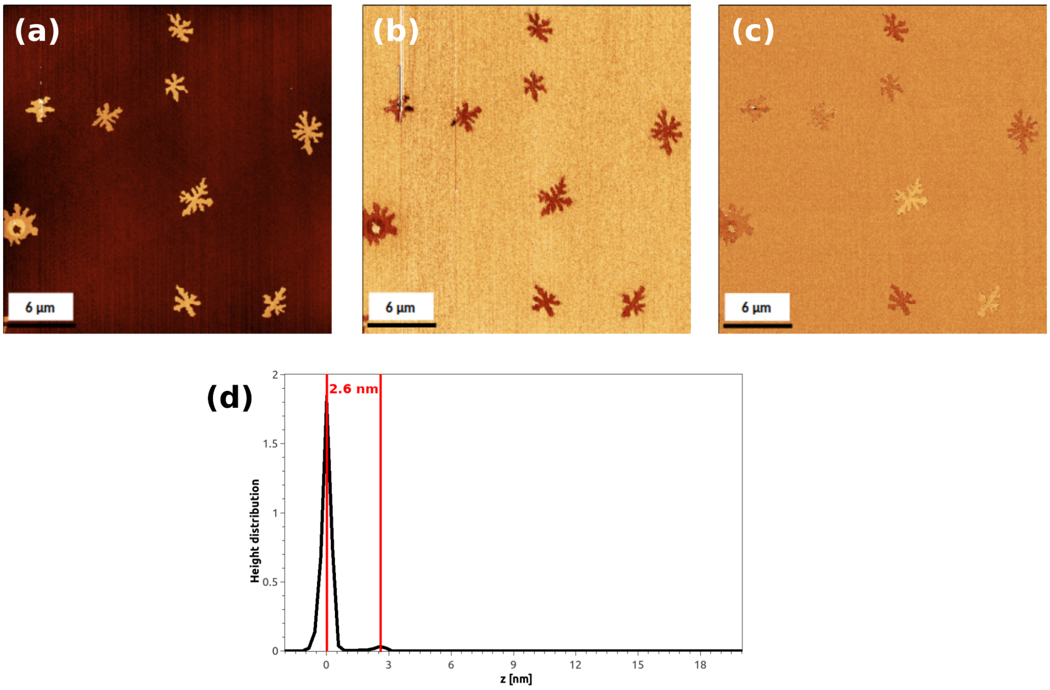

Figure 4.21: (a) 30x30 μm^2 AFM image of the topography with a z-scale of 6 nm taken from the sample annealed at 403 K for 5 min. (b) FFM image with a z-scale of 0.1 V and (c) TSM image with a z-scale of 18 mV of the topographic area shown in (a). (d) The height distribution over all islands of this sample. (All FFM and TSM images are courtesy by Q. Shen)

In conclusion, the investigations of samples which experienced a short annealing procedure right after the deposition result in islands' footprints of their former extension. These footprints are well shown in phase and KPFM images, but not in topographic and TSM images. The evidence of such footprints in FFM images is almost not visible. Nevertheless, even already dissolved islands show up in phase images at their former positions. The number of very high needle-like structures in the islands' center become dominant with higher annealing temperature which can be interpreted that with higher temperature the diffusion energy of the molecules increases high enough not only to desorb from the island edge but even to overcome easily the Ehrlich-Schwoebel barrier which causes piling up of these high structures. While the phase images display a change in the viscoelastic properties at the footprints, they appear in CPD maps of the KPFM images with completely other values than the islands or the SiO_2 surface. This may indicate not only a physical but even a chemical change of the area which was covered by the upright standing 6P molecules before annealing. In this case, further investigations are necessary. Comparing with DLA-like growth, the dissolving process of the islands during annealing indicates that in both cases – growing and dissolving – the same mechanism takes place. The islands' branches reduce more in length than in width which can be interpreted like a screening effect characteristic in the diffusion field due to DLA-like crystal growth by Honjo et al [145, 146].

4.3 Investigations of 6P deposition at grazing incidence on amorphous SiO_2

Like presented in chapter 2.1.4, steering effects were reported in growth of metal on metal surfaces which appear during deposition under a grazing incidence of an angle $\alpha > 50°$ (found by Dijken in 2000 [55]). This kind of growth results in a change in the surface topography. These findings were the motivation to start investigations on organic thin film growth under similar deposition angles. Therefore, a first series of different coverage was grown with $\alpha = 65°$. The annealing procedure for all samples within these investigations was the described standard one before growth. The growth itself took place at room temperature in UHV. Figure 4.22(a) is a sketch of the experimental setup with a view from above into the growth chamber. The heater with the sample in the holder is freely rotational around one axis. The broad green arrow symbolizes the organic molecular beam direction towards the sample which is tilted from the normal-incidence position by the deposition angle α. The analysis of a first try of the growth at grazing incidence of $\alpha = 65°$ is shown in Figure 4.22(b).

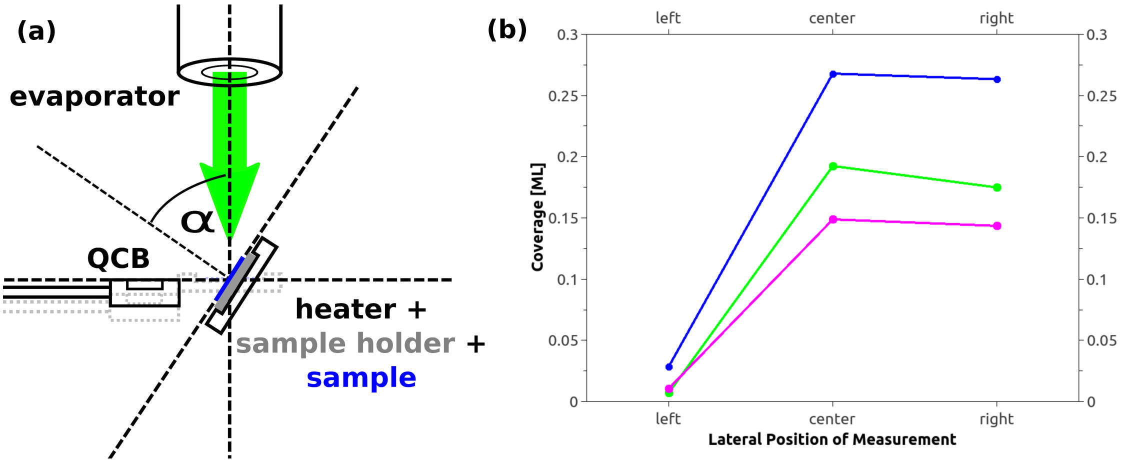

Figure 4.22: (a) Sketch of the experiment for growth at grazing incidence: α is the tilt angle of the heater (black) with the sample holder (grey) plus sample (blue); the horizontal dashed black line marks the normal position of the heater (grey dashed lines symbolize the positions of the heater and the quartz crystal balance (QCB)); broad green arrow indicates the molecular beam direction. (b) Graph of the analysis of a first series of the growth at grazing incidence of $\alpha = 65°$ showing the coverage of three samples measured at three different sample positions.

For the graph in Figure 4.22(b), different AFM topographic images were recorded at three sample positions: "left" is a position on the sample which is nearest to the evaporator during this growth while for "center" mostly AFM images were analyzed in the middle of the sample. This position on the sample has in average the same distance from the evaporator as during standard growth at $\alpha = 0°$. "right" is the analyzed position furthest away from the evaporator in comparison to the two other positions. Surprisingly, the graph shows much lower coverage than expected at position "left". This effect has nothing to do with the evaporation process, and is not caused by the large deposition angle. However, the molecular beam was covered by the side mounting plate of the heater resulted in a smaller deposition rate on the "left" side compared to the "not-shadowed" places on the sample. In chapter 3.2, the changes of the heater geometry to prevent this shwadowing effect are described in more detail. With this revision of the heater geometry, even larger deposition angles α (here up to 85°) can be achieved. The first growth series after the heater revision was similar to the first try from before. Six samples with increasing coverage were grown with the same deposition rate at room temperature and the same deposition angle of 75°. For the analysis five to six lateral positions on each sample were chosen for the AFM measurements which are displayed in Figure 4.23.

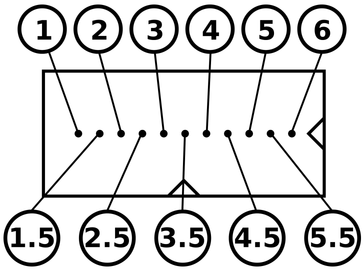

Figure 4.23: Sketch of a silicon sample (triangular marks on the lower and the right edge are made for better orientation during ex-situ AFM measurements) with the chosen eleven lateral positions for measurements where “3.5” indicates the center of each sample location. Lower numbers down to “1” indicate positions left from the center which means these positions are closer to the evaporator and higher numbers up to “6” indicate positions right from the center which means these positions are further away from the evaporator.

To get an overview of the different positions at each coverage, their topographic AFM images are presented in Figure 4.25. Row after row, the six samples are displayed which starts with the lowest coverage of about 0.05 ML up to a maximum of 1.14 ML. A brief first look reveals that not all samples show the same behavior in film growth due to the lateral position on the specimen. But all AFM images display that there is a change in density and size of the islands comparing left (near the evaporators orifice), center (a position with a distance from the Knudsen-cell comparable with growth at $\alpha = 0°$), and right positions (positions at larger distance of the evaporator). But for a better interpretation of this (visualized in Figure 4.25), an additional investigation of the coverage along the lateral positions is needed, which is provided in Figure 4.24.

In comparison to the graph in Figure 4.22(b), the graph in Figure 4.24 shows for similar coverage between 0.05 and 0.3 ML expected results and reveals again that the very low coverage at positions near the evaporator (“left”) for the first three attempts can be attributed to the described shadowing effect caused by the old heater geometry.
While for low coverage up to 0.3 ML, the samples #1-3 show for all lateral positions no change in the average coverage (refer to Figure 4.24), in Figure 4.25 it is evident that the islands have bigger size and lower island density at the outer positions than in the

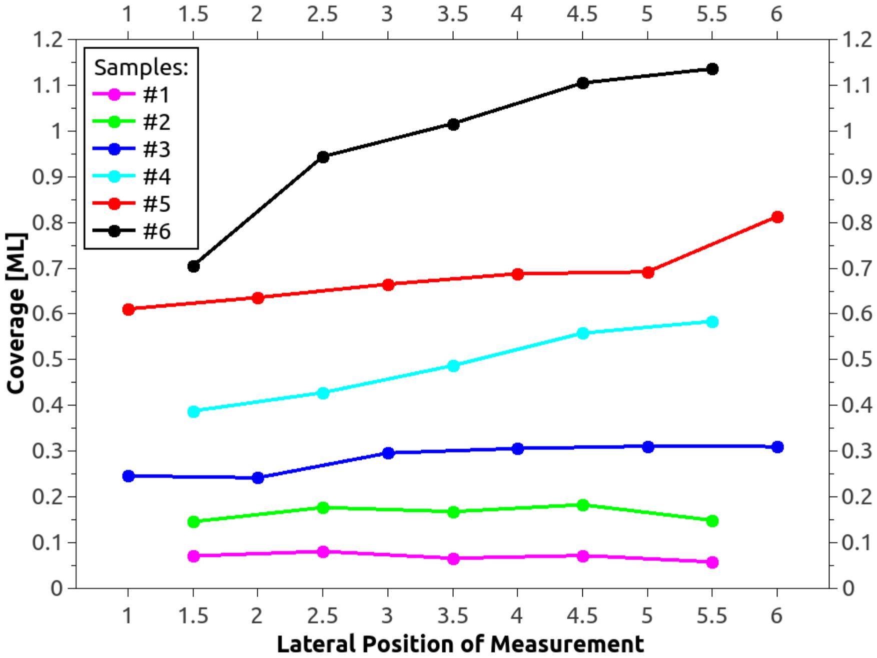

Figure 4.24: Graph of every single coverage in monolayers vs. the lateral position of the measurement from each of the six samples shown in Figure 4.25 grown at an $\alpha = 75°$. The data points are connected by lines only to guide the eye.

sample center. The same behavior prevails for the samples at higher coverage, but the graph in Figure 4.24 demonstrates obviously a trend with the coverage nearly increasing arithmetically which becomes steeper with higher coverage.
To investigate the influence of the deposition angle α for thin-film growth, samples were grown at an α of 70°, 75°, 80° and 85° with low coverage between about 0.05 to 0.14 ML. The AFM images of these samples are arranged tabularly due to their lateral position of measurement in Figure 4.26. The corresponding results of the coverage vs. lateral position for each deposition angle are presented in the graph of Figure 4.27. The lateral trend in coverage for each deposition angle is indicated with the use of linear fit curves.

While the islands on the sample at $\alpha = 70°$ in Figure 4.26 have dendritic shape at any lateral position, they change only in size and density. This is not the same for the growth at bigger deposition angles. While the islands in center position are all dendritic, they become bigger in size and more compact in shape for positions at the samples' edge. For an α at 80° and 85° the islands are becoming bigger in size and less dendritic in shape with increasing distance from the evaporator. At 85° there are no more islands with a 1^{st} layer of upright standing 6P molecules. Only very high needle-like structures appear.

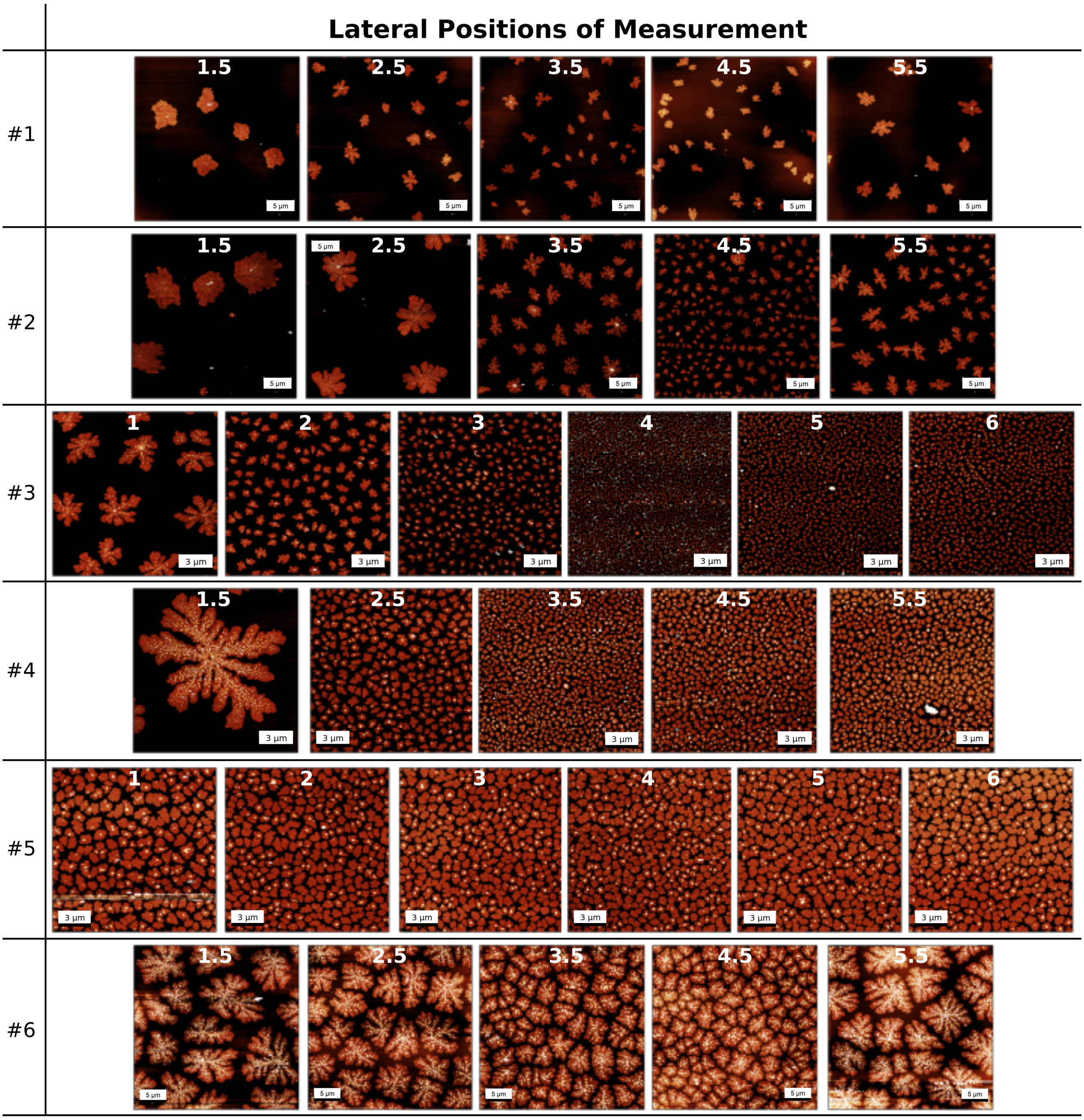
Lateral Positions of Measurement
#1
1.5
2.5
3.5
4.5
5.5
5 µm
#2
1.5
2.5
3.5
4.5
5.5
5 µm
#3
1
2
3
4
5
6
3 µm
#4
1.5
2.5
3.5
4.5
5.5
3 µm
#5
1
2
3
4
5
6
3 µm
#6
1.5
2.5
3.5
4.5
5.5
5 µm

Figure 4.25: AFM images of six samples grown at the same deposition angle of 75° arranged in a table. The six rows show AFM investigations of each sample at different lateral positions (indicated by numbers on top which are corresponding to the sketch in Figure 4.23). The rows are in ascending order towards their average coverage: #1 . . . $\theta_{\text{av}} = 0.07 \pm 0.01$ ML, #2 . . . $\theta_{\text{av}} = 0.17 \pm 0.02$ ML, #3 . . . $\theta_{\text{av}} = 0.29 \pm 0.03$ ML, #4 . . . $\theta_{\text{av}} = 0.49 \pm 0.07$ ML, #5 . . . $\theta_{\text{av}} = 0.68 \pm 0.06$ ML, #6 . . . $\theta_{\text{av}} = 0.98 \pm 0.15$ ML. (All images have a z-scale of 7 nm. The size of images from #1, #2, and #6 is 30x30 μm^2, while the others are 15x15 μm^2.)

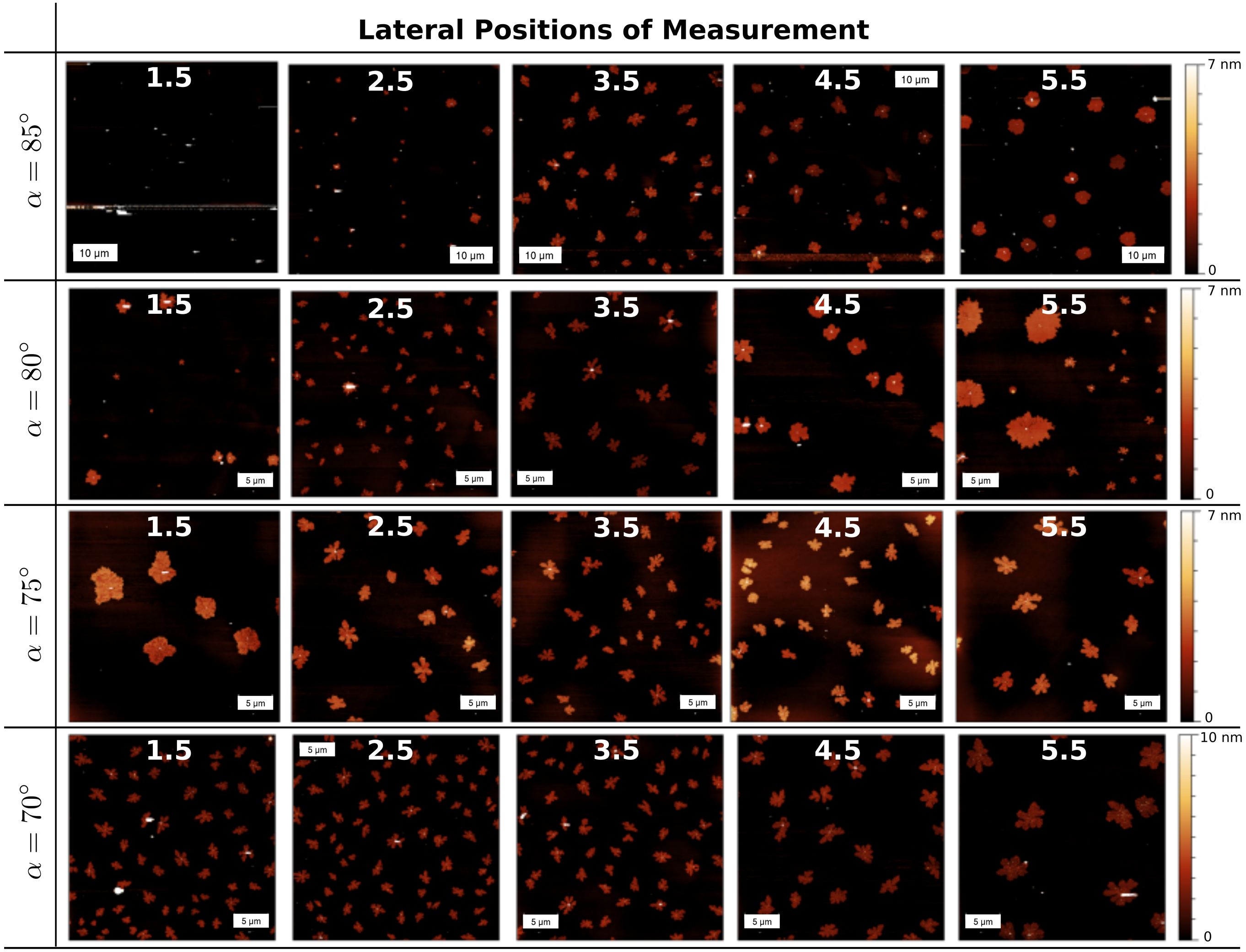
Lateral Positions of Measurement
α = 85°
α = 80°
α = 75°
α = 70°
1.5
2.5
3.5
4.5
5.5
10 µm
5 µm
7 nm
10 nm
0

Figure 4.26: AFM images tabularly arranged in four rows, starting with the biggest deposition angle of $\alpha = 85°$ down to 70°. The white numbers within center top of the images indicate their lateral position on the sample (after the sketch in Figure 4.23). The false color rulers at the right edge display the z-scale of the images in each row. The AFM images of the first row are 50x50 μm^2, while all others are 30x30 μm^2 in size.

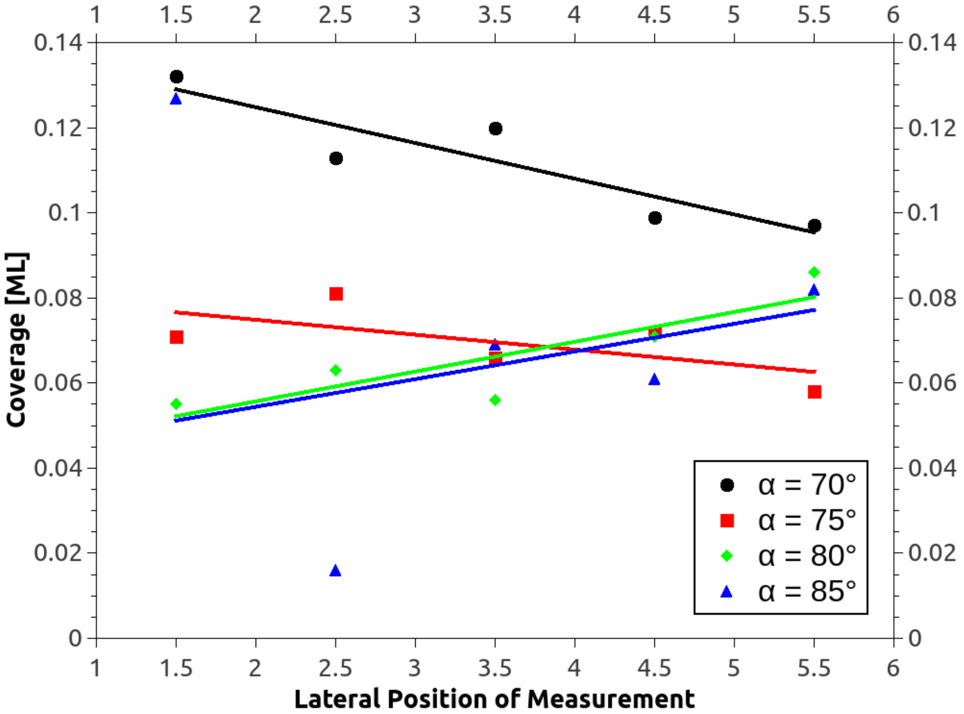

Figure 4.27: Coverage vs. the lateral position of the AFM measurements for four different deposition angles α of 70°, 75°, 80° and 85°. The trend in coverage due to the lateral position is indicated by linear fits through all data points of the appropriate sample (only for $\alpha = 85°$ the first two data points are outliers and were not taken into account for the linear fit).

The further away from the evaporator the bigger the islands become on this sample, while their shape changes from small compact to dendritic and again to a compact shape but bigger in size at the furthest lateral position.

Additional to this, the results of the graph in Figure 4.27 reveal that the coverage for deposition angles of 75° and lower becomes smaller with increasing distance from the evaporator. While for deposition angles of 80° and higher the coverage behaves the other way around, it increases with increasing distance from the evaporator. It needs to be noted that the difference in decrease or increase of the coverage vs. lateral position is not inherently big, only about 0.01 to 0.04 ML.

Whereas all the investigations mentioned above, don't reveal any expected major effect on the thin-film growth itself, the attention should be drawn to further analyze each single island in the thin film. This idea evolves from findings in earlier experiments and simulations for inorganic systems, already specified in chapter 2.1.4. There, they found changes in the surface morphology after growth under deposition angles above 50°. Examples are shown in Figure 2.14 and 2.15 (chapter 2.1.4). Farahzadi et al. [56] found even an evidence for this steering effect during organic thin-film growth, but they investigated this only for normal-incidence deposition. Taking the following ideas into account, (a) general morphological changes thin-film structures and (b) a steering effect taking place even for organic molecules, the next logical step is to examine and compare single 6P islands with each other. Earlier experiments showed that even the azimuthal particle beam direction and not only the deposition angle α has an influence on the geometry of the grown morphology (compare Figure 2.14 in chapter 2.1.4). Therefore, the shape of islands was investigated in analyzing their fractal geometry. If there is a similar effect in changing the shape of the islands, the islands should have an evident difference in the fractal geometry of those facing away and those facing into the molecular beam direction. In this case, one sample was chosen for further investigations. It underwent the same preparation and growth routine as the samples before, grown at RT with $\alpha = 75°$ resulting in a film thickness of $\theta_{\mathrm{av}} = 0.06 \pm 0.01$ ML. Figure 4.28 provides an overview how the plotted fractal data were deduced from the island shape.

The analysis procedure starts with taking an AFM image from center position of the sample. In Figure 4.28(a) islands of different size and shape are visual. In this example, 27 islands have been chosen for the fractal analysis which are colored by a green mask. Out of these 27 only 11 randomly chosen island undergo the next step of analysis (marked by numbers in Figure 4.28(a)). Each of these chosen islands is now split into left and right side, displayed in Figure 4.28(b). To split the pictures properly, the islands were split along a line through their center of mass. The contrast of these pictures has to be changed to brighter colors of the island for getting a better contrast between the bright island and the dark background of the surface resulting in a better performance of the fractal calculation. In a next step, the fractal dimension D_{f} of each island as a whole and from the left and the right side each were performed in three different ways. The first approach was done with the simple calculation by varying the radius r according to the center of mass of the island $M(r)$ with

$$D_{\mathrm{fc}} = \frac{\ln M(r)}{\ln r} \quad . \tag{4.2}$$

These results are shown in Figure 4.28(c) in red. For the results displayed in green within

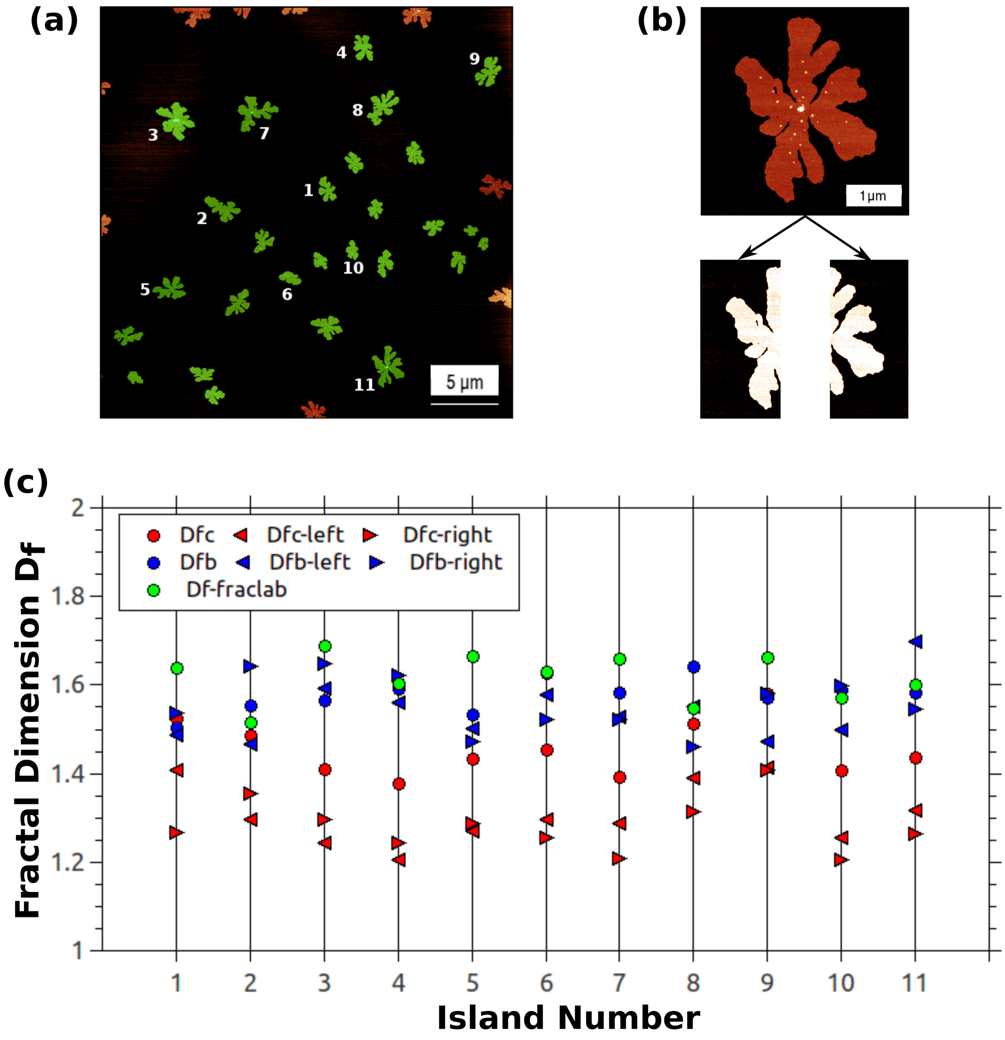

Figure 4.28: (a) 30x30 μm^2 AFM image with a z-scale of 7 nm from the center position of a sample (grown at RT with $\alpha = 75°$ and $\theta_{av} = 0.06 \pm 0.01$ ML); 27 islands are masked in green which seem to be useful for fractal analysis; 11 out of these 27 are marked with numbers which were taken for the analysis. (b) Example of one single island: its image is split into two pictures (left – facing side, right – far side according to beam direction) which were investigated separately. (c) Results of each of the 11 islands: D_{fc} (in red) marks the fractal dimension calculated by varying the radius, D_{fb} (in blue) shows results from using classical box counting method, and D_f-fraclab (in green) indicates the estimated fractal dimension yielded from the software FracLab© (circles indicate the fractal dimension of the whole island and the triangles show the fractal dimension of each left and right side of the islands).

Figure 4.28(c), eq. (2.29) from chapter 2.1.3 of classical box-counting method was used. Both ways of calculation were made in MATLAB. As a third way to estimate the fractal dimension, the program FracLab© from the french company INRIA which uses routines based on MATLAB and has been developed in C-code was applied. Its fractal analysis is using an advanced kind of the classical box-counting method. Limitations in the usage of this program makes it impossible to extract feasible results for the left and right side pictures. So, only the dimensional calculations for the entire islands were added to the graph in Figure 4.28(c) in green circles. Comparing these three approaches with each other, each method leads to a slightly different value of D_f. The graph in Figure 4.28(c) reveals that the average values of D_f are between 1.46 and 1.62, where using eq. (4.2) leads to lower values and FracLab© to higher values. Table 4.1 underlines this in presenting the average values for each method. Additional, it lists even the average values of D_f for the investigation of the left and right island sides.

Although Figure 4.28(c) together with Table 4.1 reveal a difference between left and right side, there is no evidence that one side has a distinguished value of D_f in comparison to the other.

Table 4.1: List of all average values of the fractal dimension D_f obtained with three different kind of calculations (D_fc . . . fractal dimension calculated by varying the radius, D_fb . . . using classical box counting method, D_f-fraclab. . . using FracLab©).

calculation method	total island	left island side	right island side
D_fc	1.46 ± 0.06	1.31 ± 0.07	1.28 ± 0.06
D_fb	1.58 ± 0.04	1.54 ± 0.07	1.56 ± 0.06
D_f-fraclab	1.62 ± 0.05	–	–

To complete the investigations of 6P deposition at grazing incidence, DLA simulations were performed for a single island starting with a 400x400 lattice. The sticking coefficient k_s was set in the simple MC algorithm after Witten and Sanders [37] from 0.001 to 1 for four different simulations (compare Figure 4.29). A lower k_s allows the particle to diffuse longer at the island's edge, while k_s equal 1 means that the particle sticks at the island directly after touching it. This procedure was already explained in chapter 2.1.3. These four simulations were done twice. In the first case, the particles were randomly introduced at points from all sites around the growing island simulating the growth at normal incidence. In the second case, the simulation was accommodated to the growth at grazing incidence. Therefore, the introduced particles were allowed only to arrive randomly from left side. After finishing all simulations, the fractal dimension of each received morphology was calculated similar to the images of real grown islands. The results of the simulations are presented in Figure 4.29.

The simulation demonstrates that a bigger k_s leads to a more dendritic shape with a lower fractal dimension. Figure 4.29 also exhibits the difference in shape and fractal dimension between normal and grazing incidence. In comparison with real grown islands like in Figure 4.28(a), the shapes from simulations for $k_s = 0.01$ are in good agreement with reality. The values of D_f from the real sample agree well with $D_\mathrm{f} = 1.66$ from the simulations for particles which prefer to arrive from one side towards the island.
But a closer look makes it obvious that a comparison of D_f between really grown and simulated islands is not so easy, because the simulated islands seem to be more ramified at their edges than the islands from AFM measurements. In this case, it would have been better to do all the measurements with HIM instead of AFM. Like displayed in Figure 4.30, the quality and resolution of a HIM image is much better than AFM. It's evident that such images imply a change in the result of fractal dimension of really grown islands. But within this work no further investigations were done in this direction. For further experiments, using super-sharp AFM probes (e.g. carbon whisker with 2 nm radius on soft cantilevers) and careful scanning can improve significantly the resolution of the images.

In conclusion, even if a steering effect exists for the deposited organic molecules like in inorganic growth there is no evidence that this results in a different thin-film morphology nor in a different island shape of submonolayer thin-films for growth under grazing incidence (with deposition angles higher than 50°). But two other things become evident in these investigations. The more the sample is tilted towards the molecular beam, the lesser the coverage becomes along the sample's lateral axis at the site facing the evaporator. The bigger the coverage is, the steeper the increase of coverage becomes for positions further from the evaporator. And these may originate from an influence by steering. In general, MC simulations don't reveal that the shape of the islands during grazing incidence changes according to the comparison of the fractal dimensions. But the simulations are in good agreement with real growing. The island shapes look comparable for a sticking coefficient $k_s = 0.01$ and a fractal dimension $D_\mathrm{f} = 1.66$ (see Table 4.1).

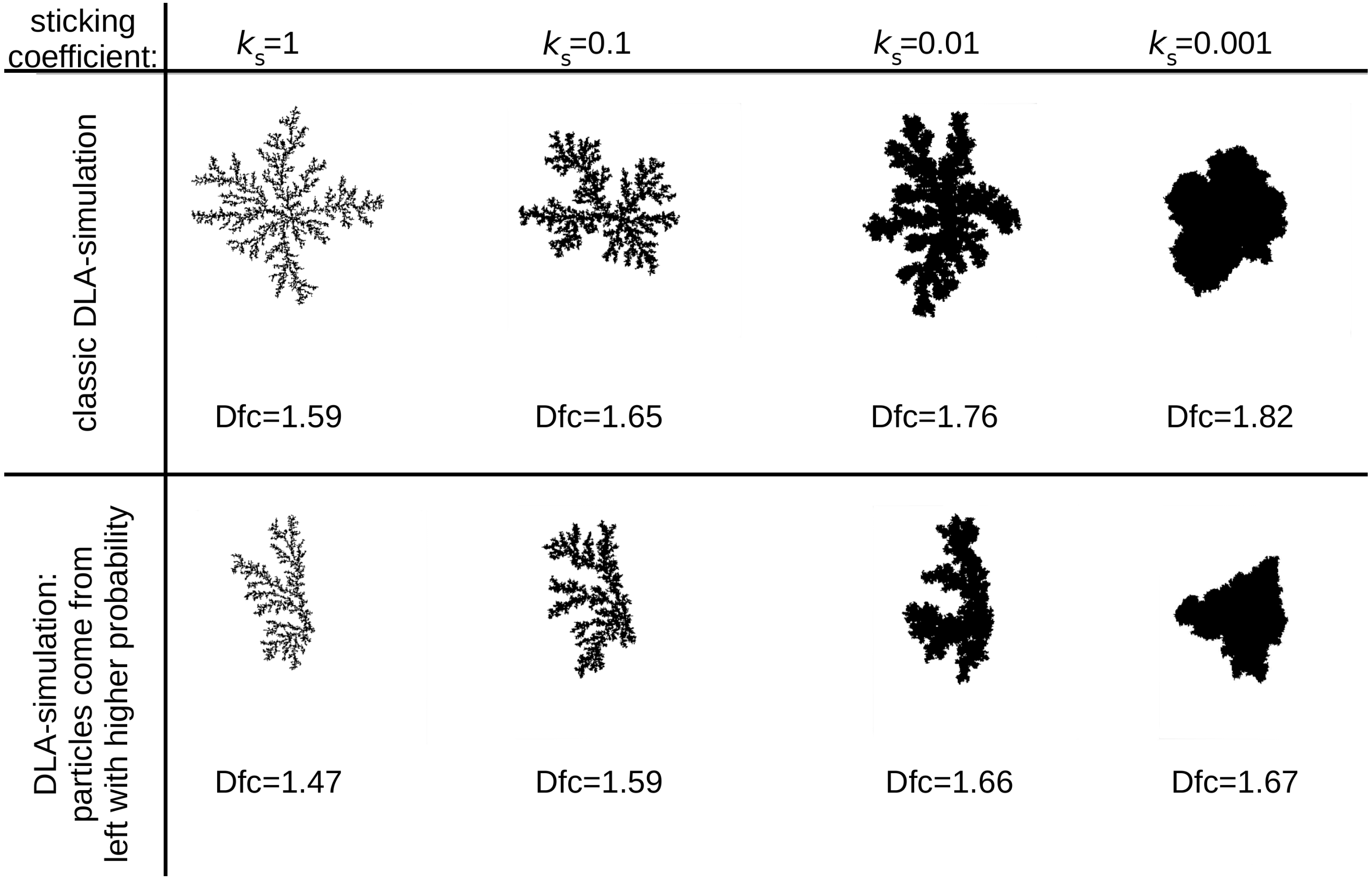
sticking coefficient:
k_s=1
k_s=0.1
k_s=0.01
k_s=0.001
classic DLA-simulation
Dfc=1.59
Dfc=1.65
Dfc=1.76
Dfc=1.82
DLA-simulation: particles come from left with higher probability
Dfc=1.47
Dfc=1.59
Dfc=1.66
Dfc=1.67

Figure 4.29: Representative simulation results and their calculated fractal dimension D_f of two series ofDLA simulation with different sticking coefficient k_s are displayed in two rows. While the upper row shows pictures with the expected shape of DLA growth with particles coming randomly from all sides, the lower row contains pictures where the particles were forced to arrive randomly only from the left side.

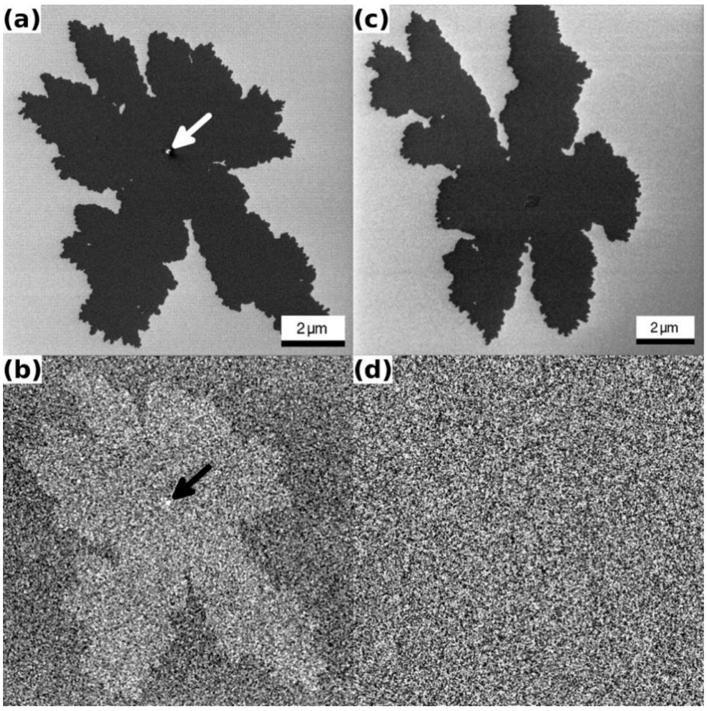

Figure 4.30: HIM images of two different single-layer 6P islands on silicon oxide, recorded with a primary energy of 20 keV and an He^+ ion dose of $3.21 \cdot 10^{15}$ cm^{-2}. (a) & (c) are images of the two islands and (b) & (c) are the corresponding backscattered helium images (While the island is visible in (b), there is nothing in (d) which is explained by a recording with a sample tilt of 10°). In (a) & (b) is a small second layer visible, marked by arrows. (From [147])

4.4 Hexagonal shaped islands in second and higher layers

In the previous sections the main focus of attention was on the nucleation and growth of first-layer islands consisting of upright standing 6P molecules. In this section the attention will be drawn onto 6P islands in second and higher layers. Owing to the Ehrlich-Schwoebel barrier at the island edges, it is common for 6P molecules starting to build second-layer islands on top of first-layer islands already before a complete coalescence of the first layer. In the works of Hlawacek et al. [4] and Potocar et al. [27], who already investigated the growth of 6P on amorphous substrates before, the careful reader is able to observe hexagonal structures of the islands within second and higher layers (compare Figure 4.31 which is a reproduction adapted from [8]). But so far, there was no focus on this behavior. This section here is dedicated to these hexagonal islands in subsequent layers.

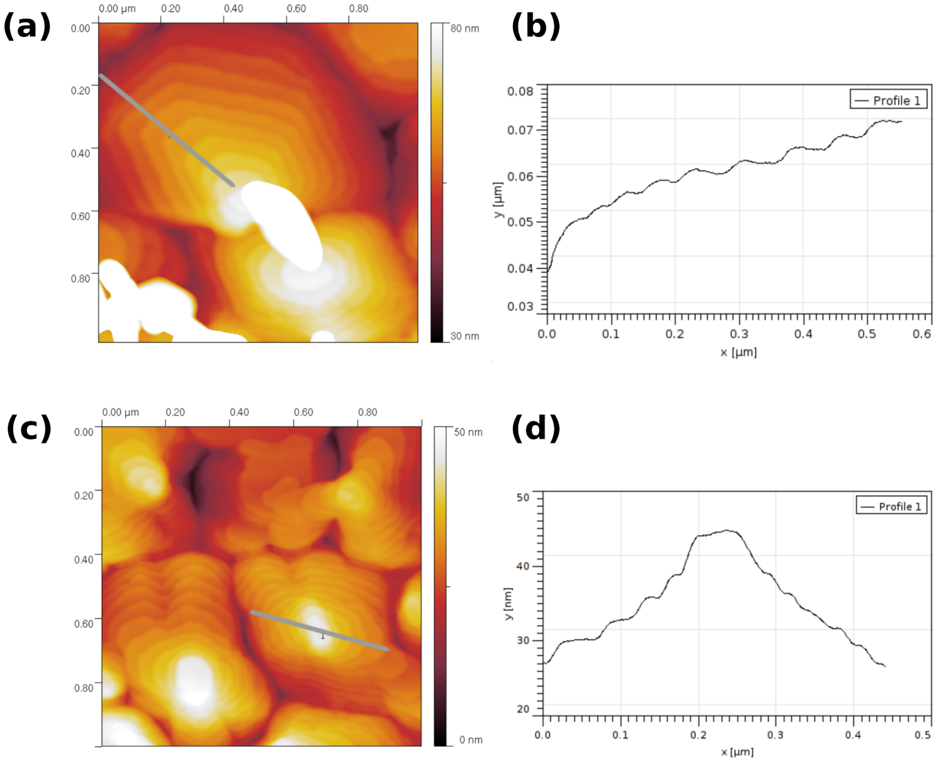

Figure 4.31: (a) 1x1 μm^2 topographic AFM image of a 30 nm thick 6P film on ion-bombarded mica with a z-scale of 80 nm showing well-defined hexagonal steps. (b) Height profile along the cross section marked in (a). (c) 1x1 μm^2 AFM image with a z-scale of 50 nm showing the mounded surface of a 50 nm thick 6P film on SiO_2 with the corresponding cross section of a single mound in (d). (Adapted from [8])

Figure 4.31 reveals already, in comparison with the analysis from previous sections in this thesis, that most of the structures which build a second layer prefer the hexagonal shape. But Figure 4.31(c) shows that these mounds can coalesce later in higher layers or form other structures which might trace back to a hexagonal base. The height profiles in Figure 4.31(b) and (d) point to the existence of the upright standing of 6P molecules which have a similar step height like the molecule length.

Here, one sample with 6P grown at room temperature (RT) on ion-bombarded mica (provided by the colleagues Prof. A. Winkler and T. Potocar from the Graz, Austria) and four samples grown in Leoben at RT, 313 K, 323 K, and 333 K on SiO_2 substrates have been investigated. The average film thickness of the mica sample is 0.98 ML and of the SiO_2 samples between 0.76 and 1.08 ML. While the deposition of 6P onto mica last longer with a deposition rate of 0.0175 ML/min and the deposition onto SiO_2 was much shorter with 0.06 ± 0.01 ML/min, the results are nevertheless in good agreement with each other. Figure 4.32(a) and Figure 4.33 present a first idea about these five samples how second-layer islands look like on irregularly shaped first layer islands.

The first investigation of these samples was dedicated to the second-layer islands which showed in average an elongated hexagonal shape. Profiles of cross sections together with height distributions (for example in Figure 4.32(b) and (c)) illustrate that on amorphous substrates 6P forms mounds of upright standing molecules with a larger tilt angle towards the substrate surface for lower layers, which was already found and explained by Hlawacek et al. [4].

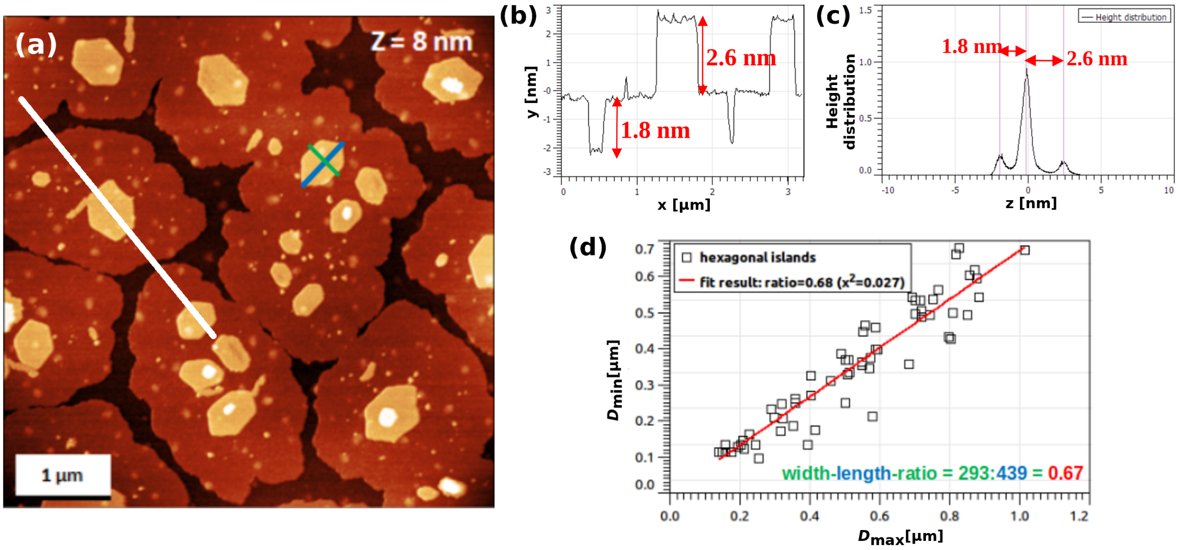

Figure 4.32: (a) 5x5 μm^2 AFM topographic image with a z-scale of 8 nm from the ion-bombarded mica sample. (b) Height profile of a cross section marked by a white line in (a). (c) Height distribution for the whole AFM image in (a). (d) Graph of a width-to-length-ratio analysis out of dozens of hexagonal-shaped-second-layer islands (D_{min}, D_{max}...width and length of the investigated islands; each aspect ratio was obtained from linear fit functions like the one in red). Inset displays exemplarily the width-to-length-ratio calculation marked in (a) by green (width) and blue (length) lines.

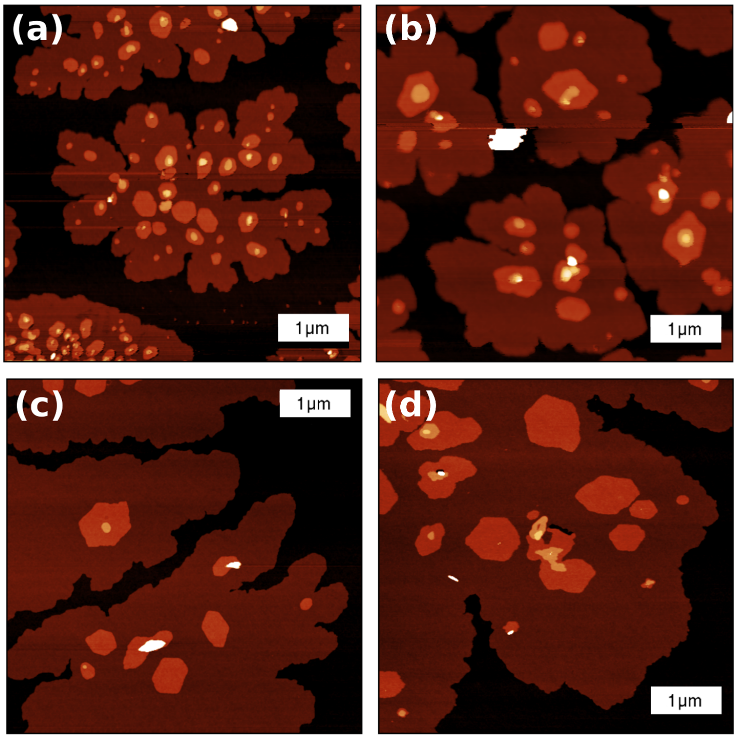

Figure 4.33: 5x5 μm^2 AFM images of 6P on SiO_2 with a z-scale of 15 nm. (a) grown at RT with $\theta = 0.89$ ML and $R = 0.059$ ML/min, (b) grown at 313 K with $\theta = 1.08$ ML and $R = 0.072$ ML/min, (c) grown at 323 K with $\theta = 0.76$ ML and $R = 0.051$ ML/min, and (d) grown at 333 K with $\theta = 1.05$ ML and $R = 0.070$ ML/min.

Figure 4.32(d) is an example how the width-to-length ratio was estimated. For hundreds of second-layer islands on mica this results in a ratio of approximated 0.67 ± 0.15 which pronounces the elongated shape of this island geometry. The same investigation was done for 6P second-layer islands on SiO_2. Table 4.2 summarizes the results of the width-to-length ratio for all five samples.

What Figure 4.33 already supports and which is documented with Table 4.2, is the conjecture that with higher substrate temperature even the second-layer islands tend to become bigger in size. And for every sample, on both substrates, at any temperature can be found only elongated hexagonal-shaped islands in the second layer.
The next effort was to investigate the interior angles of these elongated hexagonal islands. The results for the four samples are displayed in Figure 4.34. Therefore at about hundred second-layer islands for each sample the six interior angles of each hexagon were measured and then put together in histograms which are added in Figure 4.34.

Table 4.2: Listed values of the average width-to-length ratio for the four investigated samples based on hundreds of hexagonal second-layer islands.

Substrate	$T_{\text{substrate}}$	Aspect ratio (width/length)
ion-bombarded mica	RT	0.67 ± 0.15
SiO_2	RT	0.65 ± 0.17
	313 K	0.69 ± 0.14
	323 K	0.71 ± 0.17
	333 K	0.70 ± 0.16

The AFM images in Figure 4.34(a) and (b) exhibit that at each hexagonal island there are two angles somehow smaller than the four others which underlines again the elongated shape of the hexagonal second-layer islands. But only a closer look at the histograms reveals that over all second-layer islands with this elongated hexagonal shape on both substrates 104° and 126° seem to be the two preferential interior angles which is again displayed in Figure 4.35(a).

It's possible to identify these angles together with their corresponding facet orientations in a 2D map of the 6P ground plane (001) like in Figure 4.35(b). These findings lead to the idea starting simulations on 6P building a bulk structure (see chapter 2.2 and [70, 71]) of upright standing molecules onto an already existing 6P layer which are presented in Figure 4.35 and Figure 4.36.

Dimitrii Nabok and Giulio Biddau from the Chair of Atomic Modeling and Design of Materials at the University of Leoben, Austria, were performing the simulations. Nabok found using empirical force-fields in the facet orientation [10] that the energetic preferable equilibrium shape based on attachment energy is octagonal as is presented in Figure 4.35(c) with its interior angles. Figure 4.35(d) illustrates how the upright standing molecules are arranged in this equilibrium 6P crystal shape with the typical herringbone crystal structure after Baker [70, 71]. This octagonal structure was then the base for Biddau's molecular dynamics (MD) simulation based on the work of Della Valle et al. [148] to explain how a 6P molecule behaves while diffusing along the edges of this equilibrium crystal. The result of his simulation is illustrated in Figure 4.36 with a graph of the adsorption energy of a single 6P molecule versus its path along three side edges of an existing 6P island.

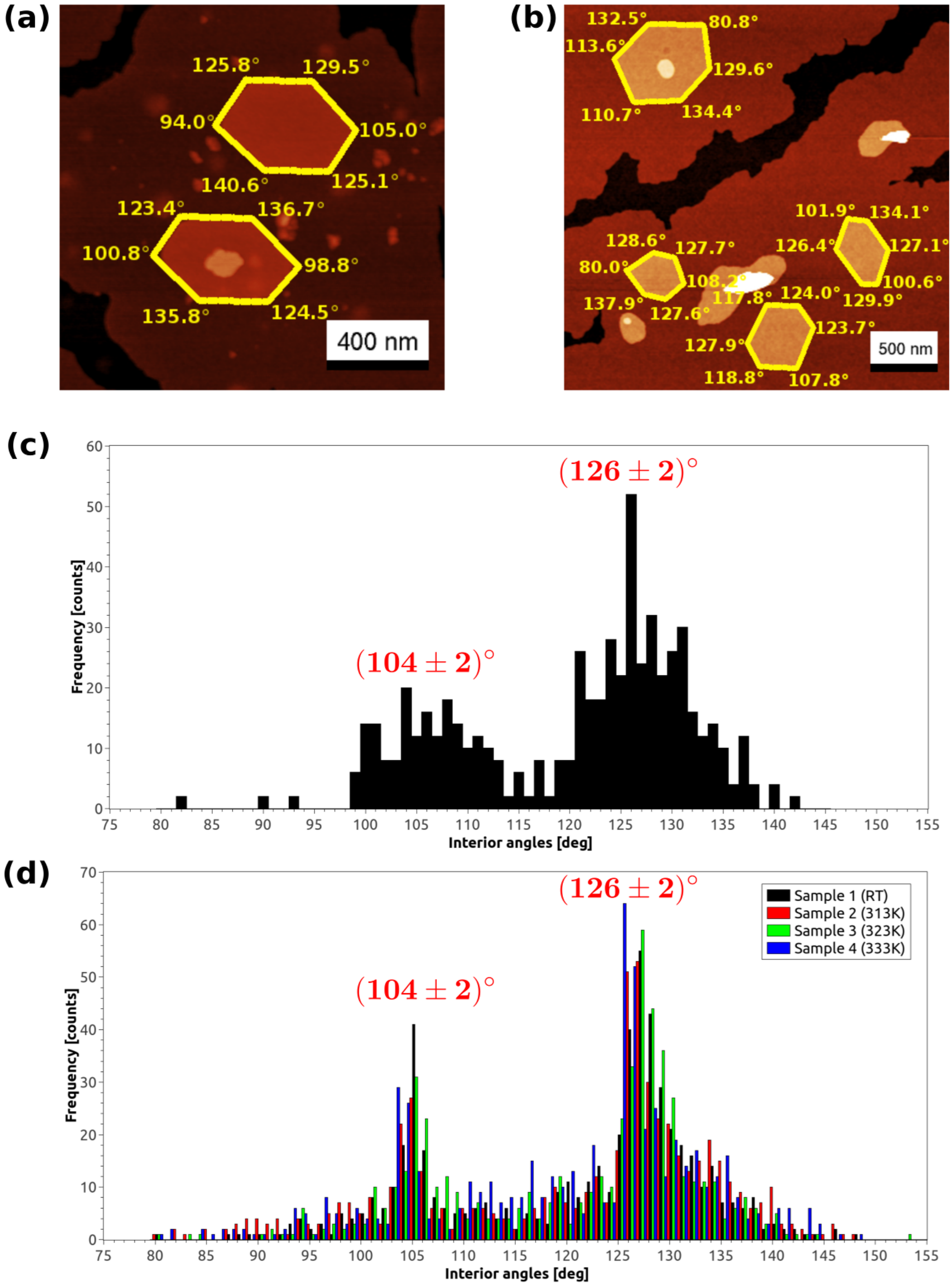

Figure 4.34: Topographies of (a) a 1.6x1.6 μm^2 AFM image of 6P on mica and (b) a 2.5x2.5 μm^2 AFM image of 6P on SiO_2 (both with a z-scale of 10 nm) which show exemplarily how the measurement of the interior angles of the hexagonal islands took place (the island shape is marked in yellow together with each interior angles displayed). Histograms of interior angles from hundreds of hexagonal second-layer islands on (c) ion-bombarded mica and (d) SiO_2.

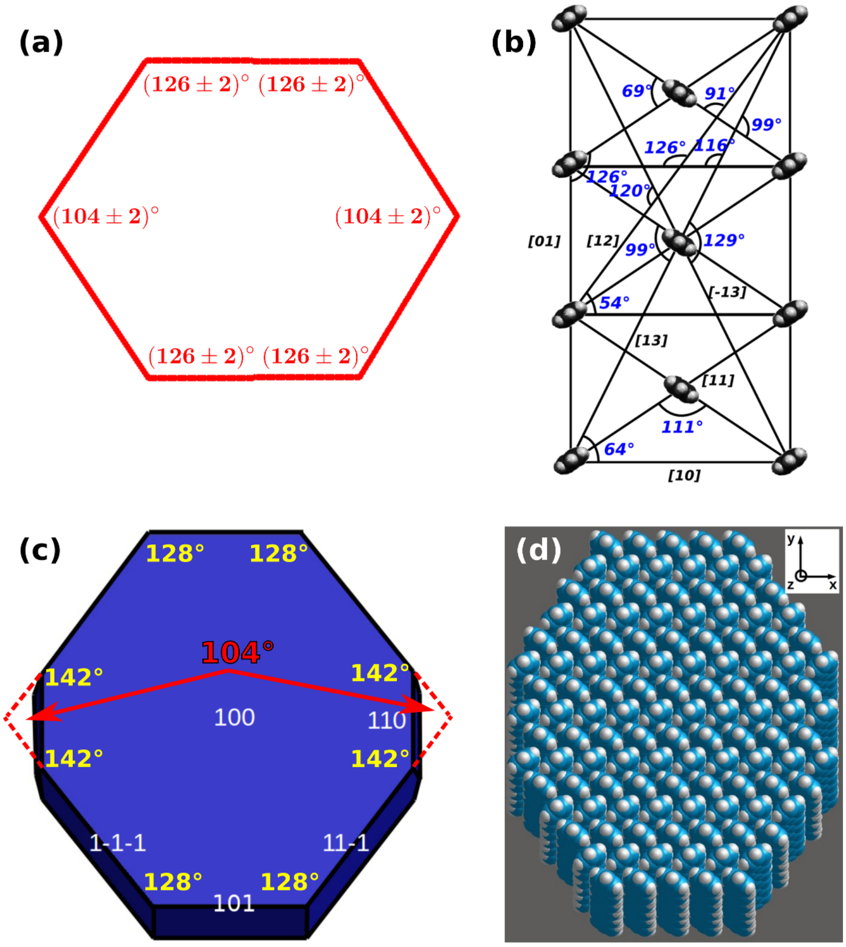
(a)
(126 ± 2)°
(126 ± 2)°
(104 ± 2)°
(104 ± 2)°
(126 ± 2)°
(126 ± 2)°
(b)
69°
91°
99°
126°
116°
126°
120°
[01]
[12]
99°
129°
54°
[-13]
[13]
[11]
111°
64°
[10]
(c)
128°
128°
104°
142°
142°
100
110
142°
142°
1-1-1
11-1
128°
128°
101
(d)
y
z
x

Figure 4.35: (a) Sketch of the most preferable shape of the hexagonal second-layer islands with the resulting two interior angles. (b) The possible facet orientations are shown in a 2D map with their angles in the ground plane(001) of the monoclinic unit cell from 6P [70]. (c) Simulations using empirical force-fields show for facet orientation [10] that the equilibrium shape of a 6P single crystal is octagonal (interior angles are in yellow and the expected angles of 104° are indicated with red arrows). (d) The equilibrium shape with single 6P molecules arranged in the typical herringbone structure shown with a slight molecular tilt of 17° towards the surface in y-direction. ((c) and (d) are a courtesy by D. Nabok)

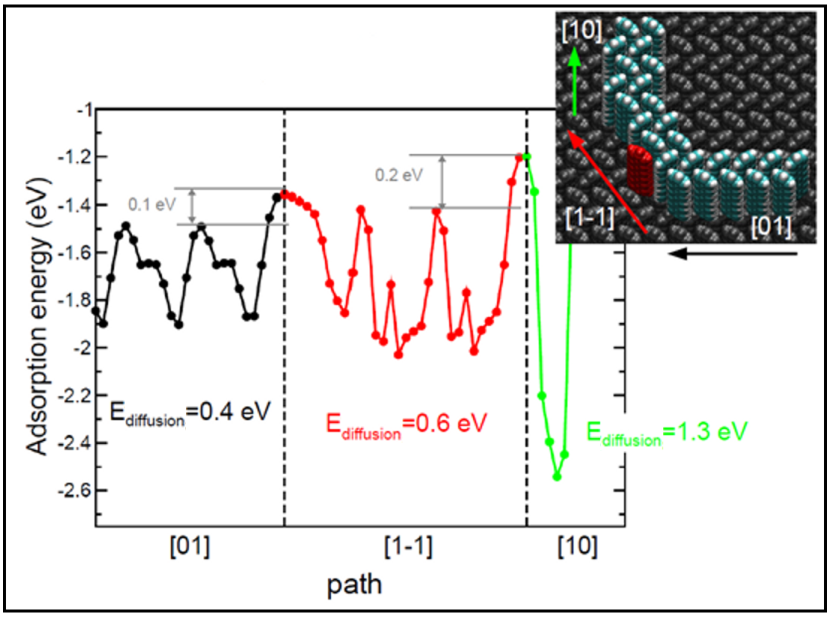

Figure 4.36: Adsorption energy versus the path of a 6P molecule along three side edges marked with their facet directions obtained from the equilibrium crystal shape of Figure 4.35(c). The three different colors of the curve corresponds with the arrows indicating the path of a 6P molecule (marked in red) along the facet directions displayed in the inset. The different energies $E_{\text{diffusion}}$ of each diffusion barrier is added to the regarding facet. (Courtesy by G. Biddau)

MD simulations reveal that, due to kinetically limited edge diffusion, the molecules have different sticking coefficients by energy barriers at facets with different orientation, indicated in Figure 4.36 where the highest diffusion barrier is 1.3 eV at the [10] facet. As a consequence, a 6P molecule prefers to stick at the [10] facet and diffuses easily at the [01] facet which results finally in a crystal shape of an elongated hexagon with the measured interior angles displayed in Figure 4.35(a).

In a next step, the orientation of these elongated hexagons of the second layer was investigated. AFM images of the topography of these films disclose that there are on both substrates hexagonal second-layer islands which have the same orientation on the underlying irregular-shaped island of the first layer, but show even different orientations on the same single first-layer island at other positions (compare for example Figure 4.32(a) and Figure 4.33). With the help of Quan Shen from the Institute of Physics at the University of Leoben, Austria, images from the 6P film on ion-bombarded mica were recorded with friction force microscopy (FFM) and transverse shear microscopy (TSM), which are described in chapter 2.5. FFM and TSM investigations help to understand what is responsible for the orientation of the hexagonal second-layer islands. A first result is shown in Figure 4.37.

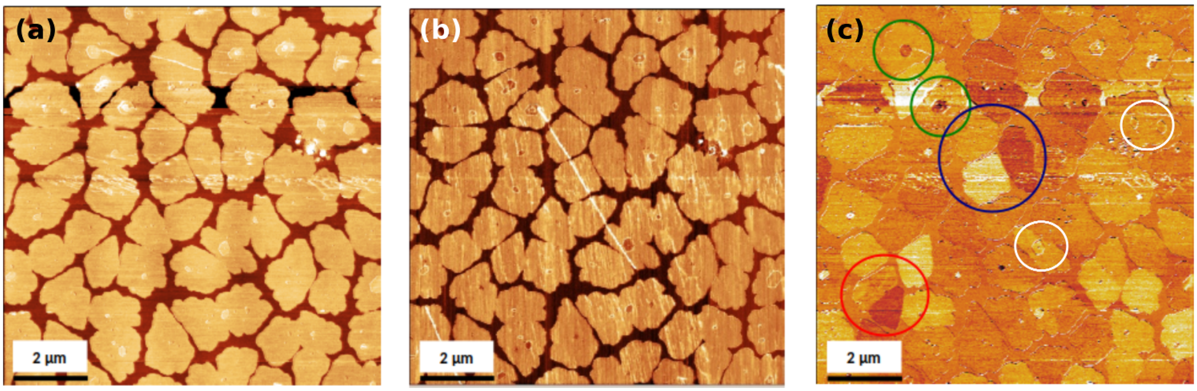

Figure 4.37: (a) 10x10 μm^2 AFM image with a z-scale of 12 nm of the topography from a center position of the 6P film grown on ion-bombarded mica. Corresponding FFM image (b) with a z-scale of 1.2 V and TSM image (c) with a z-scale of 0.5 V from the region shown in (a). In (c) a blue circle marks three first-layer islands with different molecular orientation, a red circle marks different molecular orientation within one single first-layer island, white circles mark second-layer islands with same molecular orientation like their first-layer islands, and green circles mark second-layer islands with different molecular orientation than their first-layer islands. (Courtesy by Q. Shen)

While in Figure 4.37(b) the FFM investigation only shows a difference in the stiff substrate and the soft 6P film on top of it, the TSM image in Figure 4.37(c) reveals much more useful information. For instance, the irregular first-layer islands themselves exhibit different molecular orientations (compare Figure 4.37(c) marked by a blue circle) which means that all 6P molecules within one single island are tilted in the same azimuthal direction towards the surface, but from island to island the main tilt direction seems to differ. Like it is displayed in Figure 4.37(c) marked by a red circle, it happens that there occur two different molecular orientations in one single island. With green and white circles two different cases concerning the molecular orientation of second-layer islands in comparison with their underlying first-layer islands are marked in Figure 4.37(c).

Additional TSM investigations – performed and interpreted by Q. Shen – have similar results like mentioned before with Figure 4.37(c), and even reveal something new and

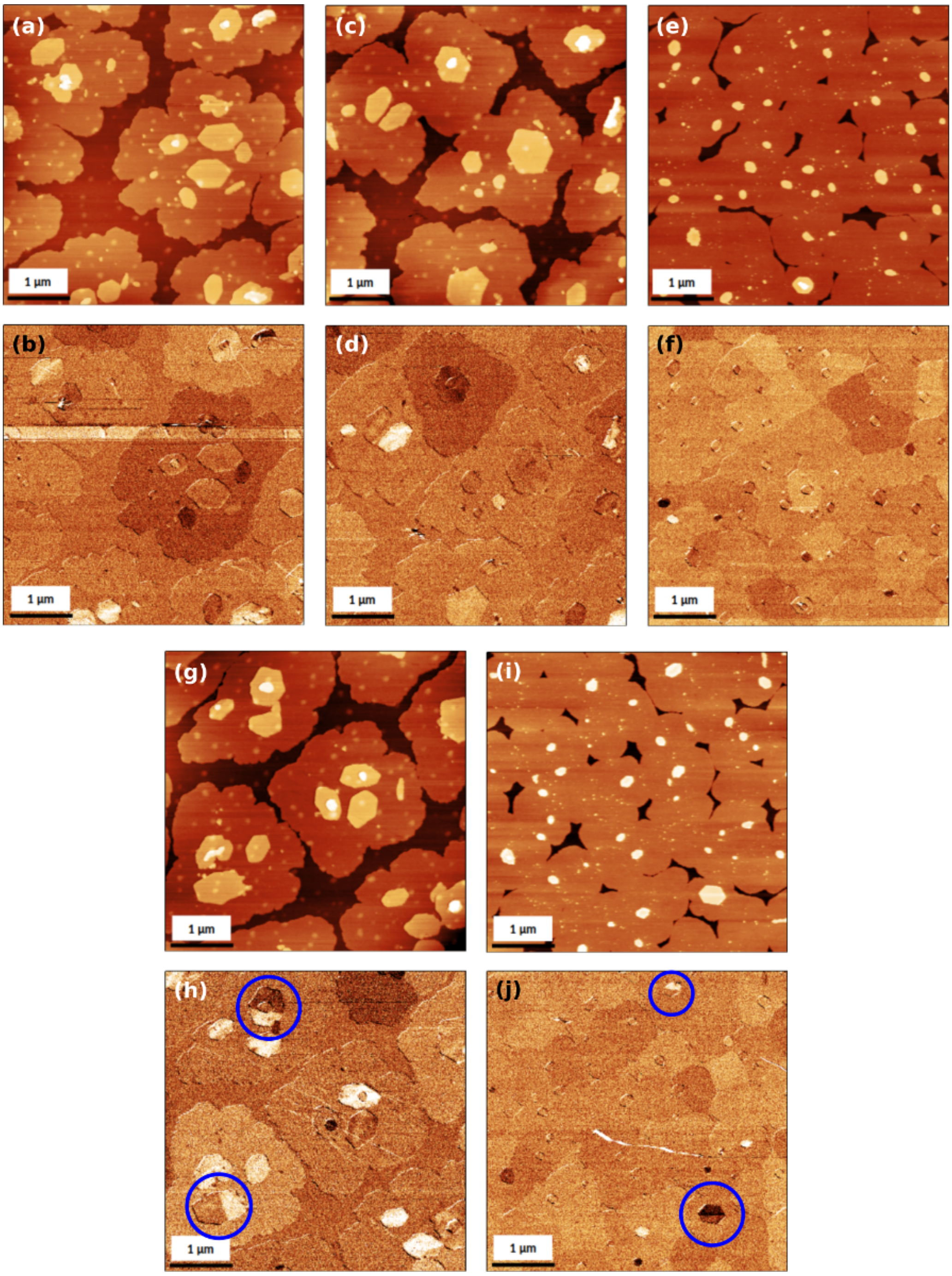

Figure 4.38: 5x5 μm^2 AFM topographic images with their corresponding TSM images of five different positions at the sample with 6P on ion-bombarded mica. (a) Topography with a z-scale of 10 nm and (b) its TSM image; (c) topography with a z-scale of 9 nm and (d) its TSM image; (e) Topography with a z-scale of 8 nm and (f) its TSM image; (g) topography with a z-scale of 10 nm and (h) its TSM image; (i) topography with a z-scale of 6 nm and (j) its TSM image. All TSM images have a z-scale of 1 mV. Blue circles in (h) and (j) indicate the rare case of different molecular orientations within single hexagonal second-layer islands. (Courtesy by Q. Shen)

unexpected. First of all Figure 4.38(b), (d) and (h) show that hexagonal second-layer islands can appear in different molecular orientations to each other and their underlying first-layer island. Secondly, Figure 4.38(b) and (h) display examples of hexagonal third-layer islands which show a different molecular orientation than the underlying second-layer islands, whereas in other cases the higher layers seem to have the same molecular orientation like the first hexagonal-shaped islands in the second layer. A very unexpected, but very rare, case is presented in Figure 4.38(h) and (j) marked with blue circles. There can exist some hexagonal second-layer islands which are with a well elongated hexagonal shape but divided into two regions with completely different molecular orientations. There is even one hexagonal third-layer island in Figure 4.38(h) which was grown exactly on the border between the two molecular orientations of the underlying second-layer island.

All these discussed investigations lead to the conclusion that the growth on amorphous substrates like ion-bombarded mica and SiO_2 results in first-layer islands with an irregular shape, but beginning with a second-layer nucleation the new formed islands tend to achieve an elongated hexagonal shape due to the herringbone crystal structure of the underlying first layer of 6P and to the behavior of 6P molecules while diffusing along different edges on the equilibrium crystal shape. Molecular dynamics simulations reveal that this edge diffusion must lead to the predominant hexagonal shape based on the octagonal equilibrium shape, because there is a higher probability for the molecules to incorporate into the [10] facet. TSM investigations show, while many second-layer islands have the same molecular orientation like their underlying first-layer, that there exist often second-layer islands with different molecular orientation than the first layer on top of one single first-layer island. The rare case of two different molecular orientations within one single second-layer island can occur, but the reason for this is still unclear.

4.5 6P thin-film growth on BaF_2

Whereas the previous sections dealt with the growth of 6P on amorphous substrates, this section is dedicated to the growth on a substrate with a crystalline surface. Like described in chapter 2.3.3, barium fluoride (BaF_2) can be easily cleaved. The next steps in growing thin films of 6P on BaF_2 were shortly explained in chapter 3.1.3. All AFM measurements were performed under ambient conditions. Figure 4.39 and Figure 4.40 summarize the investigations and their findings.

The screenshot in Figure 4.39(a) shows small triangular shapes on the surface of the BaF_2 sample which reminds of the V-shaped terraces mentioned in chapter 2.3.3 which occur if the cleavage is done along the $[\bar{1}10]$ direction. Only the topography in the AFM image of Figure 4.39(b) verifies that the growth took place on V-shaped terraces. Figures 4.39(b) and (c) reveal the interesting result that on a well-defined crystal surface (even not ion-bombarded) a thin-film consisting of upright standing 6P molecules can evolve. This is proven by the visualized step heights in the cross section in Figure 4.39(d) and underlined by the height distribution in Figure 4.39(e) displaying an average island-height of about 2.6 nm. This was proven with other BaF_2 samples treated the same way but with other film thickness (compare the example in Figure 4.40).

The close-up in Figure 4.40(b) illustrates again the possibility of hexagonal-shaped mounds like investigated in the section 4.4 before.

Concluding, there appears during thin-film growth of 6P on a BaF_2 crystalline surface islands of upright standing molecules which were only found before on amorphous surfaces. And during the growth, the thickness of the 6P film on BaF_2 is consisting of the same hexagonal mounds like investigated on amorphous substrates. Most likely this leads to the same explanation of the underlying growth mechanisms which were already stated in the sections before. Considering contamination, the samples were handled carefully, and were freshly cleaved inserted into UHV, and they got the same annealing procedure like the SiO_2 sample as a cleaning step before growth. Nevertheless, contamination of the surface should never excluded. And contamination means a larger number of nucleation sites which influences significantly the growth morphology.

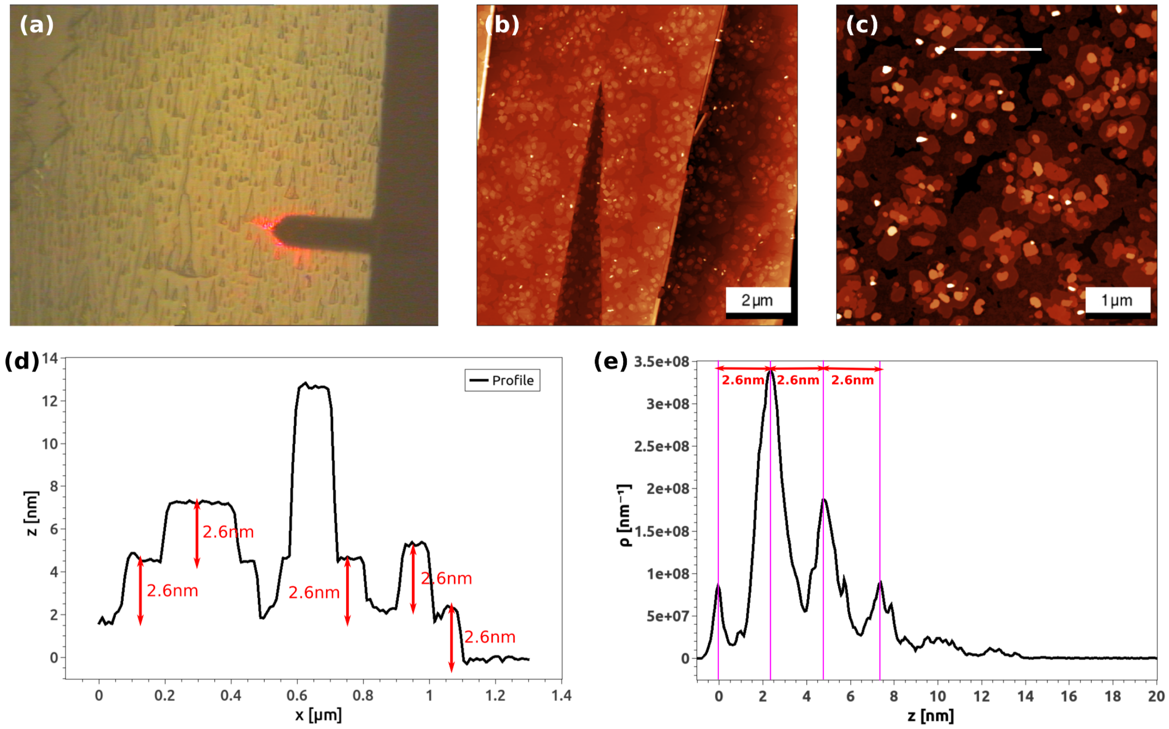

Figure 4.39: (a) Screenshot of the video camera attached to the MFP-3D Asylum Research taken during the positioning of the LASER beam onto the cantilever which shows the surface of the transparent BaF_2 substrate. (b) 10x10 μm^2 AFM image of a 6P thin-film morphology on some terraces of the BaF_2 crystal with a z-scale of 60 nm ($\theta = 1.59$ ML). (c) Detailed AFM image of the 6P film on a single terrace of the BaF_2 crystal (5x5 μm^2 with a z-scale of 25 nm). (d) Graph of the cross section along the white line marked in (c). (e) Height distribution of the 6P thin film of (b) and (c).

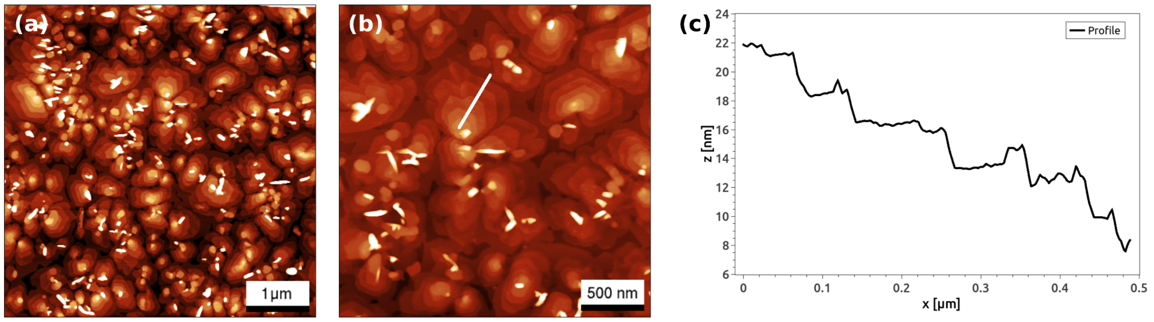

Figure 4.40: (a) 5x5 μm^2 AFM topographic image with a z-scale of 25 nm of a 6P film on BaF_2 with $\theta = 3.43$ ML. (b) A 2.5x2.5 μm^2 close-up from (a) with a z-scale of 40 nm. The cross section indicated by a white line is displayed in the graph in (c).

5 Summary & Outlook

This thesis deals with the growth of organic Para-hexaphenyl (6P) thin-films on amorphous substrates, like SiO_2 and ion-bombarded muscovite mica. 6P is part of the family of rodlike π-conjugated oligophenyls. While on crystalline oriented surfaces 6P tends to build a thin film consisting of long needles of lying molecules, it forms mound-like structures of mostly upright standing molecules on amorphous substrates.The molecules were deposited by using physical vapor deposition in ultra-high vaccuum (UHV). The grown films were investigated with different atomic force microscopy (AFM) techniques – ex- and in-situ. The obtained AFM images were analyzed and interpreted applying concepts of epitaxy. The analysis was complemented by simple Monte Carlo simulations, empirical force field simulations, and molecular dynamics simulations.

As the formation of a stable nucleus is the starting point of epitaxial film growth, the first part of the thesis was dedicated to the determination of the critical nucleus size i^*, which defines the minimum number of molecules needed to perform a stable nucleus. At a size of $i^* + 1$ the nucleus is stable and proceeds growing. For the determination of i^* three different approaches were compared: a) evaluation of rate equations (RE) as proposed by Venables et al. [7], b) the analysis of the island-size distribution (ISD) as suggested by Amar and Family [18], c) analysis of the capture-zone distribution CZD introduced by Pimpinelli and Einstein [19, 20]. The analysis of 6P on ion-bombarded mica yielded an i^* between 1 and 3. 6P films on SiO_2 grown at room temperature (RT) resulted in an i^* between 0 and 2, whereas films on SiO_2 grown at 373 K revealed a drop of i^* to 1, which was explained by means of the thermodynamics in the early growth stage. These results for both substrates derived from CZD, ISD, and RE turned out to be in good agreement for all methods. But one needs to consider the difference in diffusion-limited aggregation (DLA) and attachment-limited aggregation (ALA) driven growth which yielded in higher values of i^* for both temperatures on SiO_2. Nevertheless, this work demonstrates that the relatively unknown CZD is even in organic film growth as powerful as the two other well-established approaches.

As SiO_2 is a technologically important substrate, compatible with common semiconductor technology, an additional focus was put on the influence of differently prepared SiO_2 substrates for 6P growth. The SiO_2 substrates were modified by etching with an O_2 plasma. 6P was grown on native and thermally grown SiO_2 and then both substrate types were treated by plasma before growth. The pristine native and thermal oxide surfaces yielded different nucleation densities indicating different densities of nucleation sites. On the plasma treated surfaces the nucleation density drastically increased. However, both substrates – native and thermally grown SiO_2 – provided similar numbers of nucleation sites after only 5 minutes of plasma treatment.

In addition 6P growth on differently annealed SiO_2 substrates was also investigated. AFM investigations revealed that different annealing temperatures and times yield in different island densities. The observed island densities increased steeply and approximately linear with annealing temperatures up to 373 K. Above 373 K the island density reduced roughly exponential with annealing temperature. This was explained by an annealing induced change in surface energy and roughness. Increasing of the annealing time lead to a similar results which is a sign of the same driving mechanism.

Further, the influence of increased substrate temperatures on the 6P growth morphology was investigated. At substrate temperatures from 285 K to 348 K, 6P formed rather compact islands, whereas an increase of substrate temperature to 423 K lead to the formation of more ramified structures. The observed evolution of the island density with substrate temperature indicates a growth mechanism via a so-called hot-precursor state [72]. It means that the molecules retain much of their kinetic energy which cannot dissipated when impinging on the surface. Owing to excited rotational and vibrational states, the molecules diffuse along the surface longer than expected until they become fully accommodated. At elevated substrate temperatures above 448 K, the islands vanished and 6P started to form high needle-like structures. At these high temperatures, the 6P molecules have enough energy to overcome the Ehrlich-Schwoebel barrier at the step edges.

Complementary experiments with different growth rates R, varying the temperature of the evaporator have been performed. The slope in the Arrhenius plot for R yields $\chi = 1.3 \pm 0.3$ for growth on SiO_2 which is comparable to $\chi = 1.4 \pm 0.1$ for ion-bombarded mica [135]. Interestingly, RE resulted in $i^* = -8$ for DLA and $i^* = 6$ for the ALA model. However, previous findings showed that the growth is mainly DLA dominated which stays in a contradiction with the results obtained here.

An additional observation was that upon venting, suddenly a large number of small islands occurred in between the free areas of the original first-layer 6P islands. This effect appeared on SiO_2 as well as on ion-bombarded mica substrates resulting in "bimodal" growth. While thermal desorption spectroscopy (TDS) revealed the evidence of a monomolecular wetting layer which remains on the surface between the grown big islands on ion-bombarded mica, the in-situ AFM imaged areas between the big islands without small islands on SiO_2. After venting, both substrates showed a similar bimodal growth behavior. It seems that water vapor in air plays a main role in co-adsorption as the driving force in the post-nucleation from the wetting layer.

Concerning growth, there raises a question: How is an organic thin film reacting, if it is annealed for a short time by heating the substrate after the growth. Annealing was performed between 383 K and 423 K for 5 to 10 minutes. Interestingly, the investigated thin films definitely showed that the islands began to shrink in the same way like they were growing before. So, if they were growing DLA-like then they were shrinking the same DLA-like, until they dissolved completely. Whereas there weren't any islands of upright standing molecules evident in AFM topography, the AFM phase image revealed that something still remained at the former area of the island. Kelvin probe force microscopy (KPFM) detected a change in the contact potential difference (CPD) based on a change in the work function of the surface within the former area of the island.

There are some experiments of inorganic growth deposited under a grazing incidence of $\alpha > 50°$ which show a change in growth morphology. The growth experiments are performed at deposition angles between 70° and 85°. The investigations disclose that there is a change in island size and island density depending on the position on the sample with respect to the distance to the evaporator. Caused by the tilt angle of the sample, there are lateral positions which are near or further away from the evaporator. Neither direct growth experiments nor corresponding Monte Carlo DLA simulations provided clear evidence for an influence on the island shape. An analysis of the fractal dimension of the grown islands yielded values between 1.3 and 1.6 and were in rough agreement with the Monte Carlo simulations which resulted in 1.66. Investigations with helium ion microscopy (HIM) shows with a higher resolution that the island edges look much more frayed than in AFM topographic images. This shows that obtaining the fractal dimension from an AFM image may mislead due to the lower resolution.

Finally, the shape of second-layer islands was studied. While the first-layer islands can have a shape ranging from very fractal to irregular compact, starting with the second-layer nucleation, every higher layer tends to form elongated hexagonal islands. AFM investigations for SiO_2 and ion-bombarded mica showed that within these hexagonal islands two values for the inner angles were preferable – $(104 \pm 2)^\circ$ and $(126 \pm 2)^\circ$. Using empirical force fields together with the herring bone structure of 6P in the bulk, simulations revealed the energetically preferable shape is an octagon. Based on this crystalline structure, molecular dynamics simulation of the edge diffusion of single 6P molecules was performed. This simulation reproduced well the preferential sticking of molecules at certain facets, which leads to the observed elongated hexagonal island shape. Whereas friction force microscopy (FFM) revealed no variations in the friction forces, transverse shear microscopy (TSM) demonstrated that first-layer islands can have different molecular orientation between each other, and that second-layer islands can have the same and even a complete different molecular orientation then their subjacent first layer. TSM revealed that there were second-layer islands situated on the same first layer having different molecular orientation with respect to each other and different to their first layer. Owing to the amorphous substrate, 6P first-layer islands are of irregular shape, but starting with a second layer, diffusing 6P molecules are forced by the molecular herringbone structure beneath to build islands similar to the equilibrium shape.

As an outlook the following remaining problems are listed:

To understand better the role of DLA and ALA in growth of 6P on SiO_2, more samples should be grown and analyzed by means of RE, ISD, and CZD like it was already shown for 6P and 5A on ion-bombarded mica [142]. Also, molecular dynamics simulations should be performed to find an explanation why this difference of i^* in DLA and ALA occurs.

According to the remnants of 6P islands after an annealing step, more investigations are needed to understand on the one hand what remains on the surface of the islands (cracking products of 6P or a surface modification which results in a local difference in surface energy) with e.g., Auger electron spectroscopy, HIM, or applying force-distance-curves with AFM. On the other hand, an explanation for the mechanism which stays behind this shrinking process needs to be performed. Thus, simulations using the model of “diffusion-limited annihilation” should be applied to this system of 6P on SiO_2 [149, 150].

The MD simulations dealing with incorporation and diffusion along island edges should be continued to clarify the origin of the second-layer islands with elongated hexagonal shape and why some second-layer islands show in TSM a different molecular orientation then other islands on the same terrace (whereas the molecular orientation of the terrace itself is homogeneous.)

Even if we know already a lot about 6P and its growth behavior, there is still something to discover as was recently presented for 6P growth on 2D materials [9, 151].

List of Figures

2.1 The different modes during thin-film growth in a schematic presentation: (a) Frank - van der Merwe, (b) Stranski - Krastanov, (c) Volmer - Weber for different coverage θ. 4

2.2 Schematic of the key processes during epitaxial growth (1 – adsorption, 2 – desorption from surface, 3 – adatom diffusion on surface, 4 – formation of dimers, trimers, or bigger clusters, 5 – decay of dimers or similarly small clusters, 6 – incorporation of particles into existing stable clusters or islands, 7 – detachment of particles from clusters or islands, 8 – edge diffusion, 9 – step-up jump, 10 – step-down hopping). 6

2.3 Dependency of the chemical potentials μ_V and μ_S on the pressure p. p_e indicates the equilibrium pressure. (Reproduced from Figure 1.2 on p.5 in [5]) 8

2.4 A particle descending from a step edge experiences an additional energy barrier E_ES – the Ehrlich-Schwoebel barrier. 9

2.5 (A) Energies associated with the transition path for diffusion of a rod-like molecule (exemplarily for a 6P molecule) over a step edge. Labels B to G correspond to situations illustrated in images (B) to (G) which are snapshots of the transition path. (Reproduced from [4]) 10

2.6 Dependency of the Gibbs free energy ΔG on the island radius r assuming the formation of a crystalline nucleus with a spherical shape from a supersaturated vapor phase. ΔG^* is the work of formation of the critical nucleus at radius r^*. (Reproduced from Figure 2.6 at p.25 in [17]) 11

2.7 Diagram of different stable island configurations for $i^* = 0$ to 3 which means that the supercritical cluster is then a monomer, dimer, trimer, tetramer, and so on. 12

2.8 Schematic illustration which shows the interaction between nucleation and growth states. The density n_1 determines the critical cluster size n_i in conjunction with the different losses which have characteristic times. n_x is the density of already stable clusters (from chap 5.2.3, p.153, Figure 5.5 in [6]). 13

2.9 Step-by-step generation of a Voronoi diagram from 5 vertices in 2D; left: first a bisector between p and q is formed (divided by dashed line); middle: Voronoi vertices $\mathrm{v_i}$ are established at the bisector intersections; right: bisector remnants are now the Voronoi edges between the Voronoi cells $\mathrm{vo(p_i)}$. (From [31]) 15

2.10 (a), (b) and (c) show the transition during thin-film growth of an island from fractal to a dendritic shape which finally ends up in a large compact island. (d) The two rows are examples what happens to the islands during coalescence. (Reproduced from investigations of growth done by Yang et al. [34]) 17

2.11 Schematic diagram of a simple DLA algorithm dated back to Figure 1 from [43]. It needs three zones (here shown as circles with radii r_b, r_{Start}, and $r_{\max}$). The diffusing particles are introduced at random points with the radius r_{Start} away from the center of the seed particle (green). The blue lines are probable random walks of the particles. In case 1, the particle reaches the aggregate (gray) which has a minimum bounding radius of r_b and sticks. In case 2, the particle reaches the external boundary (set at radius $r_{\max}$) and is rejected. Therefore a new particle will start at r_{Start}. . 19

2.12 Atom trajectories for a surface with a four-monolayer-high Al island by molecular dynamics simulation on a Ni(001) surface. The trajectory calculations were performed for an adatom incident angle of (a) $\alpha = 0°$ and (b) $\alpha = 60°$ each at 80 K with 0.1 eV (dashed line) and 6 eV (solid line) incident energy. (From [53]) 21

2.13 (a) Calculated equipotential energy contours and three atom trajectories (A,B,C) for a surface with a one-monolayer-high island on top of it for $\alpha = 80°$ which start at 20 Å above the surface. (b) The deposition rate at the surface calculated and normalized to a homogeneous flux far above the surface: (i) surface with a one-monolayer-high island and $\alpha = 80°$, (ii) with a one-monolayer-high island and normal-incidence deposition, and (iii) with a three-monolayer-high island and $\alpha = 80°$. (From [55]) (c) Energy and incidence angle dependence of the lateral difference in impact position for this case through steering. (From [57]) 22

2.14 Comparison of surface morphology for deposition of Cu on a Cu(100) surface along the [110] direction (top row) with that for deposition along the [100] direction (bottom row) at different deposition angles α and at $\theta = 50$ ML. Arrows illustrate each deposition direction. It shows that different α and azimuthal deposition directions can influence the metal-metal growth behavior. (From [61]) 23

2.15 Cu/Cu(001) surface morphology result from experiments (upper row, STM topographies) and kMC simulations (lower row) with $\theta = 40$ ML at $\alpha = 80°$ for different surface temperatures. The plane of incidence of the incoming atomic beam is indicated by the black arrow in between pictures and corresponds to the [110] azimuthal direction. The comparison shows a good correlation between experiment and simulation and reveal the influence of temperature. (From [62]) 23

2.16 (a) The chemical structure of 6P with its six phenyl rings in para arrangement. (b) The Van der Waals spheres shown the molecule in its gas phase with the tilt of phenyl rings out of their molecular plane. (c) The unit cell of a 6P crystal with its herring bone arrangement marked with some of its crystalline orientations [70, 71]. 25

2.17 The set of ARPES data presented as a contour map. The color scale is linear with highest intensity dark. It shows the binding energy (scaled to the Fermi level of the substrate) to the electron emission momentum (k_x). The density of states (DOS) is on the left with all orbitals enumerated. The Fourier spectra from the DFT-calculated orbitals of an isolated twisted 6P molecule are overlaid on the experimental band map (in turquoise). The corresponding molecule orbitals in real space are on the right (the LUMO structure is only implemented additionally). (Adapted from [74]) 26

2.18 6P nanofibers grown with OMBE under UHV conditions on mica. (a) AFM overview of the morphology of such a 6P film and (b) 3D representation of the same film from [8, 82, 83]. (c) Fluorescence micrograph of Para-hexaphenyl nanofibers deposited on (001)-oriented muscovite mica (from [67]). 26

2.19 (a) 3D representation of the mounded morphology of a 50 nm thick 6P film grown on amorphous SiO_2. (b) Height distribution obtained from a 4 nm thick 6P film on ion-bombarded mica(001). Inset: A sketch of the assumed gradual decreasing of the molecular tilt angle in the first few layers from up (nearly upright standing molecules) to down (more tilted molecules). (Adapted from [8]) 27

2.20 Lying 6P molecules between two electrodes can emit light like an OLED (left side). A film of upright standing 6P molecules connecting the source and drain electrodes can form an OFET. The amorphous substrate acts as gate dielectric. 27

2.21 (a) Comparison of crystalline and amorphous SiO_2 from [87] (b) Unit cell of crystalline SiO_2 and (c) Atomistic sketch of the silicon-silicon dioxide interface from [88]. (d) High-resolution transmission electron microscopy (HRTEM) observation at the bonding interface of hydrophilic Si–SiO_2 bonding from [89]. (e) Three-dimensional sketch of an amorphous tetrahedral network from [88]. 29

2.22 The crystal structure of muscovite mica; (a) a-axis projection; (b) cleaved surface (K^+ ions are not shown). AFM images of the cleaved (001) surface of muscovite mica taken in water. (c) 8 nm×8 nm; (d) 4 nm×4 nm. (Reproduced from [91]) 31

2.23 (a) Unit cell of BaF_2 (green: Ba^{2+} ions, light blue: F^- ions); (b) and (c) Topographic AFM images of $BaF_2(111)$ surfaces obtained by cleavage along the $[11\bar{2}]$ and $[\bar{1}10]$ directions (hollow arrows indicate the cleavage directions). (From [102]) 33

2.24 (a) Scheme of a general molecular beam epitaxy growth chamber (From [97]). (b) Schematic drawing of a typical Knudsen cell with a cross section of the main core interior (heater with crucible) adapted from [103]. 33

2.25 Graph of a Lennard-Jones potential describing the interaction between the tip atoms and the surface atoms which indicates the two working regimes for AFM. 34

2.26 (a) An electron microscopic image of the chip with the cantilever and the tip on it from [105]. (b) The schematic overview of a typical AFM system from [106]. 35

2.27 (a) The sketches show how the signal in FFM should be interpreted in case of moving over structures which differ in material (left) or in height (right) from [109]. (b) The schemes show how TSM works in principle. The arrows indicate in (a) and (b) the scanning directions (blue for trace and red for retrace). (Courtesy by Q. Shen) 37

2.28 Illustration of phase mode imaging in tapping mode. (a) The cantilever is lifted off the surface in non-contact mode and oscillating with "free" amplitude. (b) The cantilever is oscillating on surface 1 with a reduced amplitude and a small phase shift. During scanning from surface 1 to surface 2 a bigger phase shift occurs. This can be explained by differencies in tip-sample interaction which arise from variation in the adhesive forces and/or different mechanic response of the surface (from [112]). The inset shows an example for a change in amplitude and in frequency of the cantilever before and after contact with the surface where f_0 is the resonance frequency and Δf is the phase shift (from [113]). 39

2.29 Schematic overview of the KPFM measurement as a two-pass technique. (From [106]) 40

2.30 Schematic setting of a HIM. Inset: Scheme of the GFIS and the apex of the tip consisting of three tungsten atoms. (Reproduced from [119] and [118] 41

3.1 Evolution of temperature (red curve) and pressure (blue curve) with time during a typical growth experiment of 6P on SiO_2 at room temperature (RT). 45

3.2 (a) UHV system at the Institute of Physics, University of Leoben, used in this work (1...in-situ Omicron AFM, 2...growth chamber, 3...Quartz Crystal Balance with its water cooling tubes, 4a & 4b...two ion getter pumps, 5...turbo molecular pump, 6...six-way-cross, 7...power supply for the electron bombardment heater; load lock, evaporator and rotary vane pumps are in the rear and not visible on the image). (b) A detailed image of the evaporator containing the Knudsen-cell mounted to the UHV system (1...manipulator for the shutter, 2...connector for the thermocouple, 3...feedthroughs for the water cooling; the power connector is not visible on the image). 48

3.3 Reassembly of the evaporator after cleaning and refilling of the Knudsen-cell. (a) Phial with 6P powder, quartz glass crucible & thin metal net with holder made of tantalum. (b) Refilled crucible. (c) Crucible back in its position in the heater of the evaporator. (d) Evaporator without crucible and tantalum shield. (e) Reassembled evaporator with its tantalum shield. 48

3.4 (a) Old version of the home made heater with attached sample holder (ex-situ view). The white circle in the inset indicates where the molecular beam shadowing happens during growth at grazing incidence. (b) New version improved for growth at grazing incidence (view from inside of the growth chamber). 1...isolated cables of the thermocouple, 2...steel mounting with sample holder, 3...heater filament, 4...power cables for the filament, 5...evaporator's orifice closed by the shutter. 49

3.5 Sketch of the new version of the heater (blue) and the sample holder (grey) for growth at a grazing incidence ((a) front view, (b) back view). 50

3.6 Growth experiments with passive cooling by liquid nitrogen. (a) Dewar filled with liquid nitrogen in front of the UHV system. (b) Front view of the growth chamber with its lower part cooled from outside (1...manipulator of the heater; **u** and **d** indicate the approximate heater upper position during annealing & thin-film growth and lower position during sample transfer & passive cooling; white and black arrows indicate the vertical moving direction of the heater inside the growth chamber). (c) Rear view of the passive cooling system (blue arrows indicate the flow direction of the liquid nitrogen). 51

3.7 (a) Omicron AFM outside of the UHV system during a service maintenance (1...slot for the sample holder, 2...slot for the AFM probe holder, 3...magnetic damping system). (b) Digital Instruments Nanoscope IIIa Multimode AFM (1...optical microscope for LASER positioning, 2...scanner head, 3...AS-130 (J) piezo scanner with the sample on top). (c) Asylum Research MFP-3D AFM (1...scanner head with thumb wheels in front for engaging tip towards sample and on both sides for LASER adjustment, 2...scanner table, 3...AFM base, 4...air-damped table for undisturbed measurement). 53

4.1 (a) One of seven 20x20 μm^2 AFM images of a 6P submonolayer film grown at RT with a z-scale of 5 nm. (b) Original AFM image from (a) masked with the capture zones calculated from Voronoi tessellation. (c) 1x1 μm^2 AFM image from a single island of the same sample. (d) Corresponding height profile represented by the red line in (c). (From Lorbek et al. [129]) 59

4.2 (a) 85x85 μm^2 AFM image of a 6P submonolayer film grown at 373 K, z-scale 5 nm. (b) AFM image from (a) after processing with MATLAB masked with the capture zones calculated from Voronoi tessellation. (c) 10x10 μm^2 AFM image from a single island of the same sample. (d) Corresponding height profile represented by the red line in (c). (Adapted from Lorbek et al. [129]) 61

4.3 Upper row shows the (a) capture-zone and (b) island-size histograms obtained from the 6P film grown at RT on SiO_2. In both cases, a data set of about 2700 values were analyzed separately from each other by the model of Pimpinelli-Einstein [20] and Amar-Family [18]. The lower row shows the (c) capture-zone histogram obtained from 250 Voronoi-cells and (d) island-size histogram using 430 6P islands from the sample grown at 373 K on SiO_2 and their analysis with each model. The overlaid fits for several i^* were computed from the distribution functions of the two models for comparison. The dashed line is the best least square fit to the data of the histogram. The thick line marks the selected i^*. (Reproduced from Lorbek et al. [129]) 62

4.4 Calculations with a new β (expecting attachment-limited growth for 6P on SiO_2) yield new graphs for several i^* in case of (a) RT and (b) 373 K (compare Figure 4.3(a)&(c)). The capture-zone areas for the histograms are still the same. The dashed line is the best least square fit to the data of the histogram. The thick line marks the selected i^*. (From Lorbek unpublished) 65

4.5 (a) & (b) 6P islands on thermally grown SiO_2 without plasma etching. (c) & (d) 6P on thermally grown SiO_2 after plasma etching. (e) & (f) 6P on native SiO_2 without plasma etching. (g) & (h) 6P on native SiO_2 after plasma etching. (a),(c),(e) and (g) are 25 x 25 μm^2 AFM images. (b),(d),(f) and (h) are detailed 10 x 10 μm^2 views of (a),(c),(e) and (g). All AFM images have a z-scale of 4 nm. 67

4.6 10x10 μm^2 AFM images with a z-scale of 6 nm of samples grown at RT with a similar deposition rate $R = 0.035 \pm 0.006$ ML/min to reach the same coverage in average. (a) Sample grown without annealing procedure. The samples (b) to (h) were annealed with 1 kV electron bombardment before growth for 15 minutes at (b) 323 K, (c) 373 K, (d) 473 K, (e) 573 K, (f) 673 K, (g) 773 K, and (h) 1073 K. The lower row shows samples grown after an annealing with 20 V e^--bombardment and for 15 minutes at (i) 473 K, (j) 573 K, (k) 673 K, and (l) 773 K. 69

4.7 Graph with the island densities of SiO_2 samples which were annealed at different temperatures for 15 minutes. The first two values in orange at 300 K are plotted only for comparison, they were not annealed before growth of 6P. The samples in black are annealed at different temperatures with 1 kV electron bombardment. Triangular marks in red present the annealing at different temperature with 20 V electron bombardment. The sample with a green triangular mark was annealed with a standard procedure but stayed in the heater about 18 hours before growth. The sample marked in blue was annealed at 773 K without support by electron bombardment. The error bars covers approximately the size of the used symbols. The dashed dark blue line is a guide to the eye. 70

4.8 10x10 μm^2 AFM images with a z-scale of 6 nm of four 6P submonolayer thin-films on SiO$_2$ annealed at 773 K for 15 minutes and grown at RT. Samples presented in (a–c) were annealed with help of electron bombardment with (a) & (c) 1 kV and (b) 20 V, while (d) was heated without electron bombardment. (c) was not deposited immediately after cooling down, only after a stay in the heater of about 18 hours. 71

4.9 Graph with the island densities of SiO$_2$-samples which were annealed with different times at 773 K. The numbers below the symbols are mean values of the island density. The error bars cover approximately the size of the used symbols. Insets: exemplary 10x10 μm^2 AFM images with a z-scale of 6 nm for each annealing time. 73

4.10 Representative AFM images recorded from samples grown at different substrate temperatures as examples (with a z-scale of 6 nm). 10x10 μm^2 images of samples grown at (a) 285 K and (b) RT; (c) 25x25 μm^2 image of a sample grown at 343 K; (d) 30x30 μm^2 image of a sample grown at 348 K; (e) 60x60 μm^2 image of a sample grown at 373 K; 80x80 μm^2 images of samples grown at (f) 398 K, (g) 423 K and (h) 448 K; (i) 100x100 μm^2 image of a sample grown at 453 K. 75

4.11 Substrate temperature dependence of the island densities for various film/substrate 6P systems, taken from [27] and [135] supplemented with the results of 6P on SiO$_2$ (error bars present the standard deviation). 77

4.12 Scheme of the hyper-thermal diffusion of an impinging molecule during deposition up to the final thermal accommodation. (From [72].) 77

4.13 Upper row: 10x10 μm^2 AFM images of the film topography of samples grown at RT with different evaporation temperatures of the Knudsen-cell, (a) 503 K, (b) 513 K and (c) 523 K (each z-scale is 6 nm). (d) Plot of the island area size vs. deposition rate R (error bars present the standard deviation). (e) Plot of the ln(island density) vs. $\ln R$ added by a red line which is the linear fit through the sample data points with a slope of 1.3 ± 0.3. 79

4.14 AFM images with a z-scale of 6 nm of six different samples grown at three different substrate temperatures with an average coverage of 0.05 ML (left column) and 0.12 ML (right column). (a) and (b) are 30x30 μm^2 images grown at 348 K. (c) and (d) are 80x80 μm^2 images grown at 373 K. (e) and (f) are 40x40 μm^2 images grown at 423 K. 81

4.15 Island densities vs. substrate temperatures. Black marks represent the density of small islands and red marks represent the density of large islands for a coverage between 0.09 and 0.14 ML. At 432 K, the orange and gray marks stand for a coverage of 0.05 ML which are added for comparison. Error bars present the standard deviation of measured data. 82

4.16 Coverage dependence of small and large island density for 6P on SiO_2. The lines are guides to the eye. 83

4.17 In-situ and ex-situ AFM images 0.4 ML 6P on SiO_2 grown at 373 K. (a) 6x6 μm^2 image by Omicron AFM in UHV with a z-scale of 5 nm. (b) 30x30 μm^2 image of the same sample by ex-situ AFM under ambient conditions (z-scale 12 nm). 84

4.18 Left column displays the topographic images (25x25 μm^2 images with a z-scale of 6 nm) and right column the corresponding phase images (their z-scale is indicated by the false color rulers). Annealing procedure: (a) & (b) 403 K for 5 min, (c) & (d) 403 K for 10 min, (e) & (f) 413 K for 5 min, and (g) & (h) 423 K for 5 min. 86

4.19 (a) 10x10 μm^2 topographic AFM image with a z-scale of 6 nm displays the residual of a single island from the sample annealed at 403 K for 10 min. (b) phase mode image of (a) with the same size. (c) overlapped pictures of DLA-like NH_4Cl crystal growing in two-dimensional cell with randomly roughened surface from [145]. (d) 10x10 μm^2 topographic AFM image from (a) masked by the footprint of (b). Two height profiles are marked in (d) by a blue and a red line which are presented in (e) and (f). 88

4.20 (a) 20x20 μm^2 topographic AFM image with a z-scale of 6 nm of a sample annealed at 423 K for 5 min. The corresponding phase image is displayed in (b) and the CPD map of the area in (c) (both z-scales are indicated by false color rulers). 89

4.21 (a) 30x30 μm^2 AFM image of the topography with a z-scale of 6 nm taken from the sample annealed at 403 K for 5 min. (b) FFM image with a z-scale of 0.1 V and (c) TSM image with a z-scale of 18 mV of the topographic area shown in (a). (d) The height distribution over all islands of this sample. (All FFM and TSM images are courtesy by Q. Shen) . . . 90

4.22 (a) Sketch of the experiment for growth at grazing incidence: α is the tilt angle of the heater (black) with the sample holder (grey) plus sample (blue); the horizontal dashed black line marks the normal position of the heater (grey dashed lines symbolize the positions of the heater and the quartz crystal balance (QCB)); broad green arrow indicates the molecular beam direction. (b) Graph of the analysis of a first series of the growth at grazing incidence of $\alpha = 65°$ showing the coverage of three samples measured at three different sample positions. 92

4.23 Sketch of a silicon sample (triangular marks on the lower and the right edge are made for better orientation during ex-situ AFM measurements) with the chosen eleven lateral positions for measurements where “3.5” indicates the center of each sample location. Lower numbers down to “1” indicate positions left from the center which means these positions are closer to the evaporator and higher numbers up to “6” indicate positions right from the center which means these positions are further away from the evaporator. 93

4.24 Graph of every single coverage in monolayers vs. the lateral position of the measurement from each of the six samples shown in Figure 4.25 grown at an $\alpha = 75°$. The data points are connected by lines only to guide the eye. 94

4.25 AFM images of six samples grown at the same deposition angle of 75° arranged in a table. The six rows show AFM investigations of each sample at different lateral positions (indicated by numbers on top which are corresponding to the sketch in Figure 4.23). The rows are in ascending order towards their average coverage: #1 . . . $\theta_{\mathrm{av}} = 0.07 \pm 0.01$ ML, #2 . . . $\theta_{\mathrm{av}} = 0.17 \pm 0.02$ ML, #3 . . . $\theta_{\mathrm{av}} = 0.29 \pm 0.03$ ML, #4 . . . $\theta_{\mathrm{av}} = 0.49 \pm 0.07$ ML, #5 . . . $\theta_{\mathrm{av}} = 0.68 \pm 0.06$ ML, #6 . . . $\theta_{\mathrm{av}} = 0.98 \pm 0.15$ ML. (All images have a z-scale of 7 nm. The size of images from #1, #2, and #6 is 30x30 μm^2, while the others are 15x15 μm^2.) 95

4.26 AFM images tabularly arranged in four rows, starting with the biggest deposition angle of $\alpha = 85°$ down to 70°. The white numbers within center top of the images indicate their lateral position on the sample (after the sketch in Figure 4.23). The false color rulers at the right edge display the z-scale of the images in each row. The AFM images of the first row are 50x50 μm^2, while all others are 30x30 μm^2 in size. 96

4.27 Coverage vs. the lateral position of the AFM measurements for four different deposition angles α of 70°, 75°, 80° and 85°. The trend in coverage due to the lateral position is indicated by linear fits through all data points of the appropriate sample (only for $\alpha = 85°$ the first two data points are outliers and were not taken into account for the linear fit). 97

4.28 (a) 30x30 μm^2 AFM image with a z-scale of 7 nm from the center position of a sample (grown at RT with $\alpha = 75°$ and $\theta_{\mathrm{av}} = 0.06 \pm 0.01$ ML); 27 islands are masked in green which seem to be useful for fractal analysis; 11 out of these 27 are marked with numbers which were taken for the analysis. (b) Example of one single island: its image is split into two pictures (left – facing side, right – far side according to beam direction) which were investigated separately. (c) Results of each of the 11 islands: D_{fc} (in red) marks the fractal dimension calculated by varying the radius, D_{fb} (in blue) shows results from using classical box counting method, and D_{f}-fraclab (in green) indicates the estimated fractal dimension yielded from the software FracLab© (circles indicate the fractal dimension of the whole island and the triangles show the fractal dimension of each left and right side of the islands). 99

4.29 Representative simulation results and their calculated fractal dimension D_{f} of two series ofDLA simulation with different sticking coefficient k_s are displayed in two rows. While the upper row shows pictures with the expected shape of DLA growth with particles coming randomly from all sides, the lower row contains pictures where the particles were forced to arrive randomly only from the left side. 102

4.30 HIM images of two different single-layer 6P islands on silicon oxide, recorded with a primary energy of 20 keV and an He$^+$ ion dose of $3.21 \cdot 10^{15}$ cm^{-2}. (a) & (c) are images of the two islands and (b) & (c) are the corresponding backscattered helium images (While the island is visible in (b), there is nothing in (d) which is explained by a recording with a sample tilt of 10°). In (a) & (b) is a small second layer visible, marked by arrows. (From [147]) 103

4.31 (a) 1x1 μm^2 topographic AFM image of a 30 nm thick 6P film on ion-bombarded mica with a z-scale of 80 nm showing well-defined hexagonal steps. (b) Height profile along the cross section marked in (a). (c) 1x1 μm^2 AFM image with a z-scale of 50 nm showing the mounded surface of a 50 nm thick 6P film on SiO_2 with the corresponding cross section of a single mound in (d). (Adapted from [8]) 104

4.32 (a) 5x5 μm^2 AFM topographic image with a z-scale of 8 nm from the ion-bombarded mica sample. (b) Height profile of a cross section marked by a white line in (a). (c) Height distribution for the whole AFM image in (a). (d) Graph of a width-to-length-ratio analysis out of dozens of hexagonal-shaped-second-layer islands (D_{min}, D_{max}...width and length of the investigated islands; each aspect ratio was obtained from linear fit functions like the one in red). Inset displays exemplarily the width-to-length-ratio calculation marked in (a) by green (width) and blue (length) lines. 105

4.33 5x5 μm^2 AFM images of 6P on SiO_2 with a z-scale of 15 nm. (a) grown at RT with $\theta = 0.89$ ML and $R = 0.059$ ML/min, (b) grown at 313 K with $\theta = 1.08$ ML and $R = 0.072$ ML/min, (c) grown at 323 K with $\theta = 0.76$ ML and $R = 0.051$ ML/min, and (d) grown at 333 K with $\theta = 1.05$ ML and $R = 0.070$ ML/min. 106

4.34 Topographies of (a) a 1.6x1.6 μm^2 AFM image of 6P on mica and (b) a 2.5x2.5 μm^2 AFM image of 6P on SiO_2 (both with a z-scale of 10 nm) which show exemplarily how the measurement of the interior angles of the hexagonal islands took place (the island shape is marked in yellow together with each interior angles displayed). Histograms of interior angles from hundreds of hexagonal second-layer islands on (c) ion-bombarded mica and (d) SiO_2. 108

4.35 (a) Sketch of the most preferable shape of the hexagonal second-layer islands with the resulting two interior angles. (b) The possible facet orientations are shown in a 2D map with their angles in the ground plane(001) of the monoclinic unit cell from 6P [70]. (c) Simulations using empirical force-fields show for facet orientation [10] that the equilibrium shape of a 6P single crystal is octagonal (interior angles are in yellow and the expected angles of 104° are indicated with red arrows). (d) The equilibrium shape with single 6P molecules arranged in the typical herringbone structure shown with a slight molecular tilt of 17° towards the surface in y-direction. ((c) and (d) are a courtesy by D. Nabok) 109

4.36 Adsorption energy versus the path of a 6P molecule along three side edges marked with their facet directions obtained from the equilibrium crystal shape of Figure 4.35(c). The three different colors of the curve corresponds with the arrows indicating the path of a 6P molecule (marked in red) along the facet directions displayed in the inset. The different energies $E_{\text{diffusion}}$ of each diffusion barrier is added to the regarding facet. (Courtesy by G. Biddau) 110

4.37 (a) 10x10 μm^2 AFM image with a z-scale of 12 nm of the topography from a center position of the 6P film grown on ion-bombarded mica. Corresponding FFM image (b) with a z-scale of 1.2 V and TSM image (c) with a z-scale of 0.5 V from the region shown in (a). In (c) a blue circle marks three first-layer islands with different molecular orientation, a red circle marks different molecular orientation within one single first-layer island, white circles mark second-layer islands with same molecular orientation like their first-layer islands, and green circles mark second-layer islands with different molecular orientation than their first-layer islands. (Courtesy by Q. Shen) 111

4.38 5x5 μm^2 AFM topographic images with their corresponding TSM images of five different positions at the sample with 6P on ion-bombarded mica. (a) Topography with a z-scale of 10 nm and (b) its TSM image; (c) topography with a z-scale of 9 nm and (d) its TSM image; (e) Topography with a z-scale of 8 nm and (f) its TSM image; (g) topography with a z-scale of 10 nm and (h) its TSM image; (i) topography with a z-scale of 6 nm and (j) its TSM image. All TSM images have a z-scale of 1 mV. Blue circles in (h) and (j) indicate the rare case of different molecular orientations within single hexagonal second-layer islands. (Courtesy by Q. Shen) 112

4.39 (a) Screenshot of the video camera attached to the MFP-3D Asylum Research taken during the positioning of the LASER beam onto the cantilever which shows the surface of the transparent BaF$_2$ substrate. (b) 10x10 μm^2 AFM image of a 6P thin-film morphology on some terraces of the BaF$_2$ crystal with a z-scale of 60 nm ($\theta = 1.59$ ML). (c) Detailed AFM image of the 6P film on a single terrace of the BaF$_2$ crystal (5x5 μm^2 with a z-scale of 25 nm). (d) Graph of the cross section along the white line marked in (c). (e) Height distribution of the 6P thin film of (b) and (c). . 115

4.40 (a) 5x5 μm^2 AFM topographic image with a z-scale of 25 nm of a 6P film on BaF$_2$ with $\theta = 3.43$ ML. (b) A 2.5x2.5 μm^2 close-up from (a) with a z-scale of 40 nm. The cross section indicated by a white line is displayed in the graph in (c). 115

List of Tables

2.1 The constants C_{i^*} and a_{i^*}, for i = 1–6. 14

2.2 The constants a_β and b_β, for $\beta = 2$–7. 16

2.3 Fundamental properties of 6P [70–72] 24

3.1 List of used AFM probes (data from [1] www.nanoandmore.com and [2] www.ntmdt-tips.com) 54

4.1 List of all average values of the fractal dimension D_f obtained with three different kind of calculations (D_fc . . . fractal dimension calculated by varying the radius, D_fb . . . using classical box counting method, D_f-fraclab. . . using FracLab©). 100

4.2 Listed values of the average width-to-length ratio for the four investigated samples based on hundreds of hexagonal second-layer islands. 107

List of Publications

1. T. Potocar, **S. Lorbek**, D. Nabok, Q. Shen, L. Tumbek, G. Hlawacek, P. Puschnig, C. Ambrosch-Draxl, C. Teichert, and A. Winkler. "Initial stages of a para-hexaphenyl film growth on amorphous mica". *Phys. Rev. B*, 83:075423, 2011
2. **S. Lorbek**, G. Hlawacek, and C. Teichert. "Determination of critical island size in para-sexiphenyl islands on SiO_2 using capture-zone scaling". *Eur. Phys. J. Appl. Phys.*, 55(2):23902, 2011
3. G. Hlawacek, V. Veligura, **S. Lorbek**, T. F. Mocking, A. George, R. van Gastel, H. J. W. Zandvliet, and B. Poelsema. "Imaging ultra thin layers with helium ion microscopy: Utilizing the channeling contrast mechanism". *Beilstein J. Nanotechnol.*, 3:507–12, 2012
4. A. Neuhold, H. Brandner, S. J. Ausserlechner, **S. Lorbek**, M. Neuschitzer, E. Zojer, C. Teichert, and R. Resel. "X-ray based tools for the investigation of buried interfaces in organic electronic devices". *Org. Electron.*, 14(2):479–487, 2013
5. B. Galiana, M. Benedicto, L. Dez-Merino, **S. Lorbek**, G. Hlawacek, C. Teichert, and P. Tejedor. "Modified energetics and growth kinetics on H-terminated GaAs(110)". *J. Chem. Phys.*, 139(16):164712, 2013

Bibliography

[1] H. Sitter, W. Kern, G. Trimmel, M. G. Ramsey, C. Teichert, R. Resel, D. Meissner, N. S. Sariciftci, S. Bauer, R. Hagelauer, T. Ostermann, and C. Ambrosch-Draxl. "Interface Controlled And Functionalised Organic Films: Functional Organics – Final Report". Technical report, National Research Network, Austria, 2006–2012.

[2] A. J. Fleming, S. Berkebile, T. Ules, and M. G. Ramsey. "Pre-nucleation dynamics of organic molecule self-assembly investigated by PEEM". *Phys. Chem. Chem. Phys.*, 13:4693–4708, 2011.

[3] G. Hlawacek, F. S. Khokhar, R. van Gastel, B. Poelsema, and C. Teichert. "Smooth Growth of Organic Semiconductor Films on Graphene for High-Efficiency Electronics". *Nano Lett.*, 11(2):333–337, 2011. PMID: 21207968.

[4] G. Hlawacek, P. Puschnig, P. Frank, A. Winkler, C. Ambrosch-Draxl, and C. Teichert. "Characterization of Step-Edge Barriers in Organic Thin-Film Growth". *Science*, 321(5885):108–111, 2008.

[5] I. V. Markov. *"Crystal growth for beginners: fundamentals of nucleation, crystal growth and epitaxy"*. World Scientific Publishing Co. Pte. Ltd. Singapore, 2nd edition, 2004.

[6] J. A. Venables. *"Introduction to Surface and Thin Film Processes"*. Cambridge University Press, Cambridge UK, 2003.

[7] J. A. Venables, G. D. T. Spiller, and M. Hanbücken. "Nucleation and growth of thin films". *Rep. Prog. Phys.*, 47:399–459, 1984.

[8] G. Hlawacek. *"Molecular growth mechanisms in para-sexiphenyl thin film deposition"*. PhD thesis, Montanuniversitaet Leoben, 2007.

[9] M. Kratzer, A. Matkovic, and C. Teichert. “Adsorption and epitaxial growth of small organic semiconductors on hexagonal boron nitride”. *J. Phys. D: Appl. Phys.*, 52(38):383001, 2019.

[10] A. Matković, M. Kratzer, B. Kaufmann, J. Vujin, R. Gajić, and C. Teichert. “Probing charge transfer between molecular semiconductors and graphene”. *Sci. Rep.*, 7(1):9544, 2017.

[11] A. Matković, A. Petritz, G. Schider, M. Krammer, M. Kratzer, E. Karner-Petritz, A. Fian, H. Gold, M. Gärtner, A. Terfort, C. Teichert, E. Zojer, K. Zojer, and B. Stadlober. “Interfacial Band Engineering of MoS_2/Gold Interfaces Using Pyrimidine-Containing Self-Assembled Monolayers: Toward Contact-Resistance-Free Bottom-Contacts”. *Adv. Electron. Mater.*, 6(5):2000110, 2020.

[12] J. W. Evans, P. A. Thiel, and M. Li. “Kinetic Monte Carlo Simulation of Epitaxial Thin Film Growth: Formation of Submonolayer Islands and Multilayer Mounds”. In *Chemistry Conference Papers, Posters and Presentations*, 2007.

[13] M. L. Klein and J. A. Venables, editors. *“Rare Gas Solids”*, volume 1. Academic Press New York, 1976.

[14] W. K. Burton, N. Cabrera, and F. C. Frank. “The growth of crystals and the equilibrium structure of their surfaces”. *Philosophical Transactions of the Royal Society of London, Series A*, 243(866):299–358, 1951.

[15] G. Ehrlich and F. G. Hudda. “Atomic view of surface self-diffusion: Tungsten on tungsten”. *J. Chem. Phys.*, 44(3):1039–1049, 1966.

[16] R. L. Schwoebel and E. J. Shipsey. “Step motion on crystal surfaces”. *J. Appl. Phys.*, 37(10):3682–3686, 1966.

[17] G. Dhanaraj, K. Byrappa, V. Prasad, and M. Dudley, editors. *“Springer Handbook of Crystal Growth”*. Springer-Verlag Berlin Heidelberg, 1st edition, 2010.

[18] J. G. Amar and F. Family. “Critical cluster size: Island morphology and size distribution in submonolayer epitaxial growth”. *Phys. Rev. Lett.*, 74(11):2066–2069, 1995.

[19] A. Pimpinelli and T. L. Einstein. “Capture-zone scaling in island nucleation: Universal fluctuation behavior”. *Phys. Rev. Lett.*, 99(22):226102, 2007.

[20] A. Pimpinelli and T. L. Einstein. “Reply to M. Li, Y. Han, and J. W. Evans, preceding Comment, Phys. Rev. Lett. 104, 149601 (2010)”. *Phys. Rev. Lett.*, 104:149602, 2010.

[21] J. A. Venables. “Rate equation approaches to thin film nucleation kinetics”. *The Philosophical Magazine: A Journal of Theoretical Experimental and Applied Physics*, 27(3):697–738, 1973.

[22] J. A. Venables. “Nucleation calculations in a pair-binding model”. *Phys. Rev. B*, 36:4153–4162, 1987.

[23] C. Ratsch and J. A. Venables. “Nucleation theory and the early stages of thin film growth”. *J. Vac. Sci. Technol., A*, 21(5):S96–S109, 2003.

[24] J. Krug. “Four lectures on the physics of crystal growth”. *Physica A*, 313(1):47 – 82, 2002.

[25] J. G. Amar, F. Family, and P.-M. Lam. “Dynamic scaling of the island-size distribution and percolation in a model of submonolayer molecular-beam epitaxy”. *Phys. Rev. B*, 50(12):8781–8797, 1994.

[26] R. Ruiz, B. Nickel, N. Koch, L .C. Feldman, R.F. Haglund Jr., A. Kahn, F. Family, and G. Scoles. “Dynamic Scaling, Island Size Distribution, and Morphology in the Aggregation Regime of Submonolayer Pentacene Films”. *Phys. Rev. Lett.*, 91(13):1361021–1361024, 2003.

[27] T. Potocar, S. Lorbek, D. Nabok, Q. Shen, L. Tumbek, G. Hlawacek, P. Puschnig, C. Ambrosch-Draxl, C. Teichert, and A. Winkler. “Initial stages of a para-hexaphenyl film growth on amorphous mica”. *Phys. Rev. B*, 83:075423, 2011.

[28] P. A. Mulheran and J. A. Blackman. “The origins of island size scaling in heterogeneous film growth”. *Philos. Mag. Lett.*, 72(1):55–60, 1995.

[29] J. A. Blackman and P. A. Mulheran. “Scaling behavior in submonolayer film growth: A one-dimensional model”. *Phys. Rev. B: Condens. Matter Mater. Phys.*, 54(16):11681–11692, 1996.

[30] M. Brinkmann, S. Graff, and F. Biscarini. “Mechanism of nonrandom pattern formation of polar-conjugated molecules in a partial wetting regime”. *Phys. Rev. B: Condens. Matter Mater. Phys.*, 66(16):1654301–1654308, 2002.

[31] H. Zimmer. “Voronoi and Delaunay techniques”. In *Lecture Notes in Computer Science VIII*, 2005.

[32] F. Shi, Y. Shim, and J. G. Amar. “Capture-zone areas in submonolayer nucleation: Effects of dimensionality and short-range interactions”. *Phys. Rev. E*, 79:011602, 2009.

[33] M. Li, Y. Han, and J. W. Evans. “Comment on Pimpinelli, A. and Einstein, T. L., Phys. Rev. Lett. 99, 226102 (2007)”. *Phys. Rev. Lett.*, 104:149601, 2010.

[34] J. Yang, T. Wang, H. Wang, F. Zhu, G. Li, and D. Yan. “Ultrathin-film growth of para-sexiphenyl (II): Formation of large-size domain and continuous thin film”. *J. Phys. Chem. B*, 112(26):7821–7825, 2008.

[35] D. Kandel. “Initial Stages of Thin Film Growth in the Presence of Island-Edge Barriers”. *Phys. Rev. Lett.*, 78:499–502, 1997.

[36] A. Pimpinelli, L. Tumbek, and A. Winkler. “Scaling and Exponent Equalities in Island Nucleation: Novel Results and Application to Organic Films”. *J. Phys. Chem. Lett.*, 5(6):995–998, 2014.

[37] T. A. Witten and L. M. Sander. “Diffusion-Limited Aggregation, a Kinetic Critical Phenomenon”. *Phys. Rev. Lett.*, 47:1400–1403, 1981.

[38] P. Meakin. “Formation of Fractal Clusters and Networks by Irreversible Diffusion-Limited Aggregation”. *Phys. Rev. Lett.*, 51:1119–1122, 1983.

[39] P. Meakin. “Diffusion-controlled cluster formation in two, three, and four dimensions”. *Phys. Rev. A*, 27:604–607, 1983.

[40] P. Meakin. “Diffusion-controlled cluster formation in 2–6-dimensional space”. *Phys. Rev. A*, 27:1495–1507, 1983.

[41] M. Kolb, R. Botet, and R. Jullien. “Scaling of Kinetically Growing Clusters”. *Phys. Rev. Lett.*, 51:1123–1126, 1983.

[42] T. Vicsek. *“Fractal Growth Phenomena”*. World Scientific Publishing Co. Pte. Ltd. Singapore, 1st edition, 1989.

[43] P. Meakin, S. Tolman, and A. Blumen. “Diffusion-Limited Aggregation [and Discussion]”. *Proceedings of the Royal Society of London. Series A, Mathematical and Physical Sciences*, 423(1864):133–148, 1989.

[44] M. Batty, P. Longley, and S. Fotheringham. “Urban Growth and Form: Scaling, Fractal Geometry, and Diffusion-Limited Aggregation”. *Environment and Planning A: Economy and Space*, 21(11):1447–1472, 1989.

[45] C. Teichert, C. Ammer, and M. Klaua. “Step formation on the ion-bombarded Ag(100) surface studied by LEED and Monte Carlo simulations”. *Phys. Status Solidi A*, 146(1):223–242, 1994.

[46] F. Hausdorff. “Dimension und äußeres Maß”. *Math. Annalen*, 79:157–179, 1919.

[47] S. Lalley and D. Gatzouras. “Hausdorff and box dimensions of certain self-affine fractals”. *Indiana University Mathematics Journal*, 41:533–568, 1992.

[48] K. Falconer. *“Fractal geometry : mathematical foundations and applications”*. John Wiley & Sons Chichester UK, 1990.

[49] M. V. Berry. “Diffractals”. *J. Phys. A: Math. Gen.*, 12(6):781, 1979.

[50] N. J. Shevchik. “Growth instabilities in the deposition of amorphous films”. *J. Non-Cryst. Solids*, 12(2):141 – 149, 1973.

[51] M. Raible, S. J. Linz, and P. Hänggi. “Amorphous thin film growth: Minimal deposition equation”. *Phys. Rev. E*, 62:1691–1705, 2000.

[52] S. J. Linz, M. Raible, and P. Hänggi. *Advances in Solid State Physics*, chapter “Amorphous Thin Film Growth: Modeling and Pattern Formation”, pages 391–403. Springer Berlin Heidelberg, 2001.

[53] S. Lee and Y. Chung. “The Incident Angle Effect of Al Adatom on the Growth Morphology of Al/Ni(001) System: Molecular Dynamics Simulation”. In *IEEE International Magnetics Conference (INTERMAG)*, volume 42, pages 2939–2941, San Diego, California, 2006. IEEE.

[54] S. van Dijken, L. C. Jorritsma, and B. Poelsema. “Steering-Enhanced Roughening during Metal Deposition at Grazing Incidence”. *Phys. Rev. Lett.*, 82:4038–4041, 1999.

[55] S. van Dijken, L. C. Jorritsma, and B. Poelsema. “Grazing-incidence metal deposition: Pattern formation and slope selection”. *Phys. Rev. B*, 61:14047–14058, 2000.

[56] A. Farahzadi, P. Niyamakom, M. Beigmohamadi, N. Meyer, D. Keiper, M. Heuken, F. Ghasemi, M. R. Rahimi Tabar, T. Michely, and M. Wuttig. “Stochastic analysis on temperature-dependent roughening of amorphous organic films”. *Europhys. Lett.*, 90(1):10008, 2010.

[57] H. Wormeester and B. Poelsema. “Flux heterogeneity through incidence angle and particle energy in steering-enhanced growth”. *Phys. Rev. B*, 66:165406, 2002.

[58] P. Politi and C. Castellano. “Irreversible nucleation in molecular beam epitaxy: From theory to experiments”. *Phys. Rev. B*, 67:075408, 2003.

[59] J. Seo, H.-Y. Kim, and J.-S. Kim. “Steering effects on growth instability during step-flow growth of Cu on Cu$(1, 1, 17)$”. *Phys. Rev. B*, 71:075414, 2005.

[60] J. Seo, H.-Y. Kim, and J.-S. Kim. “Effects of deposition dynamics on epitaxial growth”. *J. Phys.: Condens. Matter*, 19(48):486001, 2007.

[61] Y. Shim, V. Borovikov, and J. G. Amar. “Effects of shadowing and steering in oblique-incidence metal (100) epitaxial growth”. *Phys. Rev. B*, 77:235423, 2008.

[62] F. L. W. Rabbering, G. Stoian, R. van Gastel, H. Wormeester, and B. Poelsema. “Oblique incidence deposition of Cu/Cu(001): Enhanced roughness and ripple formation”. *Phys. Rev. B*, 81:115425, 2010.

[63] H. Yanagi, S. Okamoto, and T. Mikami. “Organic electroluminescent device with epitaxial p-sexiphenyl films”. *Synth. Met.*, 91(1):91 – 93, 1997.

[64] H. Yanagi and S. Okamoto. “Orientation-controlled organic electroluminescence of p-sexiphenyl films”. *Appl. Phys. Lett.*, 71:2563–2565, 1997.

[65] H. Yanagi and T. Morikawa. “Self-waveguided blue light emission in p-sexiphenyl crystals epitaxially grown by mask-shadowing vapor deposition”. *Appl. Phys. Lett.*, 75(2):187–189, 1999.

[66] A. Andreev, F. Quochi, F. Cordella, A. Mura, G. Bongiovanni, H. Sitter, G. Hlawacek, C. Teichert, and N.S. Sariciftci. “Coherent random lasing in the

deep blue from self-assembled organic nanofibers". *J. Appl. Phys.*, 99(3):034305, 2006.

[67] F. Quochi, F. Cordella, A. Mura, G. Bongiovanni, F. Balzer, and H.-G. Rubahn. "Gain amplification and lasing properties of individual organic nanofibers". *Appl. Phys. Lett.*, 88(4):041106, 2006.

[68] H. Yanagi, K. Tamura, Y. Tanaka, and F. Sasaki. "Optically pumped lasing from single-crystal cavity of p-phenylene oligomer". *Adv. Nat. Sci.: Nanosci. Nanotechnol.*, 5(4):045013, 2014.

[69] S. Guha, W. Graupner, R. Resel, M. Chandrasekhar, H. R. Chandrasekhar, R. Glaser, and G. Leising. "Planarity of para Hexaphenyl". *Phys. Rev. Lett.*, 82:3625–3628, 1999.

[70] K. N. Baker, H. C. Knachel, A. V. Fratini, and W. W. Adams. "Structural Transformations in Crystalline Oligomers of Polyparaphenylene". *MRS Proceedings*, 134:497, 1988.

[71] K. N. Baker, A. V. Fratini, T. Resch, H. C. Knachel, W. W. Adams, E. P. Socci, and B. L. Farmer. "Crystal structures, phase transitions and energy calculations of poly(p-phenylene) oligomers". *Polymer*, 34(8):1571 – 1587, 1993.

[72] A. Winkler. "Kinetics of Ultra-Thin Organic Film Growth". In K. Wandelt, editor, *Encyclopedia of Interfacial Chemistry*, pages 195 – 215. Elsevier, Oxford, 2018.

[73] T. Birendra Singh, G. Hernandez-Sosa, H. Neugebauer, A. Andreev, H. Sitter, and N. S. Sariciftci. "Electrical transport properties of hot wall epitaxially grown para -sexiphenyl nano-needles". *Phys. Status Solidi B*, 243(13):3329–3332, 2006.

[74] G. Koller, S. Berkebile, M. Oehzelt, P. Puschnig, C. Ambrosch-Draxl, F. P. Netzer, and M. G. Ramsey. "Intra- and Intermolecular Band Dispersion in an Organic Crystal". *Science*, 317(5836):351–355, 2007.

[75] S. Müllegger and A. Winkler. "Hexaphenyl thin films on clean and carbon covered Au(111) studied with TDS and LEED". *Surf. Sci.*, 600(6):1290 – 1299, 2006.

[76] R. Resel, K. Erlacher, B. Müller, A. Thierry, B. Lotz, T. Kuhlmann, K. Lischka, and G. Leising. "Molecular beam epitaxy of p-hexaphenyl on GaAs(111)". *Surf. Interface Anal.*, 30(1):518–521, 2000.

[77] B. Winter, J. Ivanco, F. P. Netzer, and M. G. Ramsey. "Ordered mono- and multilayer films of sexiphenyl on Al(111): a LEED investigation". *Thin Solid Films*, 433(1):269 – 273, 2003.

[78] Y. Hu, K. Maschek, L. D. Sun, M. Hohage, and P. Zeppenfeld. "para-Sexiphenyl thin film growth on Cu(110) and Cu(110)–(2×1)O surfaces". *Surf. Sci.*, 600(3):762 – 769, 2006.

[79] P. Frank and A. Winkler. "Tailoring the film morphology of para-hexaphenyl on KCl(001) by surface temperature". *Appl. Phys. A*, 90(4):717–721, 2008.

[80] M. Wagner, J. Hofinger, M. Setvín, L. A. Boatner, M. Schmid, and U. Diebold. "Prototypical Organic–Oxide Interface: Intramolecular Resolution of Sexiphenyl on In_2O_3(111)". *ACS Applied Materials and Interfaces*, 10(16):14175–14182, 2018.

[81] R. Resel, N. Koch, F. Meghdadi, G. Leising, W. Unzog, and K. Reichmann. "Growth and preferred crystallographic orientation of hexaphenyl thin films". *Thin Solid Films*, 305(1):232 – 242, 1997.

[82] A. Andreev, G. Matt, C. J. Brabec, H. Sitter, D. Badt, H. Seyringer, and N. S. Sariciftci. "Highly Anisotropically Self-Assembled Structures of para-Sexiphenyl Grown by Hot-Wall Epitaxy". *Adv. Mater.*, 12:629–633, 2000.

[83] C. Teichert, G. Hlawacek, A. Y. Andreev, H. Sitter, P. Frank, A. Winkler, and N. S. Sariciftci. "Spontaneous rearrangement of para-sexiphenyl crystallites into nano-fibers". *Appl. Phys. A*, 82:665–669, 2006.

[84] E. Wiberg and N. Wiberg. *"Holleman-Wiberg: Lehrbuch der Anorganischen Chemie"*. Walter de Gruyter & Co. Berlin New York, 102nd edition, 1995.

[85] S. K. Ghandhi. *"VLSI Fabrication Principles: Silicon and Gallium Arsenide"*. John Wiley & Sons New York, 2nd edition, 1994.

[86] A. Hössinger. *"Simulation of Ion Implantation for ULSI Technology"*. PhD thesis, Technischen Universität Wien, Fakultät für Elektrotechnik, 2000.

[87] NDT Education Resource Center, The Collaboration for NDT Education, Iowa State University. "Solid State Structure". `https://www.nde-ed.org/EducationResources/CommunityCollege/Materials/Structure/solidstate.htm`, last viewed 03/01/2021.

[88] J. D. Plummer, M. Deal, and P. D. Griffin. *"Silicon VLSI Technology: Fundamentals, Practice, and Modeling"*. Pearson London, US Ed Edition, 2001.

[89] H. Moriceau, F. Rieutord, F. Fournel, Y. Le Tiec, L. Di Cioccio, C. Morales, A. M. Charvet, and C. Deguet. "Overview of recent direct wafer bonding advances and applications". *Adv. Nat. Sci.: Nanosci. Nanotechnol.*, 1(4):043004, 2011.

[90] T. Potocar. "Nucleation and layer growth of para-hexaphenyl on sputtered mica(001)". Master's thesis, Graz University of Technology, 2010.

[91] T. Fukuma, K. Kobayashi, K. Matsushige, and H. Yamada. "True atomic resolution in liquid by frequency-modulation atomic force microscopy". *Appl. Phys. Lett.*, 87(3):034101, 2005.

[92] J. R. Arthur. "Interaction of Ga and As_2 Molecular Beams with GaAs Surfaces". *J. Appl. Phys.*, 39(8):4032–4034, 1968.

[93] A. Y. Cho and J. R. Arthur. "Molecular beam epitaxy". *Prog. Solid State Chem.*, 10:157 – 191, 1975.

[94] M. A. Herman and H. Sitter. *"Molecular Beam Epitaxy"*. Springer-Verlag Berlin, 1996.

[95] G. Biasiol and L. Sorba. "MOLECULAR BEAM EPITAXY: PRINCIPLES AND APPLICATIONS". In R. Fornari and L. Sorba, editors, *Crystal growth of materials for energy production and energy-saving applications*, pages 66–83. Edizioni ETS, Pisa, 2001.

[96] J. R. Arthur. "Molecular beam epitaxy". *Surf. Sci.*, 500(1):189 – 217, 2002.

[97] L. Morresi. *Silicon Based Thin Film Solar Cells*, chapter "Chapter4: Molecular Beam Epitaxy (MBE)", pages 81–107. Bentham Science Publishers, 2013.

[98] J. A. Hagen, W.-X. Li, H. Spaeth, J. G. Grote, and A. J. Steckl. "Molecular Beam Deposition of DNA Nanometer Films". *Nano Lett.*, 7(1):133–137, 2007.

[99] M. Knudsen. "Die Gesetze der Molekularströmung und der inneren Reibungsströmung der Gase durch Röhren". *Ann. Phys.*, 333(1):75–130, 1909.

[100] M. Knudsen. "Die Molekularströmung der Gase durch Öffnungen und die Effusion". *Ann. Phys.*, 333(5):999–1016, 1909.

[101] M. Knudsen. “Experimentelle Bestimmung des Druckes gesättigter Quecksilberdämpfe bei 0° und höheren Temperaturen”. *Ann. Phys.*, 334(6):179–193, 1909.

[102] M. Cardellach, A. Verdaguer, J. Santiso, and J. Fraxedas. “Two-dimensional wetting: The role of atomic steps on the nucleation of thin water films on BaF2(111) at ambient conditions”. *J. Chem. Phys.*, 132(23):234708, 2010.

[103] CreaTec Fischer & Co. GmbH. “Folder: Evaporators”, 2017. `https://createc.de/Evaporators/`, last viewed 03/01/2021.

[104] G. Binnig, C. F. Quate, and C. Gerber. “Atomic force microscope”. *Phys. Rev. Lett.*, 56(9):930–3, 1986.

[105] Nu Nano Ltd. “Components of an AFM probe”. `https://www.nunano.com/blog/2016/12/12/a-pedants-christmas-guide-to-afm-probe-terminology`, last viewed 03/01/2021.

[106] V. L. Mironov. *“Fundamentals of scanning probe microscopy”*. The Russian Acedemy of Science, Instutute for Physics and Microstructures, Nizhniy Novgorod, Russia, 2004.

[107] C. M. Mate, G. M. McClelland, R. Erlandsson, and S. Chiang. “Atomic-Scale Friction of a Tungsten Tip on a Graphite Surface”. *Phys. Rev. Lett.*, 59:1942–1945, 1987.

[108] G. Meyer and N. M. Amer. “Simultaneous measurement of lateral and normal forces with an optical-beam-deflection atomic force microscope”. *Appl. Phys. Lett.*, 57:2089–2091, 1990.

[109] Nanosurf AG. “Contact Modes”. `https://www.nanosurf.com/en/support/afm-modes-overview/contact-modes`, last viewed 03/01/2021.

[110] K. Puntambekar, J. Dong, G. Haugstad, and C. D. Frisbie. “Structural and electrostatic complexity at a pentacenc/insulator interface”. *Adv. Funct. Mater.*, 16(7):879–884, 2006.

[111] S. N. Magonov, V. Elings, and M.-H. Whangbo. “Phase imaging and stiffness in tapping-mode atomic force microscopy”. *Surf. Sci.*, 375(2):L385 – L391, 1997.

[112] J. P. Pineda, B. Kim, and K. Lee. “Phase Imaging of Polymer Deposited on Gold”. In *NanoScientific*, volume 19, pages 24–26. Park Systems Inc., Santa Clara, CA, USA, 2020.

[113] Bruker Nano Surfaces. “Fundamentals of Contact Mode and TappingMode Atomic Force Microscopy”, AZoNano. `https://www.azonano.com/article.aspx?ArticleID=3010`, last viewed 03/01/2021.

[114] M. Nonnenmacher, M. P. O’Boyle, and H. K. Wickramasinghe. “Kelvin probe force microscopy”. *Appl. Phys. Lett.*, 58(25):2921–2923, 1991.

[115] S. Sadewasser and T. Glatzel, editors. *“Kelvin Probe Force Microscopy”*, volume 65 of *Springer Series in Surface Sciences.* Springer-Verlag Berlin Heidelberg, 2018.

[116] I. Beinik. *“Electrical Characterization of Semiconductor Nanostructures by Conductive Probe Based Atomic Force Microscopy Techniques”.* PhD thesis, Montanuniversitaet Leoben, 2011.

[117] G. Hlawacek and A. Gölzhäuser. *“Helium Ion Microscopy”.* NanoScience and Technology. Springer International Publishing AG Switzerland, 2018.

[118] G. Hlawacek, V. Veligura, R. van Gastel, and B. Poelsema. ”Helium ion microscopy”. *J. Vac. Sci. Technol., B*, 32(2):020801, 2014.

[119] V. N. Bliznyuk, D. LaJeunesse, and A. Boseman. “Application of helium ion microscopy to nanostructured polymer materials”. *Nanotechnology Reviews*, 3(4):361 – 387, 2014.

[120] P. Klapetek, D. Necas, and C. Anderson. “Gwyddion user guide”, 2020. `http://gwyddion.net/documentation/`, last viewed 03/01/2021.

[121] I. Vasilief. “The QtiPlot Handbook”, 2020. `https://www.qtiplot.com/doc/manual-en/index.html`, last viewed 03/01/2021.

[122] The MathWorks, Inc. MATLAB. `https://de.mathworks.com/help/matlab/index.html`, last viewed 03/01/2021.

[123] INRIA, Saclay. “fraclab 2.2”. `https://project.inria.fr/fraclab/`, last viewed 03/01/2021.

[124] J. W. Eaton. “GNU Octave (version 6.1.0)”. `https://octave.org/doc/v6.1.0/`, last viewed 03/01/2021.

[125] P. J. Turner and Grace Development Team. “Grace User’s Guide (for Grace-5.1.22)”, 2008. `https://plasma-gate.weizmann.ac.il/Grace/doc/UsersGuide.html`, last viewed 03/01/2021.

[126] T. Michely and J. Krug. *“Islands, Mounds and Atoms”*, volume 42 of *Springer Series in Surface Science.* Springer-Verlag Berlin Heidelberg, Berlin, Heidelberg, 1st edition, 2004.

[127] D. W. Scott. “On Optimal and Data-Based Histograms”. *Biometrika*, 66(3):605–610, 1979.

[128] K. Knuth. “Optimal Data-Based Binning for Histograms”. *arXiv:physics/0605197v2*, 2006.

[129] S. Lorbek, G. Hlawacek, and C. Teichert. “Determination of critical island size in para-sexiphenyl islands on SiO_2 using capture-zone scaling”. *Eur. Phys. J. Appl. Phys.*, 55(2):23902, 2011.

[130] J. Yang, T. Wang, H. Wang, F. Zhu, G. Li, and D. Yan. “Ultrathin-film growth of para-sexiphenyl (I): Submonolayer thin-film growth as a function of the substrate temperature”. *J. Phys. Chem. B*, 112(26):7816–7820, 2008.

[131] G. Rosenfeld, R. Servaty, C. Teichert, B. Poelsema, and G. Comsa. “Layer-by-layer growth of Ag on Ag(111) induced by enhanced nucleation: A model study for surfactant-mediated growth”. *Phys. Rev. Lett.*, 71:895–898, 1993.

[132] D. D. Chambliss and K. E. Johnson. “Nucleation with a critical cluster size of zero: Submonolayer Fe inclusions in Cu(100)”. *Phys. Rev. B*, 50:5012–5015, 1994.

[133] P. A. Mulheran and J. A. Blackman. “Capture zones and scaling in homogeneous thin-film growth”. *Phys. Rev. B*, 53(15):10261–10267, 1996.

[134] M. N. Popescu, J. G. Amar, and F. Family. “Rate-equation approach to island size distributions and capture numbers in submonolayer irreversible growth”. *Phys. Rev. B*, 64:205404, 2001.

[135] L. Tumbek and A. Winkler. "Attachment limited versus diffusion limited nucleation of organic molecules: Hexaphenyl on sputter-modified mica". *Surf. Sci.*, 606(15):L55 – L58, 2012.

[136] J. A. Venables and H. Brune. "Capture numbers in the presence of repulsive adsorbate interactions". *Phys. Rev. B*, 66:195404, 2002.

[137] S. M. Sze. *Semiconductor Devices - Physics and Technology.* John Wiley & Sons Inc. New York, 2nd edition, 2002.

[138] G. Berlanda, M. Campione, M. Moret, A. Sassella, and A. Borghesi. "Evidence of postdeposition nucleation in organic molecular thin films". *Phys. Rev. B*, 69:085409, 2004.

[139] P. R. Ribič, Vivek Kalihari, C. D. Frisbie, and G. Bratina. "Growth of ultrathin pentacene films on polymeric substrates". *Phys. Rev. B*, 80:115307, 2009.

[140] J. R. Morales-Cifuentes, T. L. Einstein, and A. Pimpinelli. "How "Hot Precursors" Modify Island Nucleation: A Rate-Equation Model". *Phys. Rev. Lett.*, 113:246101, 2014.

[141] T. L. Einstein, A. Pimpinelli, D. L. González, and J. R. Morales-Cifuentes. "Progress in characterizing submonolayer island growth: Capture-zone distributions, growth exponents, & hot precursors". *J. Phys. Conf. Ser.*, 640:012024, 2015.

[142] A. Winkler. "On the nucleation and initial film growth of rod-like organic molecules". *Surf. Sci.*, 652:367 – 377, 2016.

[143] L. Tumbek, C. Gleichweit, K. Zojer, and A. Winkler. "Origin of the bimodal island size distribution in ultrathin films of para-hexaphenyl on mica". *Phys. Rev. B*, 86:085402, 2012.

[144] J. G. Amar, F. Family, and M. N. Popescu. "Kinetics of submonolayer epitaxial growth". *Comput. Phys. Commun.*, 146(1):1 – 8, 2002.

[145] H. Honjo, S. Ohta, and M. Matsushita. "Irregular Fractal-Like Crystal Growth of Ammonium Chloride". *J. Phys. Soc. Jpn.*, 55(8):2487–2490, 1986.

[146] H. Honjo. *Research of Pattern Formation.* KTK Scientific Publishers Tokyo, 1994.

[147] G. Hlawacek, V. Veligura, S. Lorbek, T. F. Mocking, A. George, R. van Gastel, H. J. W. Zandvliet, and B. Poelsema. “Imaging ultra thin layers with helium ion microscopy: Utilizing the channeling contrast mechanism”. *Beilstein J. Nanotechnol.*, 3:507–12, 2012.

[148] R. G. Della Valle, E. Venuti, A. Brillante, and A. Girlando. “Molecular Dynamics Simulations for a Pentacene Monolayer on Amorphous Silica”. *Chem. Phys. Chem.*, 10(11):1783–1788, 2009.

[149] P. Meakin and J. M. Deutch. “The formation of surfaces by diffusion limited annihilation”. *The Journal of Chemical Physics*, 85(4):2320–2325, 1986.

[150] G. M. Schütz. “Diffusion-limited annihilation in inhomogeneous environments”. *Z. Phys. B*, 104(3):583–590, 1997.

[151] M. Kratzer and C. Teichert. “Thin film growth of aromatic rod-like molecules on graphene”. *Nanotechnology*, 27(29):292001, jun 2016.

Acronyms

2D Two-dimensional.

3D Three-dimensional.

5A Pentacene.

6P Para-hexaphenyl.

AC Alternating Current.

AES Auger Electron Spectroscopy.

AFM Atomic Force Microscopy.

Al Chemical element Aluminum.

ALA Attachment-Limited Aggregation.

Ar^+ ions Positive ions of the chemical element Argon.

ARPES Angle-Resolved Photoemission Spectroscopy.

Au Chemical element Gold.

Ba Chemical element Barium.

BaF_2 Barium fluoride.

CPD Contact Potential Difference.

Cu Chemical element Copper.

CZD Capture-Zone Distribution using a generalized Wigner surmise in the scaling theory of Pimpinelli and Einstein [19, 20].

DC Direct Current.

DFT Density Functional Theory.

DI Multimode AFM with a Nanoscope IIIa controller from Digital Instruments/Veeco.

DLA Diffusion-Limited Aggregation.

DNA Desoxyribonucleic acid.

DOS density of states.

F Chemical element Fluorine.

FFM Friction Force Microscopy.

FWF Austrian Science Fund (Fonds zur Förderung der wissenschaftlichen Forschung).

GaAs Gallium arsenide.

GFIS Gas Field Ion Source.

H_2SO_5 Peroxymonosulfuric acid, also known as Persulfuric acid, Peroxysulfuric acid, or Caro's acid.

HATCN Hexaazatriphenylenehexacarbonitrile.

He^+ ion Positive ion of the chemical element Helium, produced at a tungsten atomic trimer in a helium ion microscope.

HIM Helium Ion Microscopy.

HOMO Highest Occupied Molecule Orbital.

HOPG Highly Oriented Pyrolytic Graphite.

In_2O_3 Indium(III) oxide.

ISD Island Size Distribution used in the scaling theory by Amar and Family [18].

K^+ ions Positive ions of the chemical element Potassium.

KCl Potassium chloride.

kMC kinetic Monte Carlo simulation.

KPFM Kelvin Probe Force Microscopy.

LASER Light Amplification by Stimulated Emission of Radiation.

LFM Lateral Force Microscopy.

LUMO Lowest Unoccupied Molecule Orbital.

MBE Molecular Beam Epitaxy.

MC Monte Carlo simulation.

MD Molecular Dynamics (simulation).

NFN National Research Network of Austria (Nationales Forschungsnetzwerk).

NH_4Cl Ammonium chloride.

Ni Chemical element Nickel.

O_2 Dioxygen, the common allotrope of the chemical element Oxygen.

OFET Organic Field Effect Transistor.

OLED Organic Light Emitting Diode.

OMBE Organic Molecular Beam Epitaxy.

OTFT Organic Thin Film Transistor.

PTCDA Perylene-3,4,9,10-tetracarboxylic dianhydride.

QCB Quartz Crystal (micro)Balance.

RE Rate Equations used in rate theory by Venables, Spiller and Hanbücken [7].

RHEED Reflection High Energy Electron Diffraction.

RT Room Temperature.

SEM Scanning Electron Microscopy.

Si Chemical element Silicon.

Si_2O_5 Phyllosilicates (group of silicate minerals which have a sheet-like structure with the chemical formula $[Si_{2n}O_{5n}]^{2n-}$.

SiO_2 Silicon dioxide.

SPM Scanning Probe Microscopy.

STM Scanning Tunneling Microscopy.

TDS Thermal Desorption Spectroscopy.

TiN Titanium nitride.

TSM Transverse Shear Microscopy.

TU-Graz Graz University of Technology, Austria.

UHV Ultra-High Vacuum.

UV Ultraviolet.

XPS X-ray Photoelectron Spectroscopy.